INFORMATION TO USERS

This manuscript has been reproduced from the microfilm master. UMI films the text directly from the original or copy submitted. Thus, some thesis and dissertation copies are in typewriter face, while others may be from any type of computer printer.

The quality of this reproduction is dependent upon the quality of the copy submitted. Broken or indistinct print, colored or poor quality illustrations and photographs, print bleedthrough, substandard margins, and improper alignment can adversely affect reproduction.

In the unlikely event that the author did not send UMI a complete manuscript and there are missing pages, these will be noted. Also, if unauthorized copyright material had to be removed, a note will indicate the deletion.

Oversize materials (e.g., maps, drawings, charts) are reproduced by sectioning the original, beginning at the upper left-hand corner and continuing from left to right in equal sections with small overlaps.

Photographs included in the original manuscript have been reproduced xerographically in this copy. Higher quality 6" x 9" black and white photographic prints are available for any photographs or illustrations appearing in this copy for an additional charge. Contact UMI directly to order.

ProQuest Information and Learning
300 North Zeeb Road, Ann Arbor, MI 48106-1346 USA
800-521-0600

CHARACTERIZATION OF InP AND InGaAsP GROWN BY He-PLASMA-ASSISTED GSMBE

By

HEIDI PINKNEY, B.Sc., M.Sc.

A Thesis
Submitted to the School of Graduate Studies
in Partial Fulfilment of the Requirements
for the Degree
Doctor of Philosophy

McMaster University

InP AND InGaAsP GROWN BY He-PLASMA-ASSISTED GSMBE

DOCTOR OF PHILOSOPHY (1999)
(Engineering Physics)

McMaster University
Hamilton, Ontario

TITLE: Characterization of InP and InGaAsP Grown By He-Plasma-Assisted GSMBE

AUTHOR: Heidi Pinkney, B.Sc. (Imperial College of Science, Technology and Medicine, University of London), M.Sc. (University of Toronto)

SUPERVISOR: Professor David A. Thompson

NUMBER OF PAGES: xii, 140

Abstract

This thesis involved the characterization of InP and InGaAsP grown by He-plasma-assisted gas source molecular beam epitaxy. Samples were typically grown under standard GSMBE conditions, in terms of growth rate and substrate temperature, except for the presence of a low energy helium plasma generated from an electron-cyclotron resonance source. These materials exhibit increased resistivity and faster optical response times with respect to standard materials grown without the plasma. The unusual properties are believed to be caused by the impact of the plasma particles during growth. Samples were characterized under various doping and anneal conditions using Hall effect measurements, temperature-dependent resistivity studies, positron annihilation spectroscopy, photoluminescence and SIMS analysis.

Undoped He-InP was weakly n-type as-grown, with a carrier concentration much lower than that of standard InP, suggesting that electron traps were present. On anneal, the carrier concentration decreased further, implying that donor-like defects had been removed. The sample doped with $3x10^{17}$ cm^{-3} Be was also n-type; the Be was found to be compensated by donor-like defects. Positron annihilation measurements indicated the presence of single and divacancy defects, which enlarged upon anneal.

The characterization of the quaternary constituted the core of the experimental work. He-InGaAsP exhibited the same trends as the binary He-InP. The undoped and Si-doped samples exhibited low carrier concentrations, indicating the presence of electron traps. Annealing removed these electron traps. The samples doped with $<2x10^{18}$ cm^{-3} Be were weakly n-type as-grown, but became p-type on anneal, suggesting the removal of donor-like compensating defects. Samples doped with $>2x10^{18}$ cm^{-3}Be were p-type as grown, but the hole concentration was lower than expected. As for the He-InP, positron annihilation spectroscopy indicated the presence of neutral or negatively-charged open volume defects that increased in size on anneal. None of the He-InGaAsP samples exhibited photoluminescence until annealed at temperatures of ~600°C.

To estimate the energy levels and concentrations of the defects responsible for the unusual properties of the quaternary, a Fermi-Dirac model was fitted to the Hall effect data. Two donor-like and two acceptor-like levels were identified.

Acknowledgements

I would like to acknowledge my supervisor, Dr. David Thompson, and the other members of my committee, Drs. Haugen and Simmons, for their helpful contributions and guidance. I should also like to thank Brad Robinson and Scott McMaster for the (numerous!) samples I requested. This work would not have been possible without the help of our "collaborators", who gave generously of their time and expertise: Dr. Peter Simpson and Dr. Uwe Myler of the Department of Physics and Astronomy, University of Western Ontario, London for the positron annihilation spectroscopy; Dr. Rick Streater of the Advanced Technology Group at Nortel Networks, Ottawa, for the SIMS analysis; Dr. Peter Smith and Li Qian of the Department of Electrical and Computer Engineering, University of Toronto, for discussions and data concerning the optical measurements on the quaternary samples; and Dr. Jin Ung Kang at the Naval Research Laboratory, Washington, for various measurements on the He-InP material.

I am indebted to my friends, recent and long-standing, for making daily life so much more enjoyable: Doug Bruce, Chris Butcher, Mike Clarke, Adam Densmore, Andy Duft, Gary Dyck, Marg Fraser, Jim Garrett, Barb Guild, John Hazell, Melanie Kahana, Ray LaPierre, Dave MacKinnon, Peter Mascher, Doris Stevanovic, Judy van Stralen, Jim Swoger, Eugene Tan and Christine Wettlaufer. I apologize if I have forgotten anyone. My family deserve special thanks for their constant support: my Mum, Joan, who assured me that "it would all work out" ; my Dad, John, who only asked that we "try our best"; my sister, Amanda, for her astute advice and wicked sense of humour; and my brother, Trevor, and sister-in-law, Heather, for their confidence in my abilities. Last, but not least, I thank Gregory, "the watchful one", my fiance and best friend, just for being himself.

Financial support for this work was provided by the MMO (Materials and Manufacturing Ontario), Nortel Networks and OGS (Ontario Graduate Scholarships).

Contents

1 Background **1**

1.1 Introduction 1

1.2 Low-Temperature-Grown GaAs 3

1.3 He-Plasma-Assisted GSMBE Materials 5

1.4 Summary 9

2 Preparation and Characterization Techniques **11**

2.1 Sample Growth 12

2.1.1 Gas Source Molecular Beam Epitaxy System 12

2.1.2 Electron-Cyclotron Plasma Generation System 15

2.1.3 Rapid Thermal Annealer (RTA) 16

2.2 Variable Energy Positron Annihilation Technique 17

2.3 Electrical Characterization 20

2.3.1 Room-Temperature Hall Effect Measurements 20

2.3.2 Variable-Temperature Hall Effect Measurements 25

2.3.3 N-i-n Measurements 26

2.4 Low-Temperature Photoluminescence Technique 29

2.5 SIMS Technique 31

3 Experimental Results for InP **33**

3.1 Introduction 33
3.2 Positron Results 33
3.2.1 Standard InP 34
3.2.2 He-Plasma InP 34
3.3 Hall Effect Measurements 39
3.4 N-i-n Results 42
3.5 SIMS Results 45
3.6 Discussion 48

4 Experimental Results for InGaAsP **52**
4.1 Introduction 52
4.2 Positron Results 52
4.2.1 Standard InGaAsP 53
4.2.2 He-InGaAsP 53
4.2.3 Low Growth Rate He-InGaAsP 62
4.3 Room-Temperature Hall Effect Measurements 62
4.3.1 Undoped He-InGaAsP 65
4.3.2 Si-doped He-InGaAsP 67
4.3.3 Be-doped He-InGaAsP 71
4.4 Variable-Temperature Hall Effect Measurements 76
4.5 Photoluminescence measurements of He-InGaAsP samples 77
4.5.1 Undoped InGaAsP 78
4.5.2 Si-doped InGaAsP 80
4.5.3 Be-doped InGaAsP 83
4.6 SIMS Results 86
4.7 Summary 89

5 Fermi-Dirac Statistics Modeling **91**

5.1 Introduction 91

5.2 Theory 92

5.3 Details of the Calculations 94

5.4 High Doping Considerations 96

5.5 Analysis of Experimental Results 100

5.5.1 Si-doped He-InGaAsP 100

5.5.2 Be-doped He-InGaAsP 104

5.5.3 Annealing Studies 109

5.5.4 Variable-Temperature Hall Effect Measurements 112

5.6 Summary Discussion for InGaAsP 114

6 Discussion and Future Work **118**

6.1 Defects in III-V Semiconductors 118

6.1.1 InGaAsP Defects 119

6.1.2 InP Defects 121

6.1.3 GaAs Defects 123

6.2 Future Work 125

6.2.1 Material Characterization 125

6.2.2 Device Applications 127

6.3 Conclusion 128

A Material Parameters **133**

References **135**

List of Figures

1.1 Pump-probe measurements for Be-doped He-InGaAsP, bandgap wavelength 1.5 μm. 7

1.2 Effect of He-plasma-assisted GSMBE growth on the bandedge of InGaAsP. 8

2.1 McMaster GSMBE system 14

2.2 The regions used to calculate the S-parameter for positron annihilation studies. 18

2.3 Biasing configurations for measuring resistivity 21

2.4 N-i-n device structure for electrical measurements 27

2.5 Low-temperature photoluminescence system 29

3.1 Positron annihilation results for undoped standard InP sample, as-grown and after all anneals. 35

3.2 Positron annihilation results for Be-doped InP standard sample, as-grown and after all anneals. 35

3.3 Positron annihilation results for undoped He-InP sample, as-grown and after all anneals. 36

3.4 Positron annihilation results for Be-doped ($3x10^{17}$ cm^{-3}) He-InP sample, as-grown and after all anneals. 37

3.5 Hall effect measurements for undoped He-InP sample, as-grown and after all anneals. 40

3.6 Hall effect measurements for Be-doped He-InP sample, as-grown and after all anneals. 41

3.7 Temperature-dependent resistivity measurements for undoped and Be-doped He-InP 43

3.8 Temperature-dependent resistivity measurements for annealed undoped He-InP. 44

3.9 Structure of sample 2274, grown with deuterium for SIMS measurements. 46

3.10 SIMS results for sample 2274, a) before and b) after anneal at 600°C. 47

3.11 Sheet resistance as a function of anneal temperature for undoped and Be-doped He-InP. 49

3.12 The effect of annealing on the carrier lifetime of a) He-InP and b) He-InP+Be, as measured by transient ellipsometric surface photoreflectance. 50

4.1 Positron annihilation results for undoped InGaAsP standard, as-grown and after all anneals. 54

4.2 Positron annihilation results for undoped He-InGaAsP, as-grown and after all anneals. 56

4.3 Positron annihilation results for He-InGaAsP doped with $3x10^{17}$ cm^{-3} Si, as-grown and after all anneals. 57

4.4 Positron annihilation results for He-InGaAsP doped with $3x10^{18}$ cm^{-3} Si, as-grown and after all anneals. 58

4.5 Positron annihilation results for He-InGaAsP doped with $3x10^{17}$ cm^{-3} Be, as-grown and after all anneals. 59

4.6 Positron annihilation results for He-InGaAsP doped with $3x10^{18}$ cm^{-3} Be, as-grown and after all anneals. 60
4.7 Comparison of positron annihilation results for control InGaAsP, standard growth-rate He-InGaAsP and low growth-rate He-InGaAsP. . . 63
4.8 Positron annihilation results for low growth rate He-InGaAsP, as-grown and after all anneals. 64
4.9 The carrier concentration and mobility as a function of anneal temperature for undoped He-InGaAsP. 66
4.10 Carrier concentration as a function of doping for Si-doped He-InGaAsP compared to expected values for standard InGaAsP. 68
4.11 Effect of annealing on carrier concentration in Si-doped He-InGaAsP. 69
4.12 Effect of annealing on carrier mobility in Si-doped He-InGaAsP. . . . 70
4.13 Carrier concentration as a function of doping for Be-doped He-InGaAsP samples 72
4.14 Effect of annealing on carrier concentration in Be-doped He-InGaAsP. 73
4.15 Effect of annealing on carrier mobility in Be-doped He-InGaAsP. . . . 74
4.16 Arrhenius plot of the free carrier concentration in Be-doped ($3x10^{17}$ cm^{-3}) He-InGaAsP. 76
4.17 Effect of annealing on PL spectrum of undoped He-InGaAsP. 79
4.18 Effect of annealing temperature on PL spectrum of weakly Si-doped ($3x10^{17}$ cm^{-3}) He-InGaAsP. 81
4.19 Effect of annealing temperature on PL spectrum of heavily Si-doped ($3x10^{18}$ cm^{-3}) He-InGaAsP. 82
4.20 Effect of annealing temperature on PL spectrum of Be-doped ($3x10^{17}$ cm^{-3}) He-InGaAsP. 84

4.21 Effect of annealing temperature on PL spectrum of Be-doped ($3x10^{18}$ cm^{-3}) He-InGaAsP. 85
4.22 Quaternary structure sent for SIMS analysis. 86
4.23 SIMS measurements for He-quaternary sample, a) before and b) after 10 second anneal at 700°C. 87

5.1 Calculated carrier concentrations for acceptor-like traps of various densities placed 0.2 eV above the valence band edge. 102
5.2 Calculated carrier concentrations for acceptor-like traps of various densities placed 0.4 eV above the valence band edge. 102
5.3 Calculated carrier concentrations for acceptor-like traps of various densities placed 0.6 eV above the valence band edge. 103
5.4 Calculated carrier concentrations for acceptor-like traps of various densities placed 0.7 eV above the valence band edge. 103
5.5 Calculated carrier concentrations for acceptor-like traps with an energy level 0.68 eV above the valence band edge and a concentration of $5x10^{17}$ cm^{-3}. 105
5.6 Calculated carrier concentrations for acceptor-like traps placed 0.68 eV ($5x10^{17}$ cm^{-3}) and 0.85 eV ($1x10^{18}$ cm^{-3}) above the valence band edge. 105
5.7 The He-InGaAsP Hall effect data, plotted as Fermi energy versus doping concentration, for all Be- and Si-doped samples. 106
5.8 Effect of adding each trap on calculated Fermi energy. 108
5.9 Effect of annealing on calculated Fermi energy. 110
5.10 Effect of annealing on estimated trap concentrations. 111
5.11 Model simulations of ln(n) versus 1/kT for a number of doping concentrations. 113

List of Tables

3.1 InP samples studied with the variable energy positron annihilation technique 34

4.1 Summary of InGaAsP samples and anneal temperatures 54

4.2 Summary of samples for Hall effect measurements 65

5.1 Calculated trap energy levels and concentrations as a function of anneal temperature. 111

6.1 Experimentally determined defects in InGaAsP 120

6.2 Experimentally determined defects in InP 121

6.3 Theoretically calculated defects in InP. 123

6.4 Experimentally determined defects in GaAs 123

A.1 Binary parameters used to calculate quaternary values. 134

A.2 Parameters for materials studied in this work. 134

Chapter 1

Background

1.1 Introduction

Society today has unprecedented access to information and numerous ways of communicating and, from the recent increase in internet and cellular phone use, it seems that the communications market will continue to grow. However, keeping up with this demand requires continual improvements to the technologies that make efficient communications possible, by which we mean increases in the rate at which data are transmitted, routed and received.

For a number of years, the telecommunications industry has employed semiconductor opto-electronic devices to produce and detect the data signals, combined with optical fiber technology to transport them. The optoelectronic devices are usually fabricated from quaternary alloys of the III-V binary semiconductors, indium phosphide (InP) and gallium arsenide (GaAs). The composition of these quaternary alloys, $In_{1-x}Ga_xAs_yP_{1-y}$ (where x, $1-x$, y and $1-y$ denote the mole fraction of gallium, indium, arsenic and phosphorus, respectively), can be chosen such that the devices emit or detect light at a wavelength that optimizes the performance of the optical fibre. Standard silica-glass fibre exhibits minimum attenuation at 1.55 μm and minimum dispersion at 1.3 μm [Saleh and Teich (1991), p. 879]. For long-distance

telecommunications, attenuation is the more serious problem and hence the 1.55 μm wavelength range is preferred, especially since dispersion-minimized fibre is now available at this wavelength. Clearly then, to obtain the maximum transmission rates, we need fast signal pulses, a high repetition rate and a small bandwidth that will suffer minimal dispersion in the fibre.

The maximum repetition rate achievable in a device is determined to a certain extent by the material characteristics. To manipulate a series of discrete pulses with detectors, switches and couplers, for example, the device must dissipate the electron-hole pairs produced by one pulse before the next pulse enters the system. Typically, the electron lifetime in standard high-quality intrinsic epitaxial III-V semiconductors is on the order of hundreds of picoseconds to nanoseconds. To reduce this lifetime, one has to provide alternative routes by which the holes and electrons can recombine with each other. For a number of years, semiconductor properties have been radically changed by the introduction of intentional flaws, either in the form of native defects (vacancies, antisites and interstitials) or substitutional impurities. All such defects give rise to localized levels in the band gap of the semiconductor host [Jaros, (1980)]. Shallow substitutional impurities, such as the dopants beryllium (Be) and silicon (Si) used in this work, are added during growth of the sample to increase the conductivity of the materials, whereas "deep" impurities, such as iron in "semi-insulating" (SI) InP, are introduced to purposely reduce the conductivity by causing trapping and recombination of the free carriers. Similar effects can be achieved with native defects. For example, the EL2 defect is used to produce bulk semi-insulating GaAs. Of course, the introduction of large numbers of defects can degrade other aspects of the optical performance [Melloch et al. (1996)] and a compromise is usually necessary in the design of the final device [Smith and Benjamin (1995)].

The most recent fast-response material to generate interest is GaAs grown by molecular beam epitaxy (MBE) under low-temperature conditions (low-temperature-grown or LTG GaAs), as discussed below in Section 1.2. However, this material has a bandgap wavelength of approximately 0.87 μm and, therefore, is not compatible with standard silica-glass fibre and the associated optical devices currently in use. The quaternary material, InGaAsP, grown with a bandgap wavelength of 1.55 μm using He-plasma-assisted gas source molecular beam epitaxy, is a viable alternative fast-response optoelectronic material. In this work, such material is characterized in detail and a model is proposed to explain the unusual properties this material exhibits.

1.2 Low-Temperature-Grown GaAs

Recently, low-temperature-grown (LTG) MBE GaAs has proved to be of great interest to the semiconductor community, due to its unusual electrical and optical properties [for example, see the summary by Melloch et al. (1996)]. In addition, LTG GaAs is readily fabricated alongside standard GaAs-based materials, since it is grown using well-known standard materials and techniques. At low growth temperatures (150 to 400°C versus the usual 600°C), excess arsenic incorporates as point defects in the form of deep-donor arsenic antisites and deep acceptor gallium vacancies [Kaminska et al. (1989), Look et al. (1993)]. The high strain observed in as-grown samples implies the presence of arsenic interstitials also [Warren et al. (1992)]. There is a thickness limit of $\sim 2\mu$m, due to this high strain, although Melloch et al. were able to circumvent this problem by brief periods of annealing at 600°C during growth [Melloch et al. (1996)]. On anneal, the excess arsenic forms precipitates which grow larger with higher temperature annealing. These precipitates are apparent in transmission electron microscope (TEM) images.

LTG GaAs is highly resistive (10^4 to 10^5 Ω-cm) when grown at 200-300°C and becomes semi-insulating ($\sim 10^7$ Ω-cm) when annealed at temperatures above 500°C [Bliss et al. (1992a)]. The response of the material depends strongly on the growth temperature and, therefore, percentage excess arsenic incorporated in the sample; for example, the optical carrier lifetime of LTG GaAs grown at 200°C was found to be ~ 0.4 ps, while growth at >250°C resulted in a lifetime of >60 ps [Gupta et al. (1992)]. The same group found that the optical carrier lifetime of undoped LTG GaAs, grown at 200°C and subsequently annealed at 600°C for 10 minutes, was not significantly different from that of the as-grown sample. However, Harmon et al. (1993) found that the carrier lifetime of undoped LTG GaAs, grown at 320°C, showed a marked increase when annealed at temperatures of 650°C and higher for 30 seconds, suggesting that the optical properties of the LTG GaAs may be compromised if subsequent layers were to be grown at standard substrate temperatures. Finally, the refractive index of as-grown LTG GaAs, grown at 300°C, can be changed by up to 0.1, depending on the intensity and wavelength of the signal pulse, making LTG GaAs a high-response, non-linear material suitable for all-optical telecommunications devices [Benjamin et al. (1994), Smith and Benjamin (1995)].

Two theories have been extended to describe the mechanisms behind the behaviour of LTG GaAs: the defect model and the Schottky model. According to Melloch et al. (1996), the (point) defect model tends to dominate for as-grown and weakly annealed samples, and the Schottky model (arsenic precipitates) dominates for more strongly annealed samples. A discussion of the relative roles of the As_{Ga} defects and As precipitates is given in Look (1991).

McMorrow et al. (1995) have used LTG GaAs buffer layers to reduce the charge enhancement effects seen in GaAs FETs, thereby improving their suitability

for space applications. Picosecond LTG GaAs-based photoconductive optoelectronic detectors have also been fabricated with a response time (full width half maximum) of 1.6 ps [Smith et al. (1989)]. Harmon et al. (1995) fabricated a photodetector from LTG GaAs that was able to detect 1.3 and 1.5 μm wavelengths, but with low responsivities of 0.1 and 0.01 A/W, respectively, for 10 μW input powers. To improve the response in the 1.55 μm wavelength range requires the use of the InGaAsP alloys.

1.3 He-Plasma-Assisted GSMBE Materials

The He-plasma assisted GSMBE materials were first prepared and studied by Daniel Mitchell at McMaster University [Mitchell (1995), Thompson et al. (1995), Mitchell et al. (1996)]. The binary material, InP, exhibited very unusual properties when it was grown in the gas source MBE system under standard conditions (III/V ratio = 2.9 and growth temperature $\sim$ 450°C), except for the presence of an electron cyclotron resonance generated He-plasma. This He-plasma-grown InP (referred to as He-InP below) was weakly n-type and highly resistive, with a resistivity $> 10^5\Omega-$cm, versus approximately 1 $\Omega-$cm for a standard InP sample. Hall effect studies indicated that the carrier concentration was $\sim 10^{13}$ cm^{-3} and the mobility $\sim$ 1700 cm^2/Vs [Mitchell (1996)], both much reduced compared to a standard sample for which carrier concentrations would be $\sim 1-2\text{x}10^{15}$ cm^{-3} and the mobility $\sim$ 4800 cm^2/Vs. Also, the samples emitted very little photoluminescence. Subsequent growths with Be-doped samples indicated that a He-plasma-assisted InP sample doped with $3\text{x}10^{18}$ cm^{-3} Be was still (weakly) n-type. Despite these dramatic changes in material characteristics, double crystal x-ray diffraction indicated that the samples were not strained and the surface of the sample exhibited the same morphology as a standard sample.

It was postulated that these properties were caused by the impact of the

plasma particles during growth, firstly because no evidence of residual He contamination was found from thermal desorption measurements and secondly, because simply the presence of He gas (but no plasma discharge) did not cause any changes to the standard InP properties [Mitchell et al. (1996)]. One native defect likely to be present after growth with this technique is the phosphorus vacancy: the average energy of the plasma particles is low, approximately 25-30 eV, and therefore a plasma particle is much more likely to dislodge the lighter P atom from the lattice than the heavier In atom. However, the phosphorus vacancy is donor-like and hence should contribute to the electron concentration, rather than reduce it. Therefore, it seems likely that an acceptor-like defect is also present, possibly the phosphorus interstitial, which would also arise from the collision process [Mitchell et al. (1995)].

A number of quaternary samples were also studied. Standard pump-probe measurements on He-InGaAsP with a bandgap wavelength of 1.55 μm , carried out in collaboration with Dr. Peter Smith's group at the University of Toronto, indicated that the absorption of undoped He-InGaAsP recovered with a single exponential lifetime of 15 ps, as compared to $>$ 500 ps for standard InGaAsP [Mitchell et al. (1996)]. Doping the samples with Be decreased the optical response time, as illustrated in Figure 1.1 [Qian et al. (1997a)]; in particular, sub-picosecond values were obtained for a Be-doping concentration of 6×10^{18} cm^{-3}.

By using a Z-scan technique [Sheik-Bahae et al. (1990)], the same group determined that the optical refractive index could be changed by as much as $\Delta n = -0.077$ for a wavelength of 1.57 μm, only slightly less than for standard InGaAsP [Qian et al. (1997b)]. Fortunately, despite these unusual and very useful optical properties, the defects had not affected the sharpness of the bandedge (Figure 1.2) [Qian et al. (1997a)].

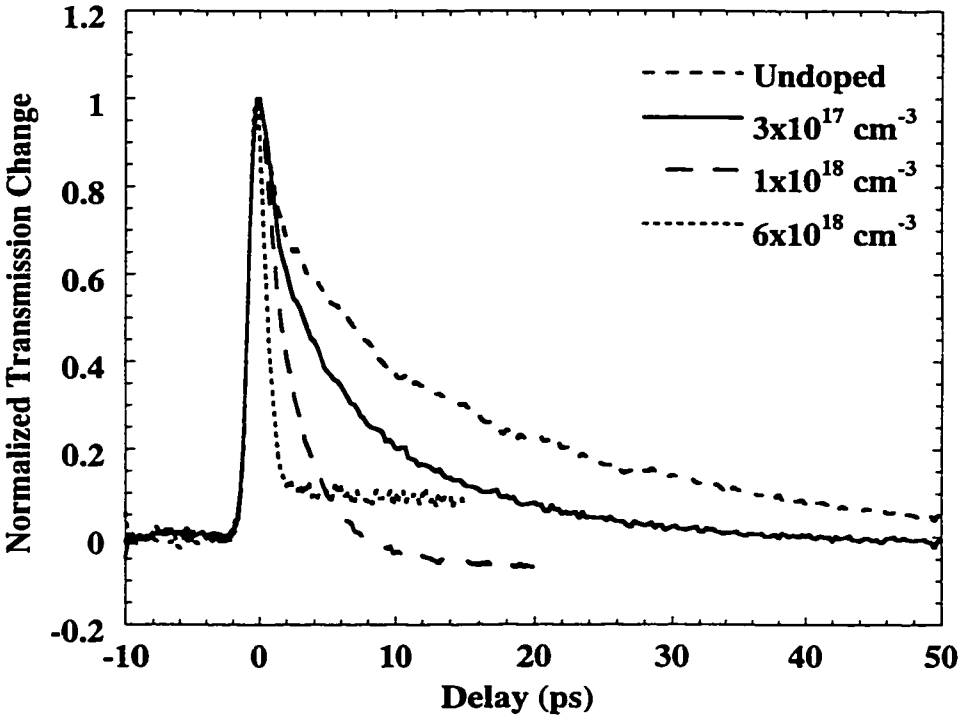

Figure 1.1: Pump-probe measurements for Be-doped He-InGaAsP, bandgap wavelength 1.5 μm. (After Qian et al. (1997a)

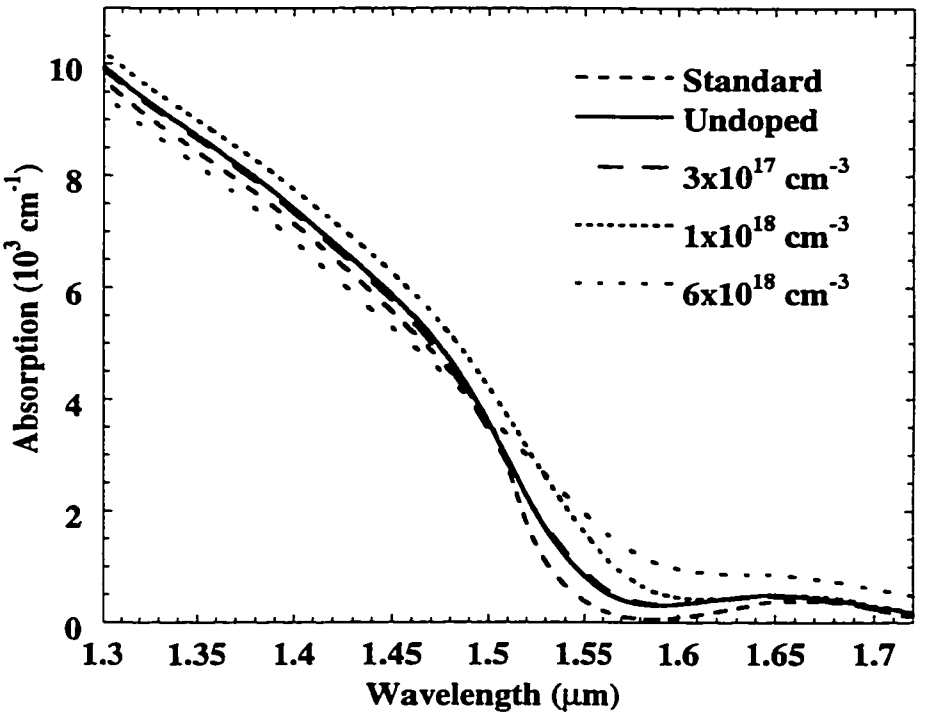

Figure 1.2: Effect of He-plasma-assisted GSMBE growth on the bandedge of InGaAsP.(From Qian et al. (1997b))

It can be seen that the He-plasma-assisted epitaxial materials may be very significant technologically: the high resistivity of the He-InP would lend itself to electrical isolation layers and radiation-hard devices, while the picosecond response of the quaternary could be applied to ultrafast telecommunications devices, such as all-optical switches, ultrafast detectors or time-domain multiplexing applications. Also, the growth technique is relatively straightforward, requiring only the additional operation of the He-plasma. Unlike LTG GaAs, the growth temperatures are comparable to those for standard GSMBE growths, therefore are easily measured and controlled. Also, no undesirable self-annealing of the fast-response layer occurs when subsequent cladding layers are grown at standard temperatures.

However, in order to fully utilize the material properties in a device application, it is necessary to understand the reason for the material behaviour. In this work, we found that the quaternary material exhibits similar characteristics to the binary material. For the first time, a comprehensive study of the He-InGaAsP behaviour as a function of doping and annealing was undertaken. The electrical, optical, SIMS and positron annihilation results described herein will be related to the work performed in collaboration with other groups. Finally, a model based on the electrical measurements will be proposed to explain the characteristics observed to date.

1.4 Summary

Details of the He-plasma-assisted gas source molecular beam growth technique and sample characterization can be found in Chapter 2. The electrical, positron annihilation and SIMS results for He-InP are described in Chapter 3. The core of the experimental work is discussed in Chapter 4, in which the positron annihilation, electrical, photoluminescence and SIMS studies for He-InGaAsP are covered. Chapter

5 introduces the Fermi statistics model used to explain the experimental results. The study concludes in Chapter 6 with a discussion of the experimental findings and suggestions for future work.

Chapter 2

Preparation and Characterization Techniques

Molecular beam epitaxy (MBE) is a high-vacuum evaporation technique that allows the growth of semiconductor layers of precise composition and thickness that take on the crystal structure of the substrate [Cho and Arthur (1975), Wicks (1993), Meier et al. (1994)]. The system used in these studies is described as a "gas source" system because the group V sources, arsenic (As_2) and phosphorus (P_2), are derived by cracking the gaseous hydrides, arsine (AsH_3) and phosphine (PH_3), while the group III sources, indium and gallium, are elemental. Using gaseous sources for the group V materials removes the difficulties involved with handling elemental phosphorus. Firstly, phosphorus has a high vapour pressure and hence the group V flux has to be high to minimize desorption from the growth surface. This means that large elemental sources must be used if the chamber is not to be opened too frequently [Wicks (1993)]. Secondly, phosphorus often contains a number of allotropes, each of which has a different vapor pressure [Panish (1986), Panish and Temkin (1989)]. As the allotropes with the highest vapour pressure leave the source, the temperature required to maintain the same phosphorus flux changes with time. Thirdly, until recently, elemental sources contained impurities, like water. However, the gaseous

sources also have their drawbacks. The hydrogen that results from the cracking process is always present during growth (the chamber pressure is $\sim$ 5x10^{-5} Torr) and, therefore, is also present in the plasma due to backstreaming into the ECR plasma source. Under normal growth conditions, hydrogen does not incorporate in the epilayers, but it must be considered when discussing the properties of the He-plasma materials, because it has been found previously to affect the material properties when present as a hydrogen plasma [Mitchell (1995)]. To address this issue, helium-plasma grown materials were submitted for SIMS analysis to determine how much "hydrogen" (or, as seen later, deuterium) incorporated during plasma growth.

The unusual properties of the He-plasma materials are believed to be caused by deep defects. However, the experimental characterization of defects is extremely difficult, for a number of reasons [Jaros, (1980)]: deep chemical impurities, vacancies, interstitials and antisite defects may exhibit a number of charge states; dynamic relaxation effects will be present; the observed transition energies may not correspond to one-electron ionization energies; lastly, no single technique can explain all the features of a defect including its origin, structure, energy levels or concentration. For this reason, a number of complementary techniques must be used, each of which provides a glimpse of the nature of the defects. In this work, variable energy positron annihilation spectroscopy, electrical studies and low-temperature photoluminescence were used, each of which is described below.

2.1 Sample Growth

2.1.1 Gas Source Molecular Beam Epitaxy System

All samples used in this work were grown in the gas source molecular beam epitaxy (GSMBE) system at McMaster University, shown schematically in Figure

2.1 In this system, the elemental group III sources, indium (In) and gallium (Ga), are evaporated from pyrolytic boron nitride (PBN) crucibles inside the chamber, as are the dopants, beryllium (Be, p-type) and silicon (Si, n-type). By controlling the temperature of these crucibles, the vapour pressure of the element can be changed, thereby altering the flux directed towards the sample. The group V fluxes, As_2 and P_2, are derived from hydride sources, which are dissociated as they enter the chamber by passing them over a rhenium catalyst at 1000°C. The gas flow of each hydride is controlled by individual mass flow controllers (MFCs) outside the chamber. All sources of host and dopant materials are shuttered to control which elements reach the growth surface at any given time. The substrate stage rotates to improve the uniformity across the wafer. The substrate temperature (450 to 460°C for this work) is monitored using an optical pyrometer. The ultra-high vacuum (UHV) is obtained with a diffusion pump, and there are liquid-nitrogen-cooled cryopanels inside the chamber on which contaminants condense. The chamber is usually maintained at a base pressure of 10^{-10} Torr, and this increases to $5x10^{-5}$ Torr during growth. Most structures are grown at a rate of 1 μm/hour (1 monolayer/second), with a III/V flux ratio of 2.9. The growth rate is determined by the rate of incorporation of the Group III species, for which the sticking coefficients are approximately unity. The group V species, particularly phosphorus, desorb more rapidly from the growth surface at these growth temperatures, hence a Group V overpressure must be used to ensure the III/V stoichiometry of the epilayers.

The maximum obtainable doping concentration is determined by the incorporation of the dopant in the host lattice. The n-type dopant, silicon, is amphoteric (that is, it could act as an n-type or a p-type dopant), since it sits in Group IV of the periodic table. However, it is found experimentally that, under normal growth condi-

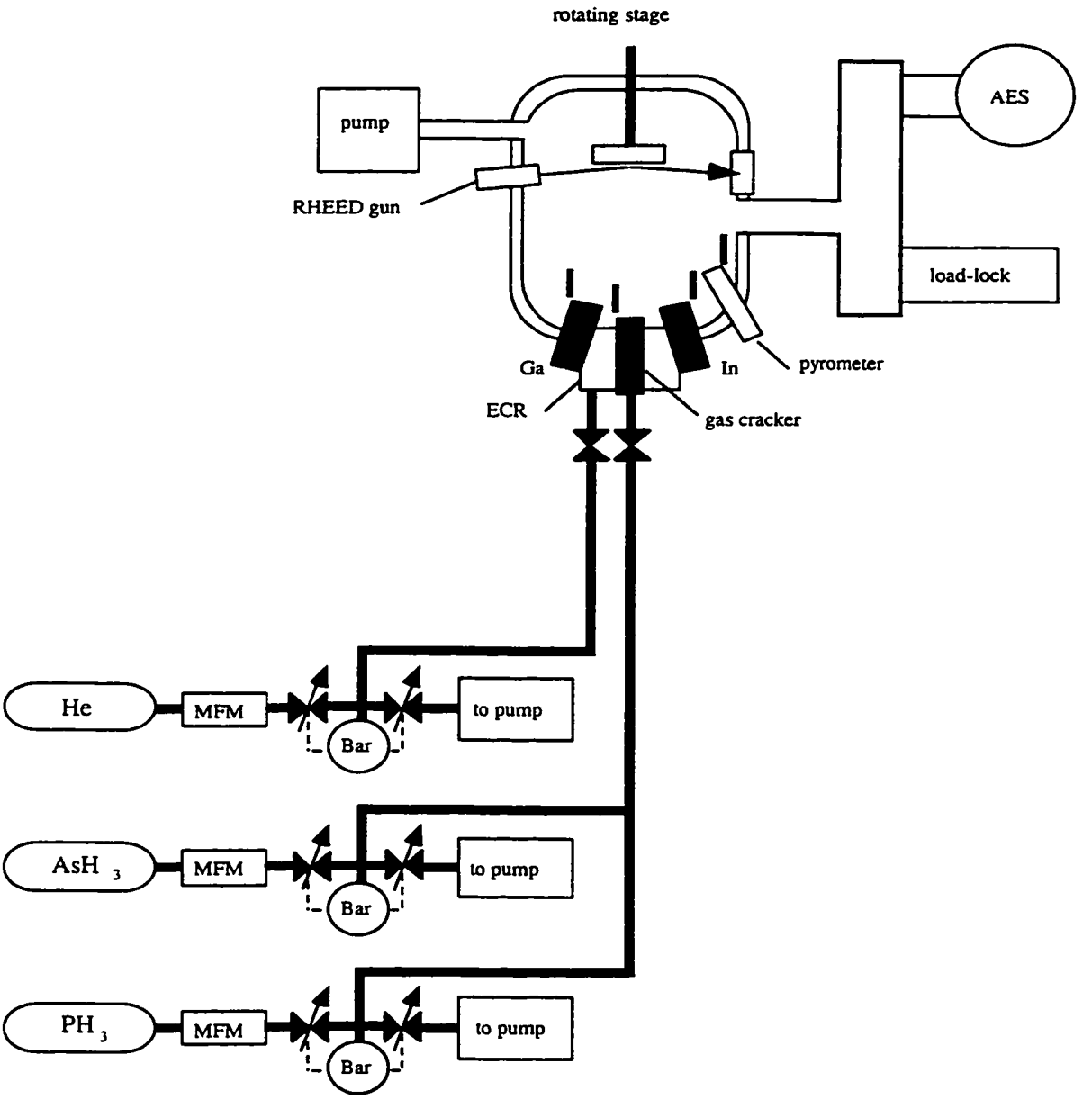

Figure 2.1: McMaster GSMBE system (Modified from a diagram by R.R. LaPierre, used with permission).

tions and as long as the concentration remains below $\sim$ 4x10^{18} cm^{-3}, Si incorporates on the Group III site and acts as a donor. Beyond a concentration of 4x10^{18} cm^{-3}, the Si may occupy some of the Group V sites, causing partial self-compensation. The p-type dopant, beryllium, is in Group II of the periodic table and, therefore, can only act as an acceptor when it incorporates substitutionally. However, for Be concentrations $\gtrsim$ 5x10^{18} cm^{-3}, it can occupy interstitial sites, forming a ($Be_{In} - Be_i$) deep, donor-like complex [Rao et al. (1991)]. Therefore, for this work, the maximum nominal Si doping was 4x10^{18} cm^{-3} and the maximum Be doping was 6x10^{18} cm^{-3}. SIMS studies later revealed that the maximum Si concentration was 3.5x10^{18} cm^{-3}, lower than the expected value. Also, throughout this work, we have assumed that the presence of the He-plasma did not affect how the dopants incorporated. For example, any changes in the electrical behaviour have been attributed solely to defects caused by the plasma, rather than to changes in the dopant behaviour. Finally, the doping concentration may have an associated error of $\pm$10%.

2.1.2 Electron-Cyclotron Plasma Generation System

The He-plasma is generated inside the chamber by a Microscience ECR-900 series electron-cyclotron resonance (ECR) source. Helium gas is passed into the plasma generation chamber from an external gas cylinder at a gas flow of 7 sccm. An initial spontaneous ionization event is required to start the plasma generation process. Microwave power at a frequency of 2.45 GHz is guided into the chamber (absorbed power of approximately 100-150 W), causing the electrons to oscillate. An axial magnetic field of 875 Gauss, chosen to correspond to the resonance condition for 2.45 GHz, is also applied which causes the electrons to spiral around the flux lines, thereby increasing their path length and the number of electron-electron collisions and thereby, the density of ionized and excited gas atoms. The average energy of the plasma particles

extracted from the source is 25 to 30 eV. As a result of the high hydrogen pressure produced in the dissociation of the Group V hydrides, there is also a hydrogen plasma component present during operation of the ECR source, due to backstreaming of H_2 from the MBE chamber into the ECR plasma chamber [Mitchell (1995)].

2.1.3 Rapid Thermal Annealer (RTA)

Annealing provides a controllable method of removing defects from a sample; if the temperature is high enough, defects can gain enough thermal energy to diffuse towards the surface or other defects. By annealing the sample at a number of temperatures, it is possible to correlate changes to one material property, such as the resistivity, with other observed changes, in defect size, for example.

Using a standard procedure, many of the samples in this study were subjected to rapid thermal anneals of 10 seconds duration, ranging in temperature from 500 to 800 $\pm$10 °C. The sample is placed on a Si wafer platform, inside the quartz furnace chamber, as close as possible to the thermocouple monitoring the temperature. A piece of n-InP wafer is placed on top of the sample to act as a capping layer, thereby minimizing phosphorus loss from the surface. The quartz chamber is purged with ultra-high purity nitrogen before and during annealing. The sample is heated to the desired temperature by banks of halogen lamps situated above and below the chamber. The temperature, ramp rate (100°C/second) and anneal time are computer-controlled. After the anneal time has elapsed, the halogen lamps are shut off and the sample is allowed to cool to room temperature before removal from the chamber.

There are a number of advantages of rapid thermal annealing versus furnace annealing [Wood (1994)]. The RTA process is much quicker, with anneal times of seconds versus an hour in a standard furnace, and hence dopant diffusion is reduced. Also, contamination from the quartz is minimal, because the wavelength of the halo-

gen lamps is chosen so that the quartz does not heat up.

2.2 Variable Energy Positron Annihilation Technique

Samples were studied at the positron annihilation facility of the Department of Physics and Astronomy at the University of Western Ontario, London, under the guidance of Dr. Peter Simpson. The positron technique allows the study of neutral and negatively-charged vacancy and open-volume defects in the sample. Positively charged defects do not tend to trap the positrons and, therefore, are usually not observed using this technique. This positron technique has a number of very useful advantages in characterizing semiconductor samples [Lawther and Simpson, (1996)]: it is sensitive to defects at a concentration on the order of 10^{16} cm^{-3}; it can differentiate between defects of different size; it provides depth information; it is non-destructive and requires no sample preparation.

The positron beam is generated from a ^{22}Na source. Positrons leave the source at very high energies (up to 546 keV for this source), and are passed through a tungsten foil moderator to slow them to thermal energies. They are subsequently accelerated through an electric field of 0.5 to 60 keV before impinging on the sample, which is mounted inside an evacuated chamber (to reduce scattering of the incident beam). The flux reaching the sample is $\sim$ 10^4 to 10^6 e^+/second. A germanium detector, situated behind the sample, detects the gamma rays produced from the annihilations between the positrons and the electrons in the sample. The resulting gamma spectrum is then analyzed, as described below, to obtain information about the defects. All samples in this study comprised 2 μm thick epilayers grown on semi-insulating substrates, with a surface area of approximately 1cmx1cm. The size of the

sample is not critical, but it must exceed the positron beam diameter (5-6 mm in this case). All measurements were performed at room temperature.

The positrons that enter the sample annihilate with core or valence electrons, producing gamma photons with a mean energy of 511 keV. Some of these gamma photons are Doppler shifted in energy since the electrons in the sample are in motion; therefore, a gamma radiation spectrum is obtained that is centered at 511 keV (Figure 2.2). Valence electrons have a lower momentum than core electrons, so their contribution lies towards the centre of the spectrum. The contribution of the core electrons is manifest mostly in the wings. Using a pre-defined central portion of the spectrum (over the energy range 510.3 to 511.7 keV), a lineshape or "S" parameter can be deduced that reflects the contribution of the valence electrons to the total spectrum (504.5 to 517.5 keV). The central portion of the spectrum is defined such that the S parameter is approximately 0.5 for a defect-free sample. This S value is

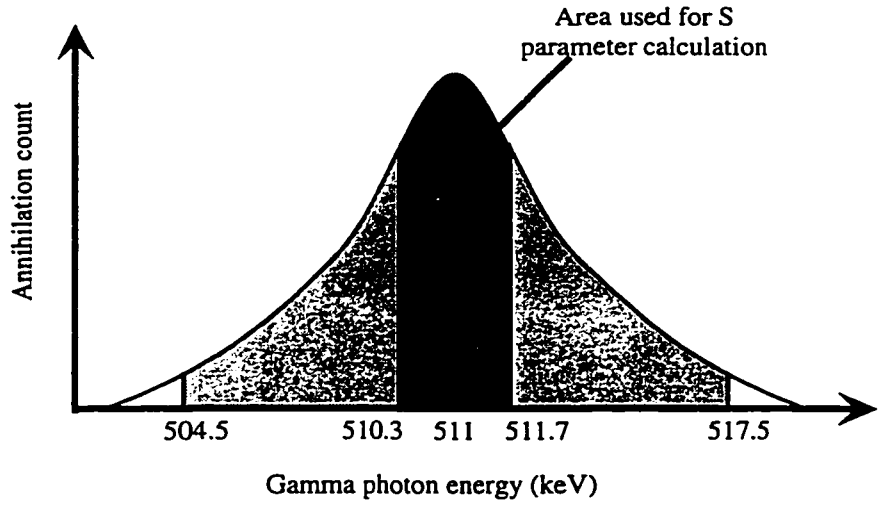

Figure 2.2: The regions used to calculate the S-parameter for positron annihilation studies.

chosen to optimize both the sensitivity to shape change and the statistical precision of the measurements.

The depth profiling is obtained by varying the energy of the incident positrons. The implantation profile of the positron beam can be described by a Gaussian function:

$$P(E,z) = -\frac{d}{dz}[exp[-(z/z_0)^2] \tag{2.1}$$

with a mean implanted depth of

$$\overline{z}(E) = (A/\rho)E^n \tag{2.2}$$

where ρ is the density of the sample and A and n are measured constants, taken to be $A = 4.00\ \mu\text{gcm}^{-2}\text{keV}^{-1.6}$ and $n = 1.6$ for semiconductors [Lawther and Simpson, (1996)]. The density of InP is 4.787 g/cm^3, so positron energies of 10, 20, 30 and 60 keV correspond to probe depths of approximately 0.3, 1.0, 1.9 and 5.9 μm, respectively. Therefore, once positron energies of 60 keV are reached, the beam is probing deep into the substrate. The density of the quaternary is $\sim$5.4 g/cm^3, leading to slightly shallower probe depths.

In a sample with open volume defects, the positrons trap at vacancy sites to maximize their distance from the positive ion cores. Therefore, they tend to annihilate with valence electrons, which increases the S parameter. Also, the S parameter tends to scale with the size of the defects. To obtain a meaningful estimate of the size of the open volume defects present, it is necessary to look at the normalized S parameter, $S_{Epi}/S_{Substrate}$, the ratio of the maximum S value in the epilayer, S_{Epi} to the (defect-free) substrate S value, $S_{Substrate}$ [Saarinen et al. (1998), p.228]. Normalized S ratios of 1.01-1.02 typically indicate monovacancies, 1.03-1.04 indicate divacancies and values of >1.05 indicate larger vacancy clusters [Saarinen et al. (1998), p.234].

2.3 Electrical Characterization

2.3.1 Room-Temperature Hall Effect Measurements

All samples were electrically characterized using room temperature Hall effect measurements. In this way, the resistivity, majority carrier concentration and mobility were obtained. Any traps present in the sample cause the carrier concentration to be reduced. As described later, by studying how the carrier concentration changes with parameters such as doping, we can estimate the defect levels and concentrations. The mobility gives an indication of the flaws in the sample: a reduction implies that the concentration of ionized impurities may have increased.

The standard van der Pauw technique [van der Pauw (1958)] was used to electrically characterize the samples. This technique can be used as long as the contacts are small and placed at the edge of a sample of uniform thickness. The samples consisted of 2 μm thick epilayers grown on semi-insulating (Fe-doped) InP substrates. These substrates have a resistivity greater than $1x10^7$ Ω-cm and a mobility between 2200 and 2700 cm^2/Vs, and are 350 μm thick. Samples were cleaved into (4±0.01) mm x (4±0.01) mm squares. The appropriate contacts, Sn for n-type samples and 95:5 In:Zn for p-type samples, were applied to the corners of the samples, and the samples heated until all contacts melted. The contact anneal was carried out in an $HCl:N_2$ atmosphere to prevent surface oxidation. Before loading the sample into the Hall effect apparatus, the resistance of each side of the sample was measured to verify that the contacts were self-consistent and ohmic. If non-ideal behaviour was observed, the contacts were re-annealed and/or re-applied as necessary. Values for the majority carrier concentration, the majority carrier mobility and the sample resistivity were obtained, as described below. Typical values for the measured voltages and currents were $\sim 0.01 - 0.4$ V and $10^{-8} - 10^{-3}$ A (depending on the resistivity of the sample),

respectively.

Resistivity

The resistivity and mobility measurements described below are based on the standard theory by van der Pauw (1958). To find the resistivity of a sample of thickness d, a current is applied between the contacts A and B on one side and the voltage drop across the other pair of contacts, C and D, is measured (see Figure 2.3).

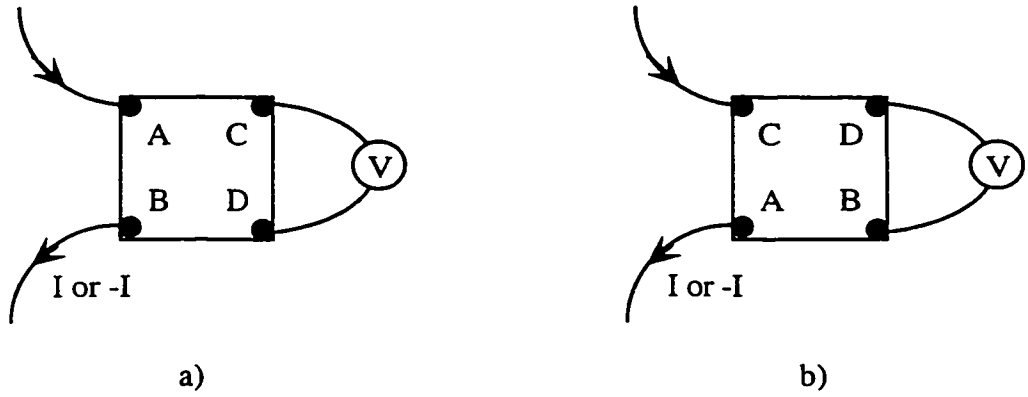

Figure 2.3: Biasing configurations for measuring resistivity a) $|R_{AB.CD}|$, b) $|R_{BD.AC}|$.

The applied current is then reversed and the potential drop measured again. This procedure is repeated, this time with the current applied between contacts A and C and the potential drop measured across B and D. The voltages and currents are combined as follows:

$$R_{AB.CD} = \frac{V_{CD}}{I_{AB}} \tag{2.3}$$

The resistivity, ρ, is then determined from the thickness, d, and the function f:

$$\rho = \frac{\pi d}{ln2}\left(\frac{|R_{AB.CD}| + |R_{BA.CD}| + |R_{BD.AC}| + |R_{DB.AC}|}{2}\right) f\left[\frac{R_{AB.CD}}{R_{BC.DA}}\right] \tag{2.4}$$

where $f[R_{AB.CD}/R_{BC.DA}]$ reflects the symmetry of the sample and is the solution to:

$$\frac{R_{AB.CD} - R_{BC.DA}}{R_{AB.CD} + R_{BC.DA}} = \frac{f}{ln2} arccosh\left[\frac{exp(ln2/f)}{2}\right] \tag{2.5}$$

which approximates unity for a square sample.

The dominant errors in these measurements are due to: i) the estimate of the thickness, d, of the conducting channel; and ii) variability of the contacts, discussed below.

i) Depletion effects: All the calculations in Chapters 3 and 4 assume that the conduction path was 2 μm thick, that is, depletion effects at the surface and at the epilayer-substrate interface have been ignored. This assumption was verified for a specific Si-doped sample as follows: samples of He-InGaAsP (with a room-temperature wavelength of 1.55 μm), doped with 7x10^{17} cm^{-3} Si were grown with thicknesses of 1 and 3 μm. Using the standard Hall effect technique described below, the carrier concentration for both samples was found to be $\sim$ (2.7$\pm$0.1)x10^{17} cm^{-3}, indicating that the depletion width was negligible for this doping level. Therefore, for samples doped more highly than this, the assumption is valid. However, the depletion effect becomes more pronounced as the carrier concentration decreases. For example, n-type InP exhibits a total depletion width of $\sim$1 μm for a free carrier concentration of 10^{15} cm^{-3} and this decreases to $\sim$0.05 μm for a free carrier concentration of 10^{18} cm^{-3}. Therefore, the samples with very low carrier concentrations may be substantially depleted at the surface and growth interface. Since it is not possible to know the depletion width for these samples, this effect has not been factored into the experimental error bars shown on the data plots.

ii) Contact variability: Measurements of the resistance of each side of the square samples indicated that the resistance of a particular side could vary by as much as 10% with respect to the other sides of the square. The measurement errors in the voltage and current readings taken by the Hall effect apparatus are ±0.01% and up to ±0.35%, respectively [Keithley], so are negligible in comparison to the errors introduced by the contacts.

Mobility

To determine the mobility and carrier concentration using the Hall effect, the sample is placed in a magnetic field, B (typically 0.2 Tesla), normal to the surface of the sample. Initially, with a magnetic field of $+B$, a current is applied diagonally across the sample between the contacts A and D and the potential difference between B and C is measured. Then the current is reversed and the voltage drop recorded again. A current is subsequently applied between B and C and the potential drop measured across A and D. The magnetic field is then reversed and all the measurements repeated. By combining the measurements taken for two directions of the magnetic field, the spurious voltages that would otherwise contribute to the measurement error cancel out. The Hall coefficient is calculated for each of the above measurements as follows, for example:

$$R_{H(AD.BC)} = \frac{d}{2B}\left(\frac{V_{BC}(+B)}{I_{AD}(+B)} - \frac{V_{BC}(-B)}{I_{AD}(-B)}\right) \tag{2.6}$$

Finally, the carrier concentration and mobility are given by:

$$n = \frac{1}{R_H e} \tag{2.7}$$

and:

$$\mu = \frac{1}{ne\rho} \tag{2.8}$$

where

$$R_H = \frac{R_{H(AD.BC)} + R_{H(DA.BC)} + R_{H(BC.AD)} + R_{H(BC.DA)}}{4}. \tag{2.9}$$

As for the resistivity measurements, the major source of error for the mobility measurements is the estimate of the thickness of the conducting channel, as discussed earlier. Also, the magnetic field can decrease over time by as much as 5%.

In InP there are three major contributors to the electron mobility: polar-optical, deformation potential acoustical and ionized impurity scattering [Walukiewicz et al. (1980)]. Standard, undoped InP grown at McMaster university has a free carrier mobility of $\sim$ 4800 cm^2/Vs.

Leheny et al. (1980) investigated undoped quaternary alloys $In_{1-x}Ga_xAs_yP_{1-y}$ (where x, $1-x$, y and $1-y$ denote the mole fraction of gallium, indium, arsenic and phosphorus respectively) over the full composition range from InP to InGaAs. The room-temperature mobilities started at approximately 3700 cm^2/Vs for InP, decreased slightly as y approached 0.3 and then rose steadily to a value of 11,000 cm^2/Vs for InGaAs. They surmised that alloy scattering was the most important factor for most of the quaternary range. Shibli and Garcia de Carvalho (1988) performed low-temperature Hall effect measurements (from 4.2 K to room-temperature) on Sn doped (n) InGaAsP (E_g = 0.96 eV). The mobility at room-temperature was approximately 1x10^3 to 3x10^3 cm^2/Vs and the dominant scattering mechanisms were polar optical phonons and alloy scattering. P-type $In_{1-x}Ga_xAs_yP_{1-y}$ samples were studied by Hayes et al. (1980) using room-temperature Hall effect measurements. They found that over most of the composition range (y = 0 to 1 with $y = 2.1x$ to maintain lattice matched conditions) the hole mobility at room temperature was dominated by alloy scattering. The mobilities varied between 80 to 180 cm^2/Vs. Other contributing factors were ionized impurity scattering (more prevalent at T<130 K), non-polar optical,

acoustic optical and polar optical scattering.

2.3.2 Variable-Temperature Hall Effect Measurements

The results from the room-temperature Hall effect measurements were subsequently fitted with a Fermi statistics model (see Chapter 5), which indicated that a number of defect energy levels were present in the sample. As additional confirmation of the model, Hall effect measurements were made on a Be-doped ($3x10^{17}$ cm^{-3}) quaternary sample over the temperature range -25 to +100 ($\pm$0.1) °C. A comparison was then made between the model prediction and the experimental data for a sample at different temperatures.

For these measurements, the sample was mounted on a cold finger inside an evacuated chamber. The chamber was maintained at a pressure of <50 mTorr with a mechanical pump. Thermal contact was maintained between the sample and the mount using thermal paste. However, it is possible that the sample was warmer than indicated by the thermocouple mounted inside the cold finger and this would introduce a systematic error into the results. The temperature of the cold finger was increased by electrical heating. Once the desired temperature had been reached, the sample was allowed to stabilize for 5 to 10 minutes before the reading was taken. As for the room-temperature measurements, the carrier concentration, mobility and resistivity were recorded.

The analysis of temperature-dependent measurements usually assumes that only one major acceptor and one major donor control the electrical behaviour of the sample [Bourgoin and Lannoo (1983), p. 125]. With this assumption, and as long as the temperature range is chosen such that $n \ll N_A$ and $n \ll N_D - N_A$, the relation between the carrier concentration and donor defect level is [Bourgoin and Lannoo

(1983), p. 127]:

$$n = \frac{N_C(N_D - N_A)}{2N_A} e^{-E_D/kT} \tag{2.10}$$

By plotting the data in the form $ln(n)$ versus $1/kT$, the energy level of the controlling donor-like defect, $-E_D$, can be calculated from the slope of the line. However, as will be discussed in Chapter 5, this approach is not an accurate description for the He-plasma-assisted materials, since a number of defect levels appear to be present in these samples. Therefore, the experimental results of these measurements (discussed in Chapter 4) will be compared to the results generated from the computer model. Also, care needs to be taken both in the experimental measurement itself and in the interpretation of the results. For example, contacts that are adequate at room temperature may no longer be ohmic at lower temperatures. According to Jaros [1980], substantial corrections may be required to the binding energies obtained from Hall effect measurements, since at finite temperatures, the energy involved in the release of a particle from a bound state into a band corresponds to a change in the Gibbs free energy, $\Delta F = \Delta H + T\Delta S$, which involves an entropy term as well as the enthalpy. The analysis is further complicated by the fact that the temperature dependence of the deep level in the gap may not be simply related to the temperature dependence of the band gap of the host material, making estimates of its position inaccurate.

2.3.3 N-i-n Measurements

The very high resistivity of the He-InP samples means that Hall effect measurements are unreliable due to the low carrier concentrations and unknown depletion effects. To gain a better estimate of the resistivity and to verify the trends observed from Hall effect measurements, n-i-n resistor structures were fabricated. The work

described herein is a continuation of the work started at McMaster University by Robinson et al. (1997).

The devices consisted of a layer of He-plasma material sandwiched between two Si-doped ($1x10^{18}$ cm^{-3}) layers of standard material to form a resistor structure on an n-type InP substrate. A layer of highly Si-doped InGaAs ($4x10^{18}$ cm^{-3}) was grown on top of the InP to ensure an ohmic contact was formed with the metal contact. Circular metal alloy contacts of different radii (60, 100, 200 and 300 μm) were then deposited on the top surface and 7000 Å deep mesas were etched, using the contacts as a mask, to form isolated devices. A back contact was alloyed on the underside of the substrate. The device structure is shown in Figure 2.4.

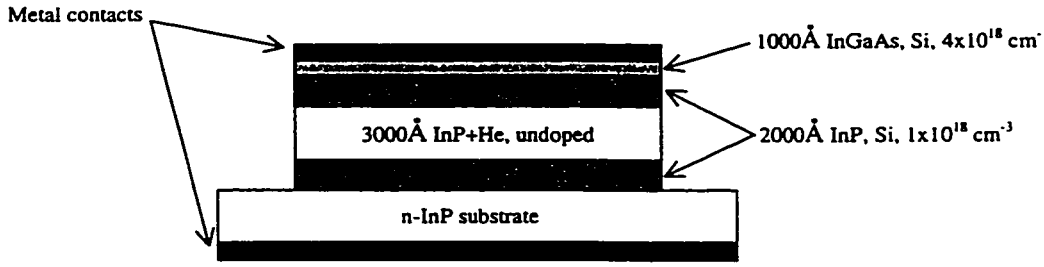

Figure 2.4: N-i-n device structure for electrical measurements

Measurements were taken for undoped and lightly Be-doped InP. The Be doping was kept below $2x10^{18}$ cm^{-3} so that the He-material remained n-type. For "insulating" materials, only the low voltage regions of the I-V curve are ohmic [Lampert and Mark (1970)]; at higher voltages the injected carriers dominate the thermal carriers, leading to a non-linear current-voltage relationship of the form $I \propto V^2$. Hence, I-V measurements were taken for voltages of 1-100 mV (the linear range) over the temperature range 200 to 375 ($\pm$0.2)K. Silver paste was used for thermal and

electrical contact between the devices and the cold finger. Using this technique, both the room temperature resistivity and the "activation" energy could be estimated. To obtain an estimate of the activation energy (enthalpy) for carriers in SI GaAs, Tang et al. (1989) plotted the carrier concentration from Hall effect measurements versus 1/T, since they are related as follows:

$$n_0 = AT^{3/2}e^{-\Delta H/kT} \tag{2.11}$$

From the n-i-n devices, we obtain only the resistivity, but this can be accommodated by modifying the theory found in Tang et al. (1989), as follows:

$$\rho(T) = \frac{1}{en_0(T)\mu_n(T)}, \tag{2.12}$$

therefore,

$$\rho(T) = (1/Ae\mu_n)T^{-3/2}e^{\Delta H/kT} \tag{2.13}$$

where ρ is the resistivity of the sample at a given temperature, n_0 is the carrier concentration, μ_n is the mobility, A is a constant of proportionality, T is the temperature in K, ΔH is the activation energy of the trap and k is the Boltzmann constant. By plotting $\ln(T^{3/2}\rho)$ versus $1/T$, the activation energy can be found from the slope, if the carrier mobility is assumed to be constant. Samples were also studied after annealing to see whether the changes in resistivity observed in these devices confirmed the results obtained from the Hall effect studies. Experimental error would be introduced in the measurement of the currents ($\pm 1\%$) and voltages ($\pm 0.1\%$) [Hewlett-Packard] used to calculate resistance. However, these are negligible compared to contact resistance or temperature inaccuracies. For example, the sample may not be at the same temperature as the cold finger and this would introduce an error into all measurements. Also, there is error in the linear fit. Therefore, a total possible error of 10% will be quoted with the data.

2.4 Low-Temperature Photoluminescence Technique

A number of He-quaternary samples were studied using photoluminescence. For this technique, an optical source is used to promote electrons from the valence band to the conduction band. The incident photons must have an energy greater than the bandgap of the sample. The electrons and holes generated by this process then recombine via radiative and non-radiative pathways. By collecting the luminescence that the sample emits, we can obtain the photon energy of any radiative processes taking place, including transitions involving defect levels in the bandgap.

The photoluminescence apparatus at McMaster University, shown in Figure 2.5. The samples are mounted on a brass block that sits on a cold finger inside the chamber. The cold finger is cooled by a He compressor. To obtain the lowest cold finger temperature of (16±2) K and prevent frosting of the chamber window,

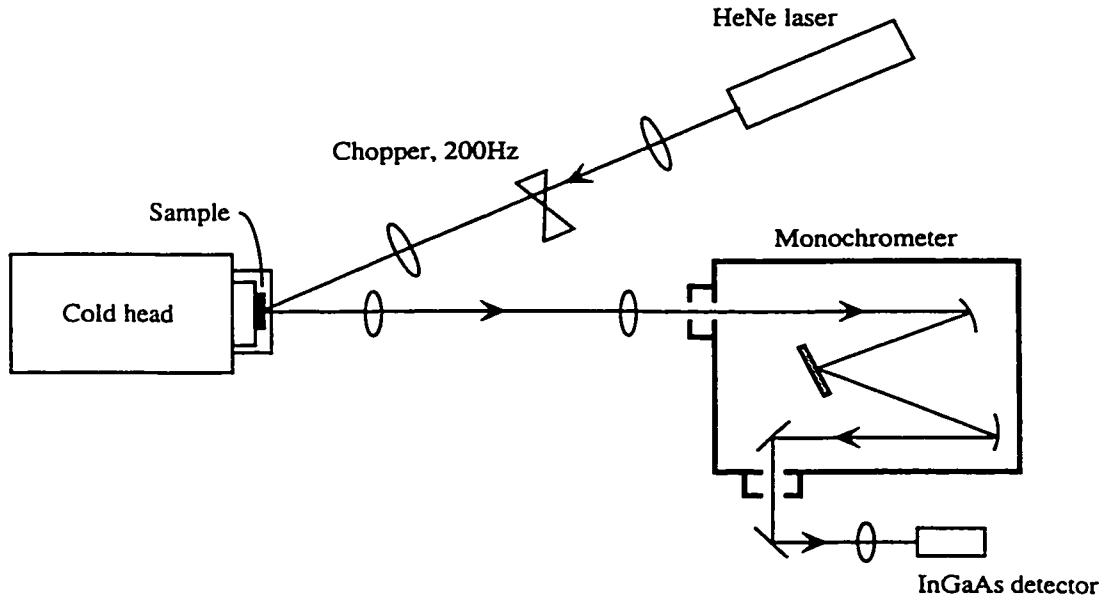

Figure 2.5: Low-temperature photoluminescence system

the chamber is pumped down to a pressure of < 50 mTorr. The excitation source is a HeNe laser, operating at a power of 10.4 mW and a wavelength of 632.8 nm. The laser beam passes through a number of lenses to focus the beam to a small spot and to allow positioning of the beam on the sample. The incident laser light is chopped at a frequency of 200 Hz to allow measurements to be taken with a lock-in amplifier, thereby improving the signal-to-noise ratio. The photoluminescence generated from the surface of the sample is collected by a lens positioned as close as possible to the chamber window. This luminescence then passes through another lens, chosen to match the f-number of the monochrometer. On passing through the monochrometer, the light is diffracted from a grating of 600 lines/mm that can be rotated to allow the desired wavelength of light to pass through the exit slit to the InGaAs detector, sensitive over the range 1200 to 1700 nm. The input and exit slits were set to a width of 500 μm. Readings were taken every 2$\pm$0.2 nm.

For a high-quality standard sample (with few defects), the dominant feature of the PL spectrum would be the bandgap excitonic transition with an energy close to that of the bandgap of the material. We must remember, however, that changing the temperature of the sample also changes the bandgap and the wavelength observed for low sample temperatures will be different to the room-temperature value. The bandgap energy is related to the sample temperature by the Varshni equation [Varshni, (1967)]:

$$E(T) = E(0) - \frac{\alpha T^2}{(\beta + T)} \tag{2.14}$$

where $E(0)$ is the band gap at 0 K, T is the temperature in K and α and β are material parameters. For the quaternary alloys, the coefficients were experimentally determined to be $\alpha = 4.9\text{x}10^{-4}$ eV/K and $\beta = 327$ K (the same as for InP) [Temkin et al. (1981)]. This means that the low-temperature (15 K) bandgap energy is approxi-

mately 67 meV larger than the room temperature bandgap energy. Transitions seen at energies lower than the bandgap energy are due to recombination via energy levels in the bandgap: donor-acceptor, donor-valence band or conduction band-acceptor, for example. In a sample with few substitutional impurities, these lower energy transitions may indicate radiative recombination involving native defect states. However, deep traps (those that lie more than $\sim$ 200 meV from the conduction or valence band-edge) are often non-radiative recombination centres, so these trap levels are often absent from the PL spectrum. Such samples may exhibit very little photoluminescence. The PL linewidth for band-edge emission for standard quaternaries grown on InP substrates is given by approximately kT for PL temperatures below 200 K and 1.7 to 1.9 kT for PL temperatures above 200 K [Temkin et al. (1981)]. Broader peaks may indicate recombinations involving bandgap states.

2.5 SIMS Technique

As mentioned previously, there is always hydrogen present in the MBE growth chamber due to the dissociation of the group V hydride sources. This means that hydrogen may backstream into the ECR source during operation and may inadvertently be present in the helium plasma. Previous work [Mitchell et al. (1995)] indicated that a hydrogen plasma causes InP to be more conductive. Also, the dopant, Be, is known to be passivated by hydrogen. To determine whether hydrogen was present in the He-plasma-assisted material, a number of samples were sent to the Advanced Technology Group at Nortel Networks, Ottawa for SIMS measurements by Dr. R.W. Streater.

The SIMS technique measures the concentration of elements in the sample as a function of depth. For example, it can be used to verify a dopant concentration or determine the presence of an impurity, provided that the concentration exceeds

the minimum detection level of the SIMS apparatus. In this system, the samples are bombarded with caesium, and the resulting ions displaced from the surface are analyzed in a mass spectrometer. Measurements as a function of sputtering time allow a concentration profile to be generated as a function of depth.

For this work, we wished to determine the concentration of hydrogen in the samples. However, the detection minimum for hydrogen as H_2 is on the order of 10^{17} cm^{-3}, and it was quite possible that the levels of hydrogen in the material could be substantially lower. To facilitate measurements of lower concentrations, special samples were grown in the presence of deuterium gas. Deuterium has an extra neutron in the nucleus compared to hydrogen and is chemically identical to H_2. Using D_2 as the element detected, a lower minimum detection limit of $\sim 10^{-15}$ cm^{-3} can be achieved. During these special growth runs, the MBE growth chamber pressure was $1x10^{-4}$ to $2x10^{-4}$ Torr, a factor of $2-4$ times the usual growth background pressure of $5x10^{-5}$ Torr. The amount of hydrogen incorporated in the sample was estimated by appropriate scaling of the SIMS deuterium value. This is discussed in more detail with the relevant experimental results.

Chapter 3

Experimental Results for InP

3.1 Introduction

Indium phosphide is the seemingly obvious choice for the study of this growth technique, since it only contains two elements. Moreover, we have some prior knowledge of this system from the work by Mitchell (1995). This chapter describes the characterization of He-InP using positron annihilation spectroscopy, Hall effect and n-i-n electrical measurements and SIMS analysis. Samples were studied as-grown and after anneal at a variety of temperatures. The effect of weak Be-doping was also included. The summary relates the findings of the experiments to independent results from Dr. Jin Ung Kang at the Optical Sciences Division of the Naval Research Laboratory in Washington, D.C. and discusses the difficulties of working with He-plasma-assisted InP.

3.2 Positron Results

Two He-InP samples were studied using positron annihilation spectroscopy: one undoped and the other doped with $3x10^{17}$ cm^{-3} Be. Two controls (one undoped and the other doped with $3x10^{17}$ cm^{-3} Be), grown under standard conditions (with no He plasma), were also studied. The samples are summarized in Table 3.1. All

samples were studied as-grown (pre-anneal) and after each of a number of 10 second rapid thermal anneals at 550, 650 and 700°C.

MBE no.	Description	Dopant (cm^{-3})
2158	InP + He plasma	None
2122	InP standard (no plasma)	None
2159	InP + He plasma	Be, $3x10^{17}$ (nominal)
1762	InP standard (no plasma)	Be, $3x10^{17}$ (nominal)

Table 3.1: InP samples studied with the variable energy positron annihilation technique

3.2.1 Standard InP

Figure 3.1 shows how the undoped standard InP sample, 2122, behaved on anneal. The peak S-parameter of the as-grown sample was approximately 0.503, as expected for a defect-free sample (see Section 2.2), and this value did not change with anneal, indicating that no defects were created by the rapid thermal annealing process. Similar results were obtained for the Be-doped standard sample, 1762, as-grown and after all annealing steps, as illustrated in Figure 3.2. The peak S-parameter was approximately 0.505 for the un-annealed sample and did not change with anneal.

3.2.2 He-Plasma InP

Figure 3.3 shows the S parameter for the undoped He-plasma InP sample, 2158 (denoted as He-InP below), as-grown and after all anneals. This sample exhibited very different behaviour compared to the standard InP sample. A peak appears in the S-parameter at low positron energies (10-20 keV, or a depth of 0.3-1.0 μm) that corresponds to annihilations in the epitaxial layer. The peak S-parameter of the as-grown He-InP sample was ~0.527, giving a normalized S-parameter, $S_{Epi}/S_{Substrate}$ of 1.045, which indicates that open volume defects, probably in the form of single and

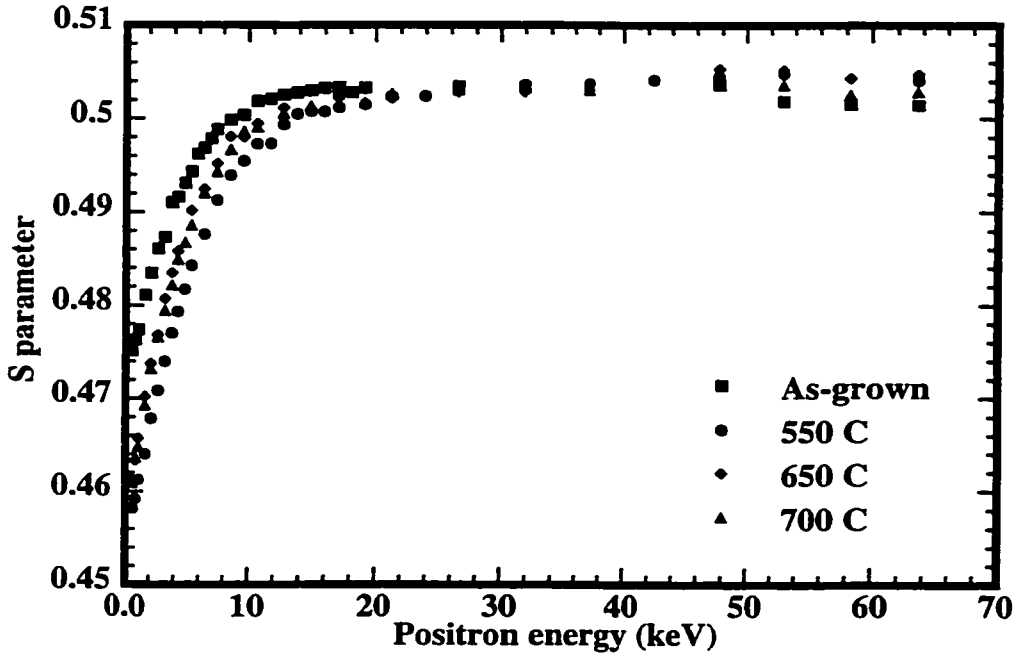

Figure 3.1: Positron annihilation results for undoped standard InP sample, as-grown and after all anneals.

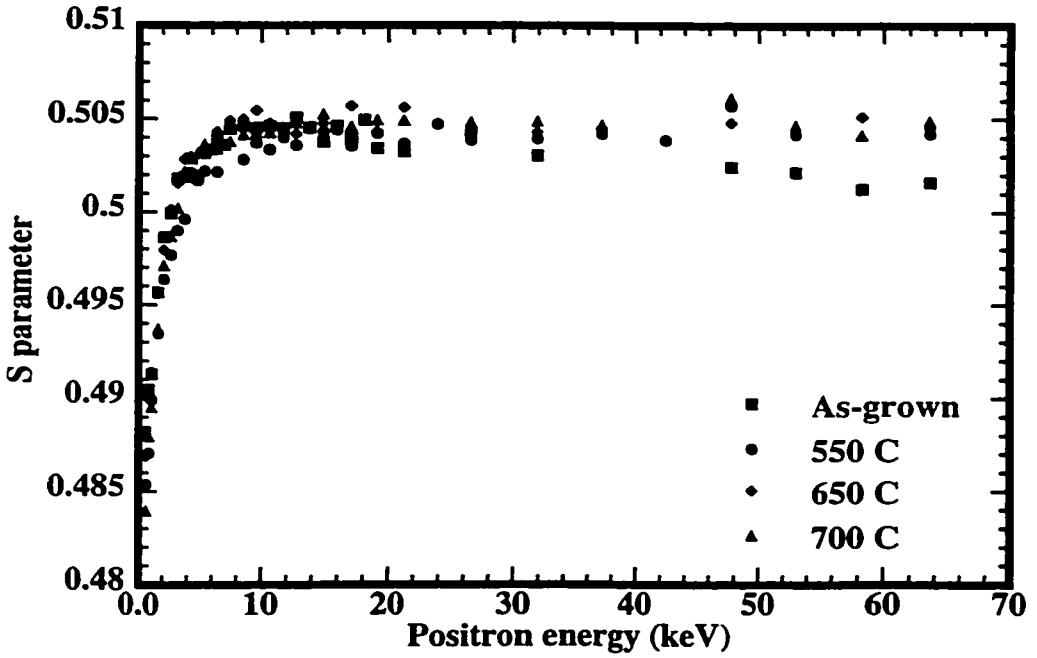

Figure 3.2: Positron annihilation results for Be-doped InP standard sample, as-grown and after all anneals.

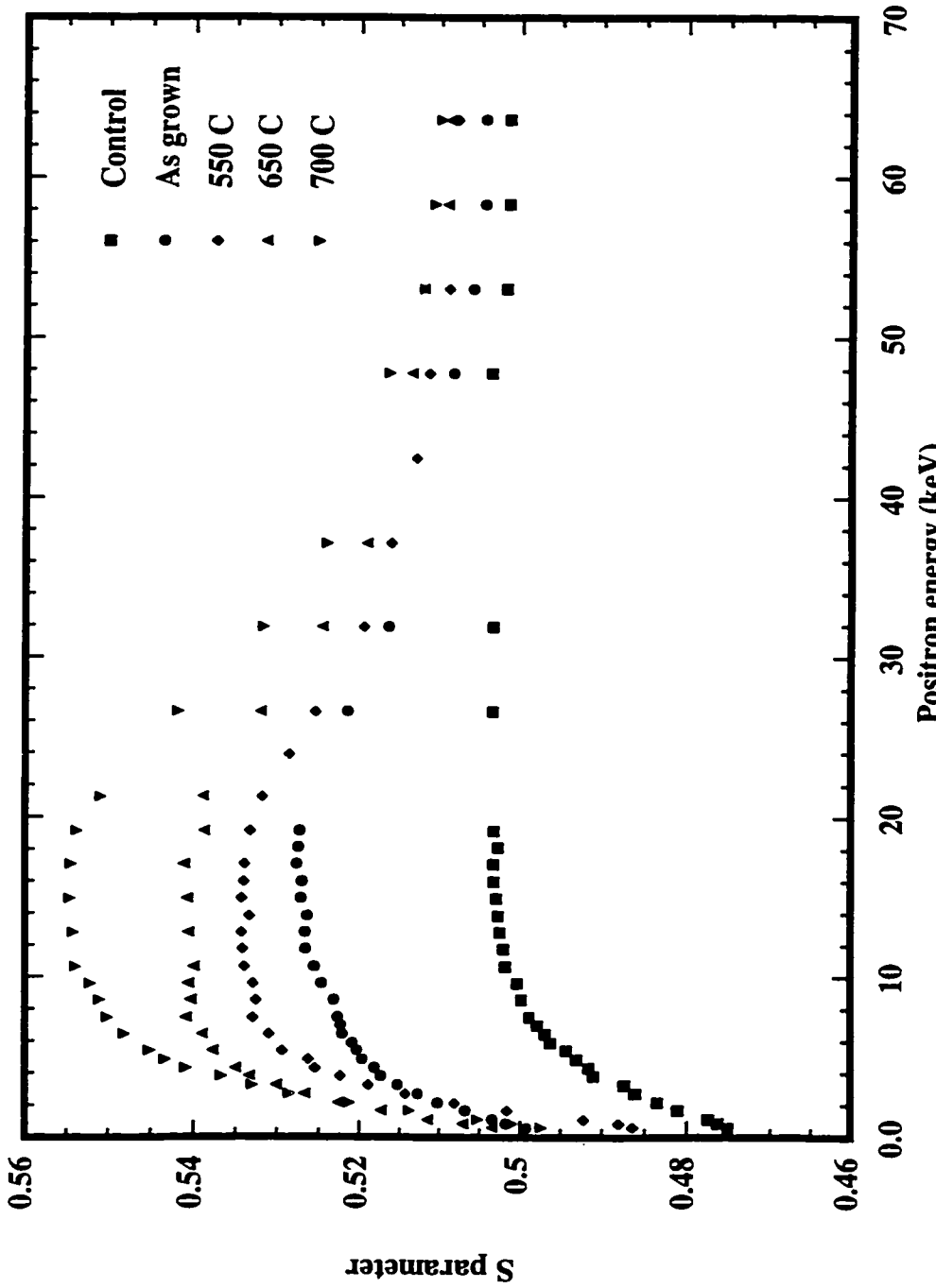

Figure 3.3: Positron annihilation results for undoped He-InP sample, as-grown and after all anneals.

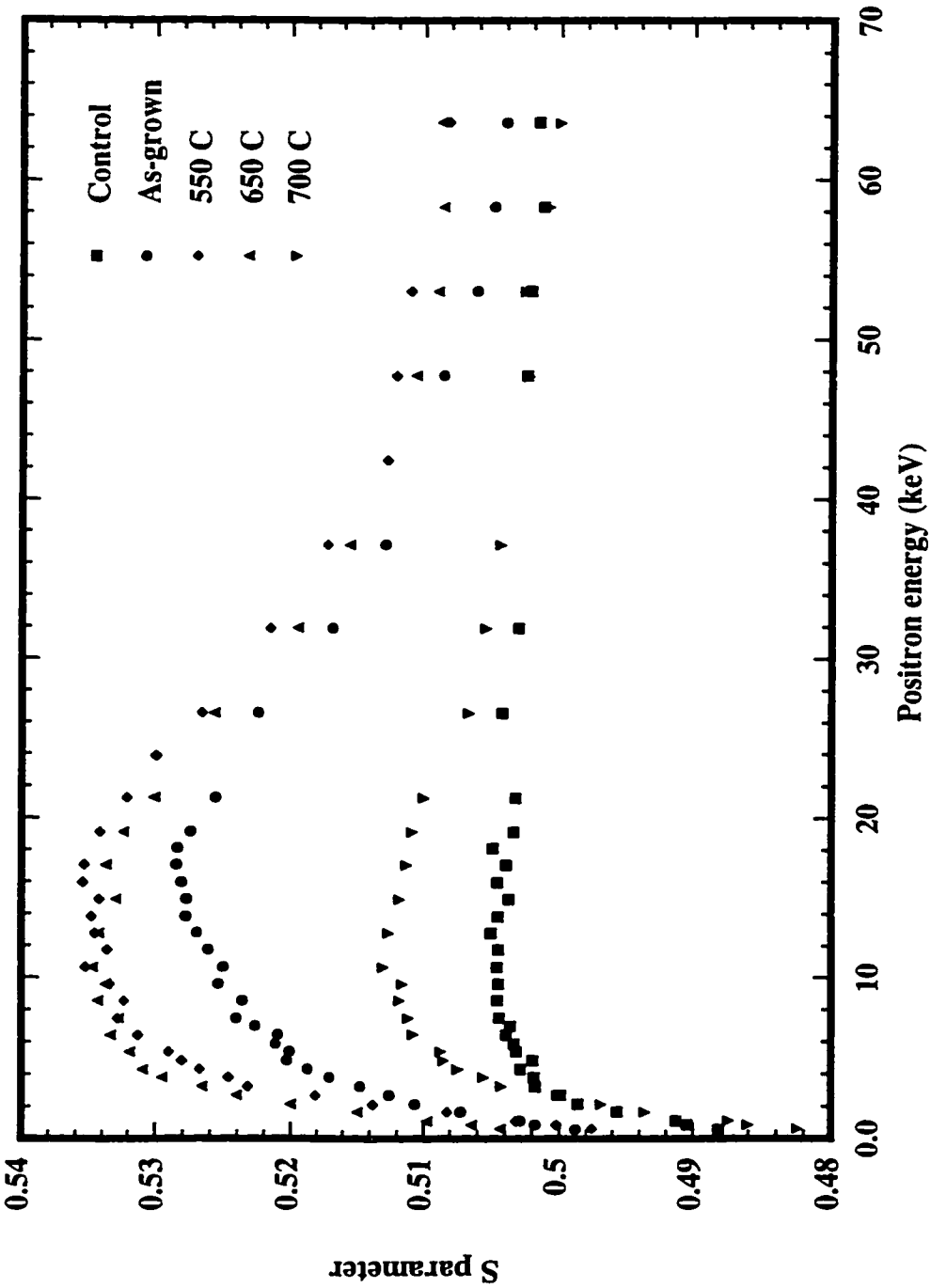

Figure 3.4: Positron annihilation results for Be-doped ($3x10^{17}$ cm^{-3}) He-InP sample, as-grown and after all anneals.

divacancies [Saarinen et al. (1998), p.234], were created in the sample during growth by the impact of the plasma particles. The peak S-parameter increased steadily on anneal to ~0.555, to yield $S_{Epi}/S_{Substrate}$=1.09, for the highest temperature anneal at 700°C. Since the S-parameter tends to scale with volume of the defect, this increase suggests that the small defects created during growth clustered into larger open volume defects during annealing [Saarinen et al. (1998)].

The anneal behaviour of the Be-doped He-InP sample, 2159, is shown in Figure 3.4. The as-grown Be-doped sample appeared very similar to the as-grown undoped He-InP sample, with a peak S-parameter of approximately 0.527, yielding $S_{Epi}/S_{Substrate}$=1.045. After anneal at 550°C, this value increased to 0.535, or $S_{Epi}/S_{Substrate}$=1.053, in a similar way to the undoped He-InP sample. Annealing at 650°C did not change the S-parameter appreciably. However, after anneal at 700°C, the S parameter suddenly decreased to a value of 0.513, ($S_{Epi}/S_{Substrate}$=1.026), lower than the S-parameter for the as-grown sample. This behaviour suggests that either the presence of the Be caused the break up of the defect clusters formed at lower anneal temperatures or the defects have become positively-charged and therefore, inefficient positron trapping centres. Given the behaviour of the sample at low anneal temperatures, the latter seems more likely. Also, studies by other researchers [Chen et al. (1996)] have indicated that the sensitivity of the positron annihilation technique to certain defects may depend on the doping of the sample, since the charge state of a defect depends on the position of the Fermi level. They concluded that only indium vacancies would be observed in p-type InP, since the phosphorus vacancies would be positively-charged when the Fermi energy was below mid-gap, but that both types of vacancies (In and P) would be seen in n-type or SI-InP. Later, the electrical behaviour of the samples will show that changes to the Fermi energy do occur on anneal; the

electron concentration decreases, implying that the Fermi level has moved toward the valence band. Therefore, it is possible that a donor-like defect is responsible for the decrease in the S-parameter.

3.3 Hall Effect Measurements

Corresponding room-temperature Hall effect measurements were made on the same materials (samples 1762, 2122, 2158 and 2159) studied with the positron annihilation technique. The Hall effect samples underwent rapid thermal annealing alongside the positron samples to ensure that the conditions were identical. The standard van der Pauw technique was used as described in Section 2.3.

The as-grown undoped standard InP sample, 2122, exhibited an electron concentration of $\sim 10^{15}$ cm^{-3} and mobility of $\sim$ 4500 to 4850 cm^2/Vs, as expected for standard undoped material. The Be-doped standard InP sample, 1762, exhibited a hole concentration of $\sim 5x10^{17}$ cm^{-3} and a mobility of $\sim$ 70 to 100 cm^2/Vs. As expected, these values did not change appreciably with annealing for either sample.

Figure 3.5 shows the carrier concentration and mobility for the undoped He-InP sample as a function of anneal temperature. Reliable measurements could not be obtained for the sample annealed at 700°C, so the data have not been included. The curve fit is provided as a guide only; due to the limited number of experimental points, the shape of the curve cannot be known accurately. The as-grown sample was weakly n-type with a carrier concentration and mobility of $\sim 6x10^{11}$ cm^{-3} and 940 cm^2/Vs respectively. These values are much lower than those for standard InP, implying that electron traps are formed during the He-plasma-assisted growth process. The carrier concentration decreased further on anneal to $\sim 5x10^{10}$ cm^{-3} after 10 seconds at 550°C, and 10^{11} cm^{-3} after 10 seconds at 650°C. At the same time, however, the

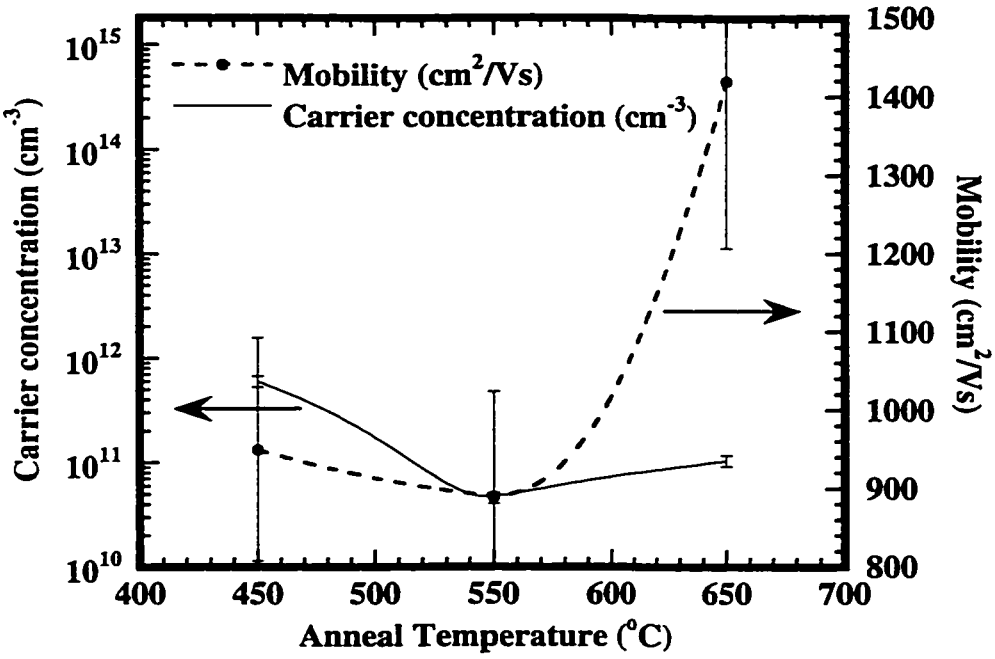

Figure 3.5: Hall effect measurements for undoped He-InP sample, as-grown and after all anneals. The as-grown sample is represented at T=450°C, the growth temperature.

mobility increased quite rapidly, from 900 to 1400 cm^2/Vs, suggesting a reduction in the concentration of ionized impurities, such as defects, that cause scattering of the free carriers. The decrease in free electron concentration and concurrent increase in mobility may imply that donor-like defects have been removed on anneal.

Figure 3.6 shows the results for the Be-doped He-InP sample. Despite the presence of the acceptor-type dopant, the as-grown sample was weakly n-type, as can be seen from the relatively high mobility of 1000 cm^2/Vs. Therefore, the Be was not electrically active, because it was either passivated or compensated. Hydrogen is known to passivate acceptors in InP and could be playing a role in this material, since there is always hydrogen in the chamber during growth due to the thermal dissociation of the phosphorus hydride, PH_3. Alternatively, compensation of the Be would imply the presence of deep donors that act as hole traps. This type of behaviour has been

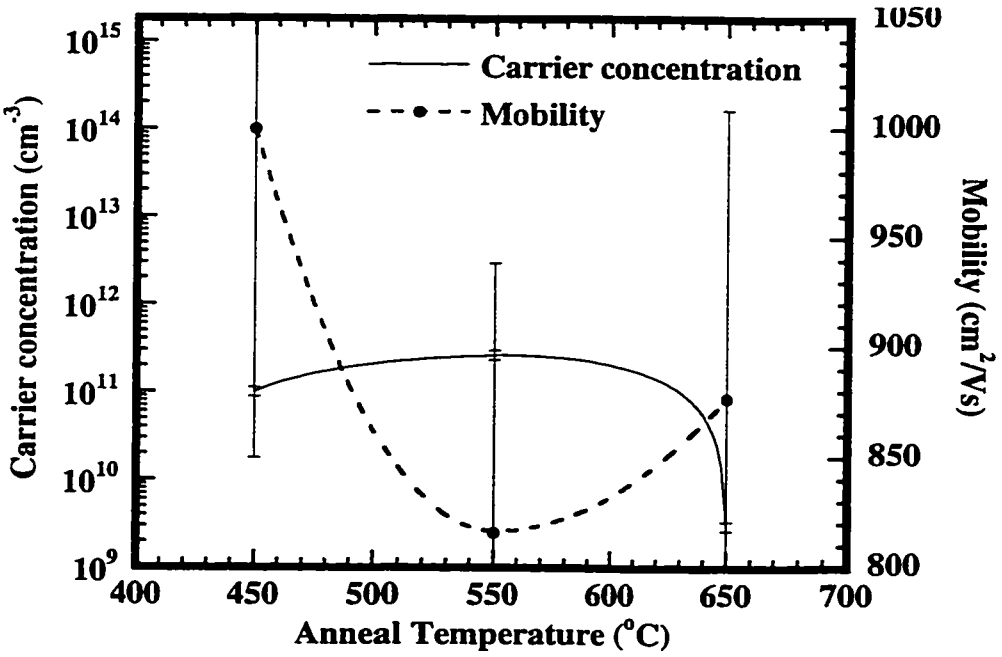

Figure 3.6: Hall effect measurements for Be-doped He-InP sample, as-grown and after all anneals.

observed in Be-doped LTG GaAs [Atique et al. (1995), Bliss et al. (1992a,b), O'Hagan and Missous (1994)]. Bliss et al. (1992a,b) proposed that the Be was compensated by high concentrations of the donor-like As_{Ga} defects. As discussed in Section 3.5, SIMS results revealed that hydrogen is not the likely cause of the Be inactivity, from which we can conclude that donor-like defects may be present. The electron concentration of the as-grown Be-doped sample was $\sim 10^{11}$ cm^{-3}, lower than that of the as-grown undoped He-InP sample, which implies that a certain fraction of the Be must be electrically active in order to pull down the Fermi level. The sample remained n-type after both anneal steps of 550 and 650 °C with the carrier concentration decreasing to $\sim$ 3x10^9 cm^{-3} after the 650°C anneal. The fact that the p-type nature of the Be was still not evident means that annealing at 650°C was not sufficient to remove a substantial fraction of the deep donors present after growth. The mobility decreased

after the 550°C anneal, but recovered slightly for the higher anneal temperature. The sample annealed at 700 °C was too resistive to obtain consistent results, so the data have been omitted.

From these results we can conclude that the He-plasma-assisted growth technique causes increased resistivity in InP and that these characteristics become more pronounced with annealing and light Be doping. The high resistivity of the undoped material implies the presence of electron traps. It also seems likely that a donor-like defect is present to compensate the Be doping. However, the extremely low carrier concentrations mean that the Hall effect results are unreliable. For these samples, the Hall effect apparatus was operating at its sensitivity limit, the samples may have been highly depleted and the SI-InP substrate may have been taking part in conduction. To confirm the behaviour of the He-InP samples required an alternative method to determine the resistivity, as discussed in the following section.

3.4 N-i-n Results

We saw from the Hall effect measurements that estimates of the resistivity are difficult due to the low carrier concentrations involved. Therefore, n-i-n devices were fabricated as described in Section 2.3, with nominally undoped or Be-doped ($1x10^{18}$ cm^{-3}) He-InP as the "intrinsic" layer. SIMS studies later revealed that this "intrinsic" layer also contained Si at a concentration of $\sim 4x10^{16}$ cm^{-3}, approximately ten times the concentration found in the substrate. In order to confirm the increases in resistivity with anneal, similar devices were also fabricated from undoped He-InP that had been previously rapid thermal annealed for 10 seconds at 550 and 650°C.

Figure 3.7 shows the temperature-dependent resistivity results for the as-grown Be-doped and undoped He-InP samples. The plot for undoped He-InP shows

two regions of different slope: a steep slope for sample temperatures above 250K (that is, for $1000/T \leq 4$) and a shallower slope below this temperature (for $1000/T > 4$). Bliss et al. (1992a) also saw two distinct slopes when they conducted temperature-dependent resistivity measurements on LTG GaAs samples. They attributed the above-room-temperature slope to free-carrier conduction due to thermally-excited electrons from the Fermi energy pinned at the mid-gap defect level. The slope for temperatures lower than room temperature was assigned to thermally-assisted hop-

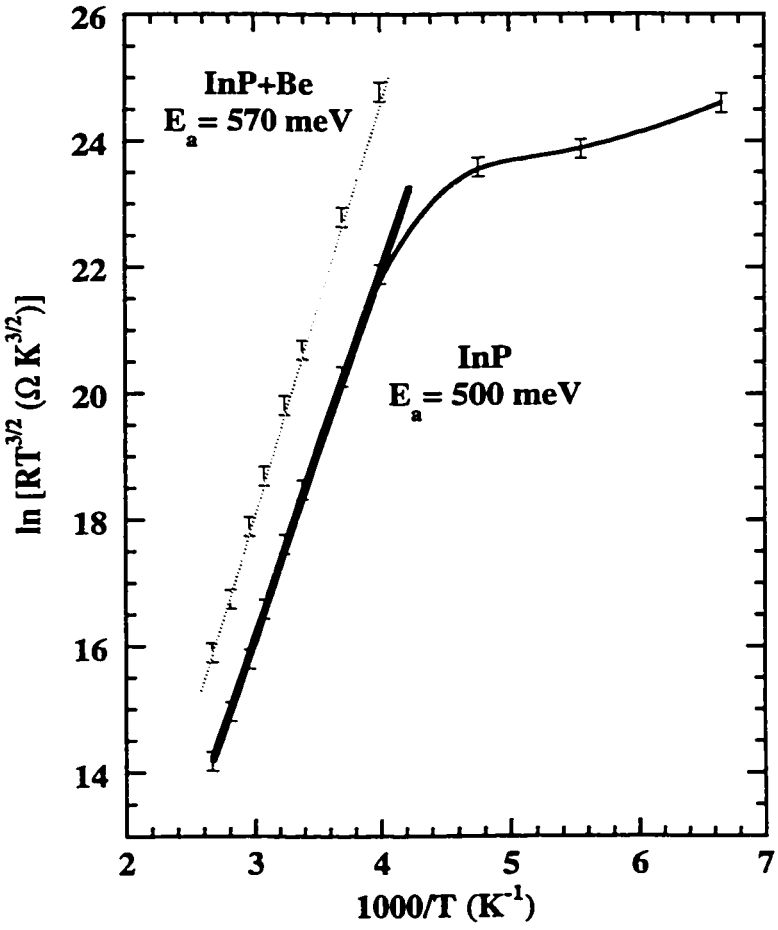

Figure 3.7: Temperature-dependent resistivity measurements for undoped and Be-doped He-InP

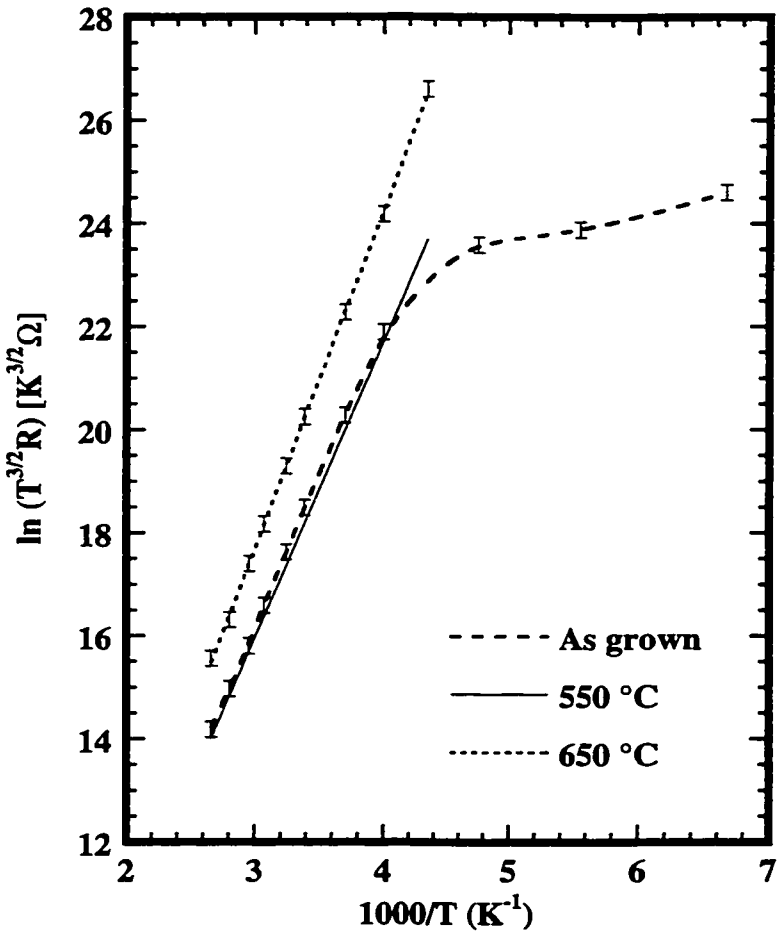

Figure 3.8: Temperature-dependent resistivity measurements for annealed undoped He-InP.

ping conduction between defect states. Given this interpretation, the activation energies for the He-plasma-assisted materials were calculated using the steeper slope and were found to be $(E_C - 500)$ meV for the undoped sample and $(E_C - 570)$ meV for the Be-doped sample, with an error in the linear fit of ± 5 meV. This confirms that the Fermi energy lies lower in the bandgap for the Be-doped sample, which is consistent with the increased resistivity described in Section 3.3. Since the bandgap of InP is 1.35 eV, these energy levels are just above mid-gap, hence both samples are

n-type. The room-temperature (T=295K) resistivities were calculated as $9x10^5$ Ω-cm for undoped He-InP and $2x10^6$ Ω-cm for Be-doped He-InP.

Figure 3.8 shows the temperature-dependent resistivity measurements for the annealed undoped He-InP samples. The results confirm the trend seen from the Hall effect measurements; the sample becomes more resistive with the 650°C anneal, which is consistent with the Fermi energy of the 650°C sample sitting lower in the bandgap. Once again, the hopping conduction mechanism appears for T(measurement)< 250K.

3.5 SIMS Results

The Hall effect studies showed that the Be in the doped sample was not electrically active, but was passivated or compensated in some way. Hydrogen is known to passivate acceptor-like dopants in the InP system in preference to donor-like dopants [W.C. Dautremont-Smith et al. (1989)] and is present in the chamber during growth. To investigate whether hydrogen may be playing a role in the high resistivity values of the Be-doped samples, a specially-designed sample, grown in the presence of deuterium, was submitted for SIMS analysis by Dr. Richard Streater at Nortel Networks Inc.

This sample, 2274, was comprised of 3000 Å layers of He-InP with various Be doping concentrations ($4x10^{17}$, $1x10^{18}$, $3x10^{18}$, $7x10^{18}$ cm^{-3}) sandwiched between 1000 Å thick undoped layers of He-InP, as illustrated in Figure 3.9. All layers were grown in the presence of the He-plasma and with deuterium gas present in the chamber, to give a total background pressure of $1x10^{-4}$ Torr (standard background of $\sim 4x10^{-5}$ Torr plus additional deuterium). The concentrations of D and Be for the sample before and after anneal for 10 seconds at 600°C are shown in Figure 3.10. The deuterium incorporated at a level of approximately $4x10^{17}$ cm^{-3} for the lower doping

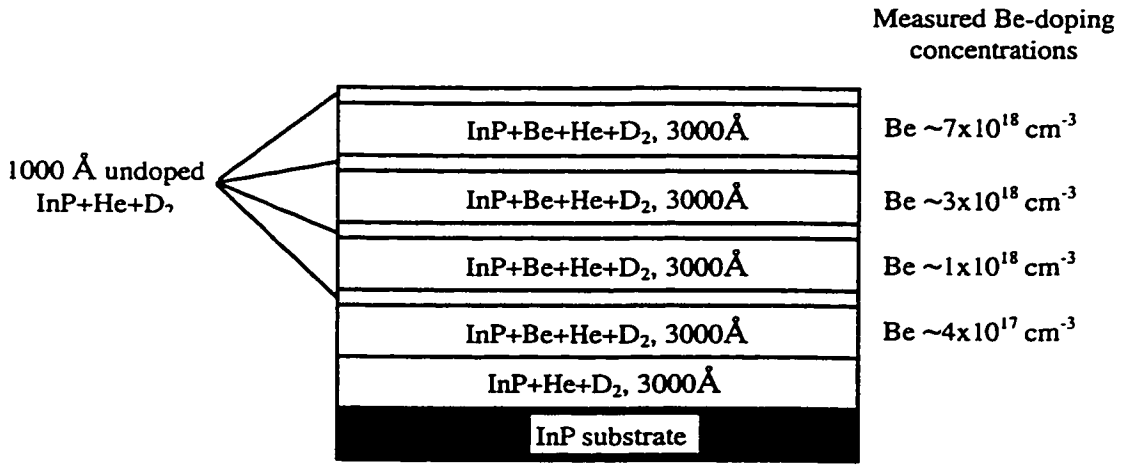

Figure 3.9: Structure of sample 2274, grown with deuterium for SIMS measurements.

levels of $4x10^{17}$ and $1x10^{18}$ cm^{-3} Be and this level increased slightly to $5x10^{17}$ cm^{-3} for the $3x10^{18}$ cm^{-3} doping level. The largest deuterium incorporation of $2x10^{18}$ cm^{-3} occurred for the highest Be doping of $7x10^{18}$ cm^{-3}. Also, the deuterium incorporation was approximately the same whether or not Be was present, with the undoped regions incorporating $5x10^{17}$ cm^{-3} deuterium. The results show that deuterium incorporates in the sample when the helium plasma is operating and, therefore, could be a factor in the resistivity properties of the samples. Also, there is enough deuterium present in the as-grown sample to fully passivate a weakly Be-doped ($3x10^{17}$ cm^{-3}) He-InP sample, such as that used for the Hall effect measurements. However, the weak relationship between Be concentration and deuterium incorporation suggests that the deuterium is not necessarily incorporated at Be sites. Therefore, Be passivation may not be the sole factor that determines the behaviour of the doped He-InP.

The SIMS results for the annealed sample also lead to this conclusion. After anneal for 10 seconds at 600°C, the deuterium has been reduced to a level of $1x10^{16}$

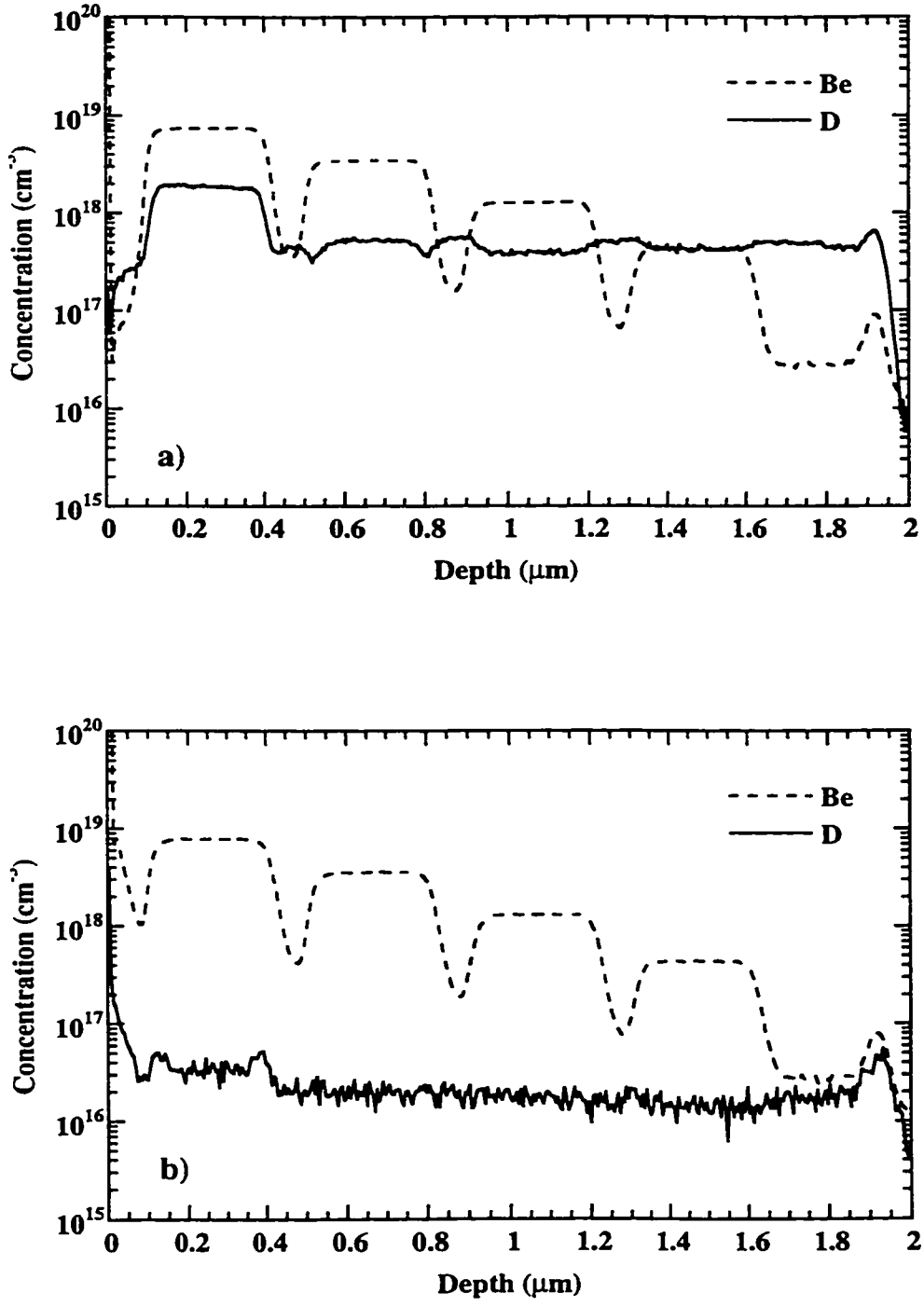

Figure 3.10: SIMS results for sample 2274, a) before and b) after anneal at 600°C.

to $3x10^{16}$ cm^{-3}, which is only a small fraction of the Be concentration. This implies that, if the Be is solely compensated by hydrogen or deuterium, then after anneal at 600°C, most of the Be should be electrically active. As seen from the Hall effect measurements, this is not the case, since the Be-doped samples retained their n-type nature on anneal.

3.6 Discussion

He-InP exhibits much higher resistivity than InP grown under standard conditions, due to reduced electron concentration and mobility. This implies the presence of an electron trap, i.e. an acceptor-like defect. The addition of $1x10^{18}$ cm^{-3} Be did not cause the material to be p-type, suggesting that the Be is either compensated by donor-like defects or is passivated in some way. The Be-doped sample became more resistive with anneal at 600°C, indicating that the Fermi energy moved lower in the bandgap. SIMS measurements indicated that, although the He-plasma causes deuterium to incorporate in the material, the concentration of deuterium did not depend strongly on the Be-doping concentration. Also, the deuterium content was reduced to $\sim 10^{16}$ cm^{-3} after anneal at 600°C. Therefore, hydrogen cannot be the sole cause of the Be "inactivity" since, after anneal, the concentration is too low. It seems then, that the Be must be compensated to a certain extent by a donor-like defect.

Samples of He-InP, both undoped and Be-doped ($1x10^{18}$ cm^{-3}) were sent to Dr. Jin Ung Kang at the Naval Research Laboratory in Washington, D.C., for sheet resistance and transient ellipsometric surface photoreflectance optical measurements [Pinkney et al. (1998), Kang et al. (1998)]. The sheet resistance measurements, plotted in Figure 3.11 confirmed the trends seen with the Hall effect and n-i-n studies (as described above). The undoped sample became more resistive with increased anneal

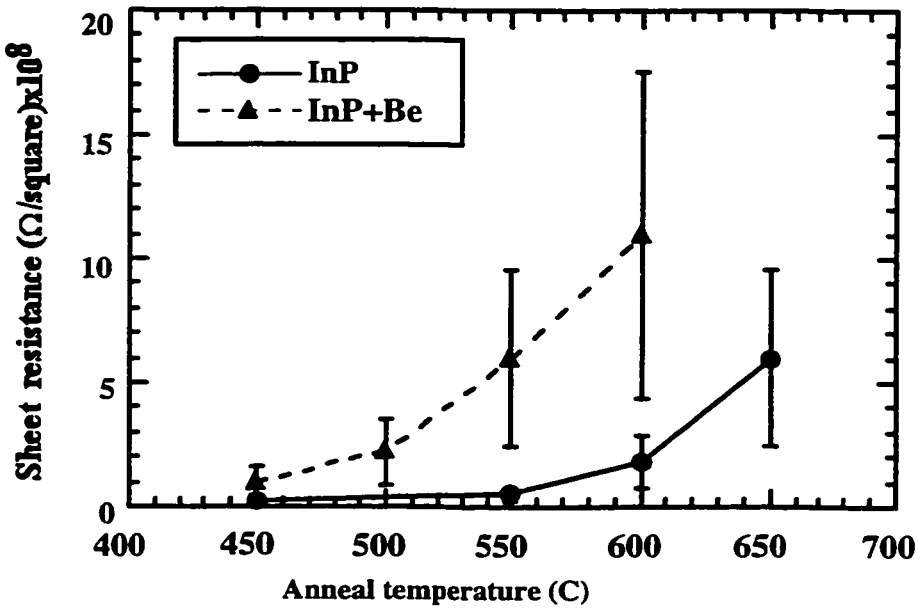

Figure 3.11: Sheet resistance as a function of anneal temperature for undoped and Be-doped He-InP (after Pinkney et al. (1998)).

temperature. The data for samples annealed above 600°C were omitted, because the resistivity was too high to give reliable measurements. The resistivity of the Be-doped sample, which was weakly n-type as-grown, also increased on anneal. However, beyond an anneal temperature of 650 °C, the sample may have become p-type, since the I-V characteristics indicated that a p-n junction may have been formed between the n-type contact and the sample. The Be-doped sample was also consistently more resistive than the undoped sample.

As mentioned in Section 1.3, He-InP emits very little photoluminescence, even when cooled to 15 K. However, it was possible to use the transient optical technique [Frankel and Carruthers (1994)] to determine the lifetime of the carriers in the material. The measurements indicated that the carrier lifetime in the as-grown Be-doped He-InP was 8 ps and in the undoped sample, 6 ps. However, after

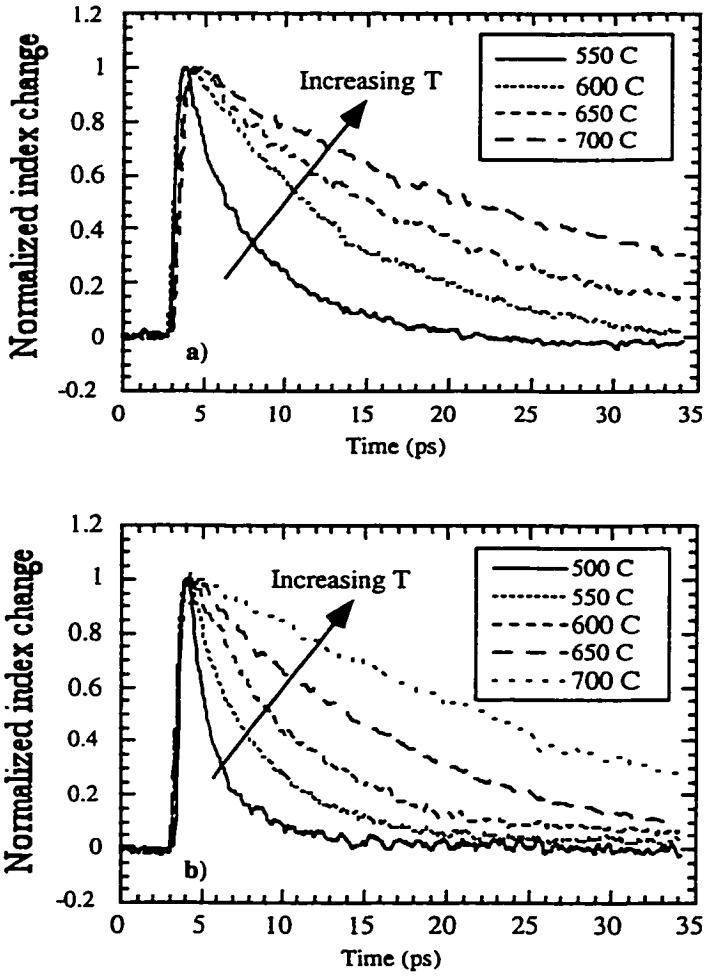

Figure 3.12: The effect of annealing on the carrier lifetime of a) He-InP and b) He-InP+Be, as measured by transient ellipsometric surface photoreflectance (after Pinkney et al. (1998)).

anneal at temperatures over the range 500 to 700 °C, the carrier lifetime in the Be-doped material was consistently shorter than that of the undoped He-InP, as shown in Figure 3.12. Also, the optical carrier lifetime increased as a function of anneal (to 24 ps and 13 ps for the undoped and Be-doped samples, respectively), suggesting that the defects responsible for the fast optical response were removed on annealing. The optical and electrical behaviours suggest that there are at least two defect types

present in the He-InP material: an electron trap that causes the undoped He-material to be more resistive than standard material, and a hole trap that is responsible for the high speed and Be compensation.

Positron annihilation spectroscopy on undoped and Be-doped He-InP revealed that divacancies were present, which enlarged on anneal. In the case of the Be-doped sample, the peak S-parameter decreased dramatically after anneal at 700°C, suggesting that the defects had become positively charged. This may indicate the presence of the P vacancy, a donor-like defect. Mitchell (1995) suggested the presence of two defects: the P vacancy and the P interstitial. Phosphorus is the lighter atom in the lattice; therefore, it is more likely to be dislodged in a collision event. The displaced atom would leave behind a donor-like vacancy and would itself become an interstitial, which is an electron trap. Therefore, both these defects may be playing a role in the behaviour of the material.

From this brief study of He-InP it was clear that identifying the defects responsible for the unusual characteristics would be difficult with the techniques available to us, due to the extreme electrical and optical properties. At this point, then, the focus of the study was turned to the quaternary material, InGaAsP. As we shall demonstrate in Chapters 4 and 5, the quaternary was much more accessible to electrical and optical characterization and was studied in some depth. Also, these studies allowed a model of the defect energy levels to be developed. The presence of four elements and the associated point defects (antisites, interstitials and vacancies) greatly increases the complexity of the system. However, from an applications viewpoint, the quaternary has much more potential for high-speed, all-optical devices.

Chapter 4

Experimental Results for InGaAsP

4.1 Introduction

In Chapter 3, we saw the difficulties in characterizing the He-plasma-assisted GSMBE binary material, InP, due to its very high resistivity. The quaternary material, $In_xGa_{1-x}As_{1-y}P_y$, offered an alternative system for study for two reasons: it is technologically important for the telecommunications industry; and it is easier to characterize electrically, due to its narrower bandgap. Also, as previously reported [Mitchell et al. (1996)], the quaternary material had already exhibited very short optical carrier lifetimes in undoped samples with a room-temperature wavelength of 1.5 μm. This chapter describes the results from positron annihilation spectroscopy, Hall effect, photoluminescence and SIMS measurements on InGaAsP, grown lattice-matched to InP, with a bandgap wavelength in the technologically important region of $\sim$ 1.55 μm.

4.2 Positron Results

Five quaternary samples were studied using the positron annihilation spectroscopy: undoped, with room-temperature bandgap wavelength of approximately 1.52 μm; Be-doped, 3x10^{17}cm^{-3}, bandgap wavelength of 1.52 μm; Be-doped, 3x10^{18}cm^{-3},

bandgap wavelength of 1.55 μm; Si-doped, 3x10^{17} cm^{-3}, bandgap wavelength 1.55 μm; and Si-doped, 3x10^{18} cm^{-3}, bandgap wavelength 1.55 μm. Standard samples, grown without the presence of the helium plasma, but under otherwise identical conditions, were also included in the study. All samples were grown at the normal growth rate of 1 μm/hour and were studied as-grown and after each of a number of 10 second rapid thermal annealing steps. The samples are summarized in Table 4.1.

4.2.1 Standard InGaAsP

Figure 4.1 shows how the S parameter changed with anneal for the undoped standard InGaAsP sample. The S parameter of the as-grown sample reached a value of approximately 0.502, as expected for a "defect-free" material, confirming that the standard growths were high-quality epitaxial samples. On anneal, the curve changed very little, indicating that no negatively-charged or neutral open volume defects were created by the anneal process. The controls for the doped samples, 2156 (Be) and 2454 (Si), behaved in a similar way and are not included here.

4.2.2 He-InGaAsP

Undoped He-InGaAsP

The positron annihilation results for the undoped He-InGaAsP sample, as-grown and after anneal, are shown in Figure 4.2. The presence of the He plasma during growth caused the maximum S parameter to increase to a value of 0.52, i.e. $S_{Epi}/S_{Substrate}$=1.03. This implies that open volume neutral or negatively-charged defects were created by the impact of the plasma particles during growth, most likely in the form of single and divacancies [Saarinen et al. (1998)]. On anneal, the S parameter peak increased steadily until a temperature of 650°C was reached, at which point the S parameter saturated at approximately 0.54. This gives a normalized S

MBE no.	Description	Dopant (cm^{-3})	Anneal temperatures (°C)
2154	InGaAsP + He	None	500, 550, 600, 650, 700
2155	InGaAsP (no plasma)	None	500, 550, 600, 650, 700
2157	InGaAsP + He	Be, $3x10^{17}$	500, 515, 600, 650, 700
2725	InGaAsP +He	Be, $3x10^{18}$	550, 650, 700
2156	InGaAsP (no plasma)	Be, $3x10^{17}$	500, 515, 600, 650, 700
2454	InGaAsP + He	Si, $3x10^{17}$	550, 600, 650, 700
2723	InGaAsP + He	Si, $3x10^{18}$	550, 650, 700
2459	InGaAsP (no plasma)	Si, $3x10^{18}$	550, 600, 650, 700

Table 4.1: Summary of InGaAsP samples and anneal temperatures

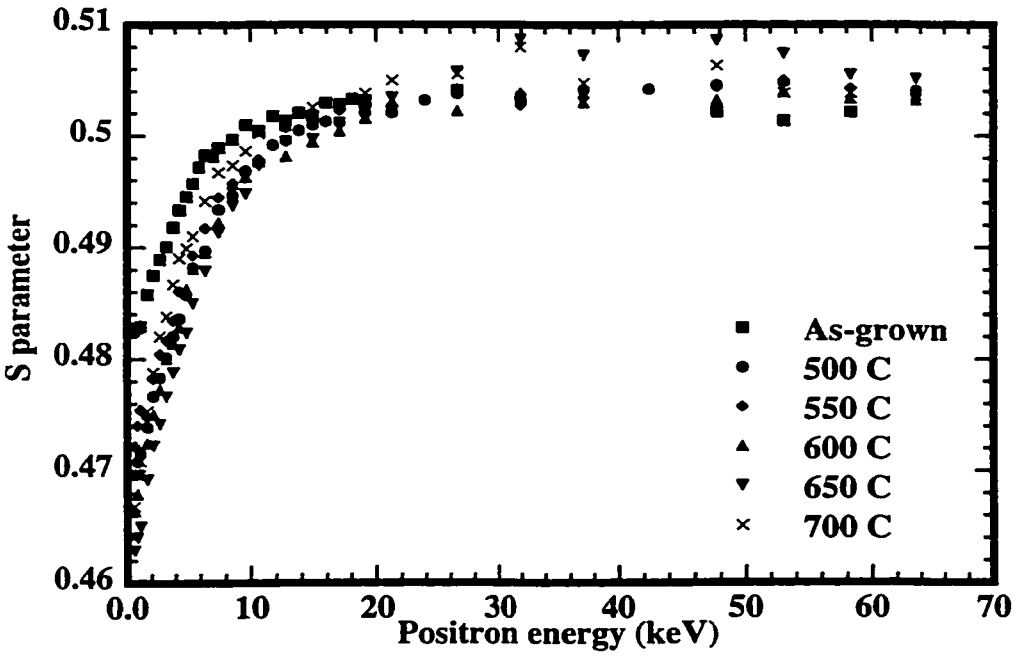

Figure 4.1: Positron annihilation results for undoped InGaAsP standard, as-grown and after all anneals.

value of $S_{Epi}/S_{Substrate}$=1.06, which indicates open volume clusters larger than 2 or 3 vacancies in size [Saarinen et al. (1998)]. As explained in Section 2.2, the S parameter tends to scale with the size of the open volume defect, so this increase in $S_{Epi}/S_{Substrate}$ may be explained by the single vacancies diffusing during annealing and agglomerating to produce larger vacancy clusters.

Si-Doped He-InGaAsP

Two Si-doped samples with different dopant concentrations ($3x10^{17}$ and $3x10^{18}$ cm^{-3}) were studied using this technique. Figures 4.3 and 4.4 show the results for the samples doped with $3x10^{17}$ and $3x10^{18}$ cm^{-3}, respectively. Both Si-doped He-InGaAsP samples were very similar to the undoped sample. The S parameter of the as-grown samples was approximately 0.52, $S_{Epi}/S_{Substrate}$=1.025 (single and di-vacancies), and this value rose to and saturated at ~0.54, $S_{Epi}/S_{Substrate}$=1.06 (open volume defects > 2 or 3 vacancies), after anneal at 650°C. Annealing at 700°C did not change the peak S-parameter appreciably for either sample. These results indicate that the presence of Si at a concentration of either $3x10^{17}$ or $3x10^{18}$ cm^{-3} affects neither how the defects are created by the plasma, nor how they behave on anneal. As for the undoped sample, the He-plasma causes single and divacancies, which diffuse and agglomerate with anneal.

Be-Doped He-InGaAsP

The positron annihilation results for the Be-doped samples are shown in Figures 4.5 and 4.6 for the samples doped with $3x10^{17}$ and $3x10^{18}$ cm^{-3} Be, respectively. The sample doped with $3x10^{17}$ cm^{-3} Be initially exhibited similar behaviour to the undoped and Si-doped He-InGaAsP samples. The as-grown S parameter had a value of 0.52, ($S_{Epi}/S_{Substrate}$=1.03, indicating single and divacancies), but the S value only

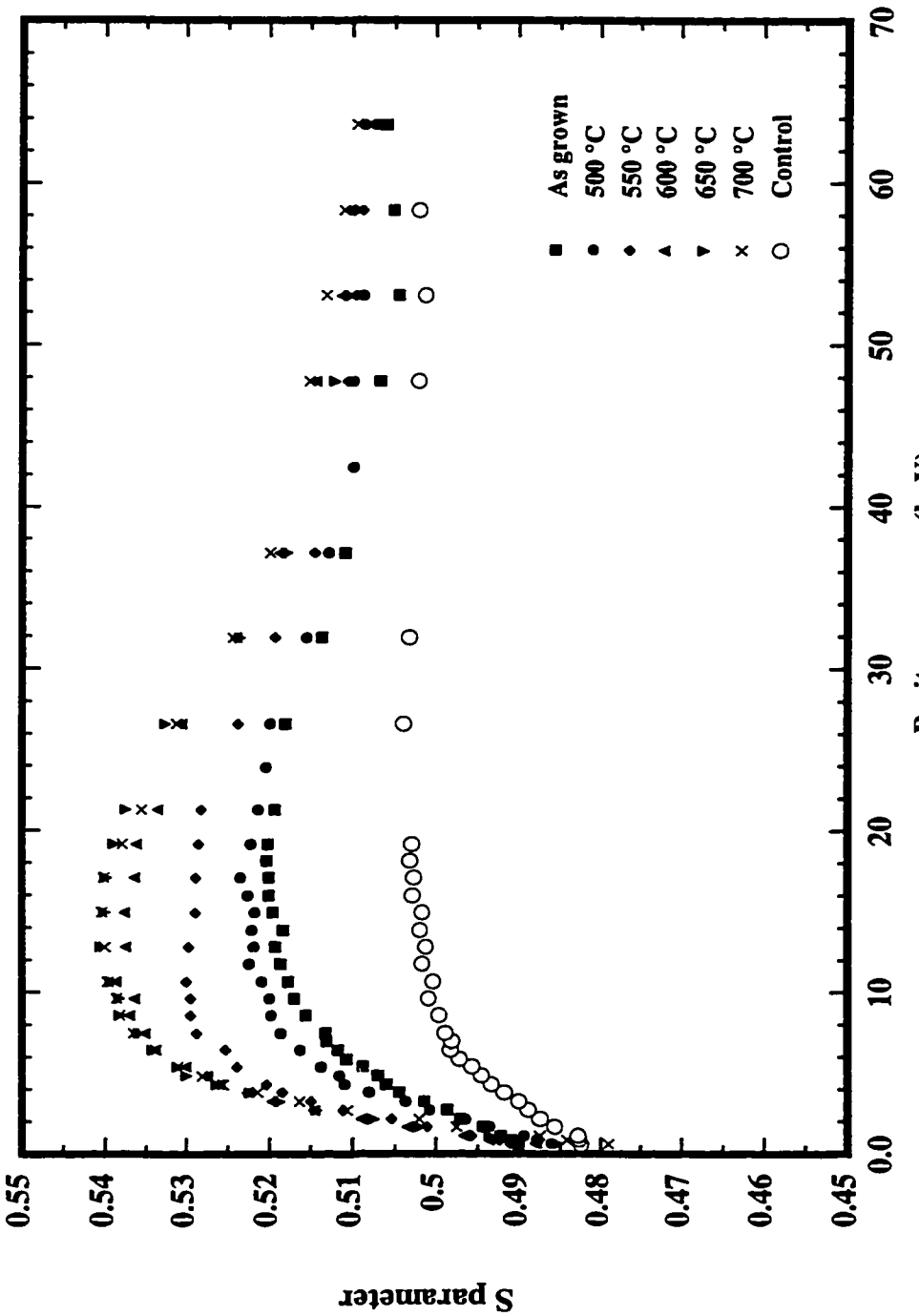

Figure 4.2: Positron annihilation results for undoped He-InGaAsP, as-grown and after all anneals.

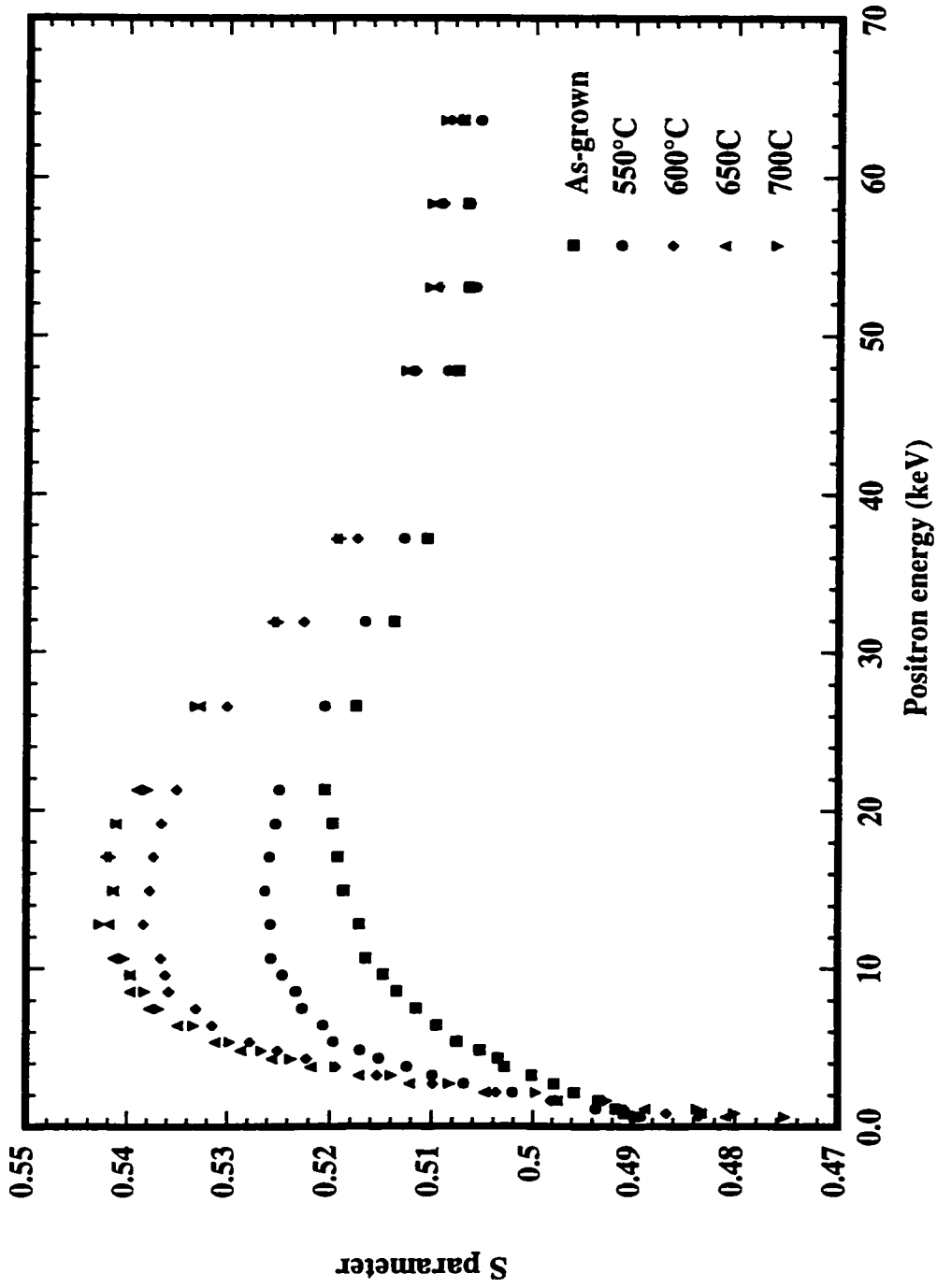

Figure 4.3: Positron annihilation results for He-InGaAsP doped with $3x10^{17}$ cm^{-3} Si, as-grown and after all anneals.

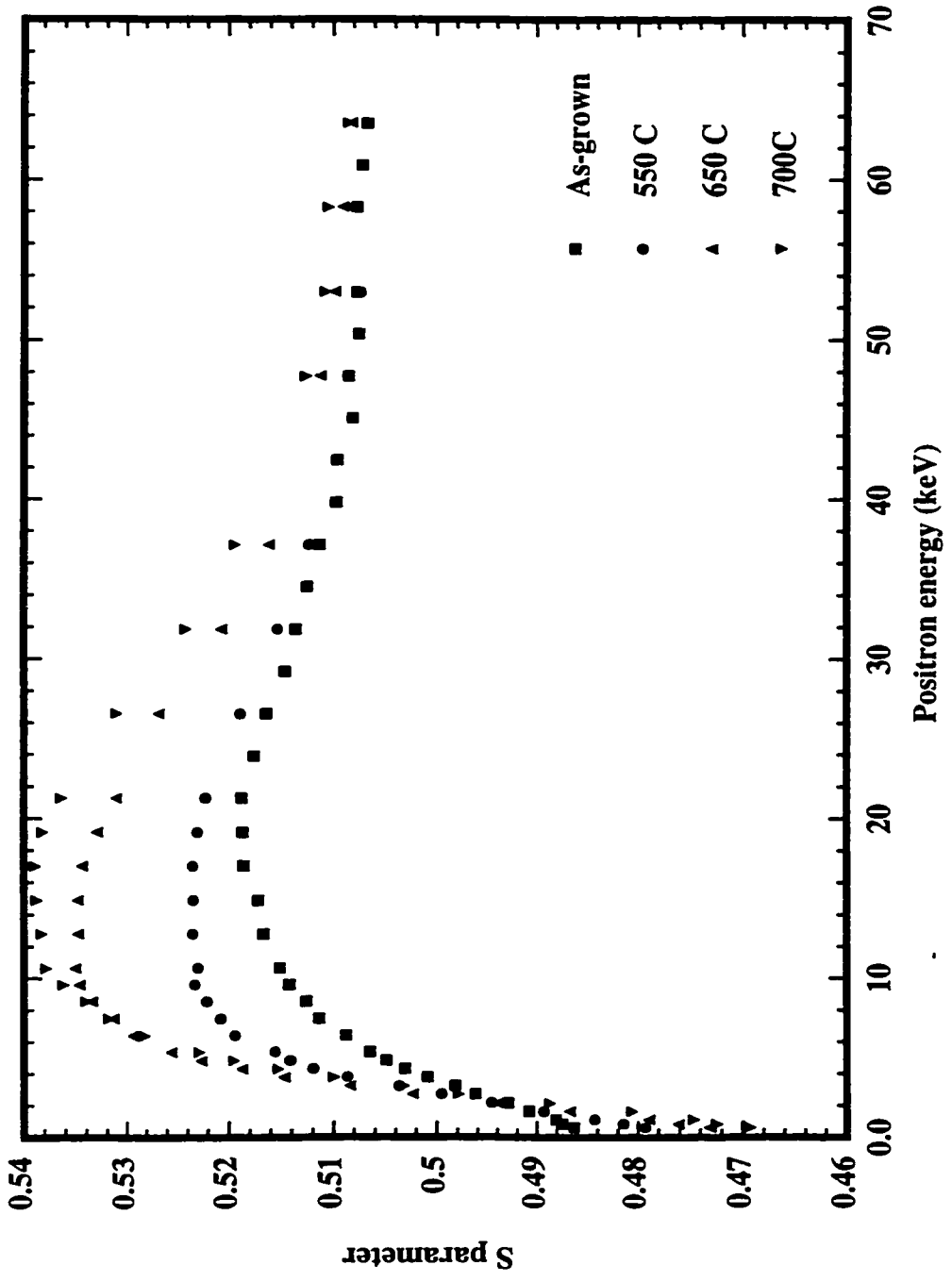

Figure 4.4: Positron annihilation results for He-InGaAsP doped with $3x10^{18}$ cm^{-3} Si, as-grown and after all anneals.

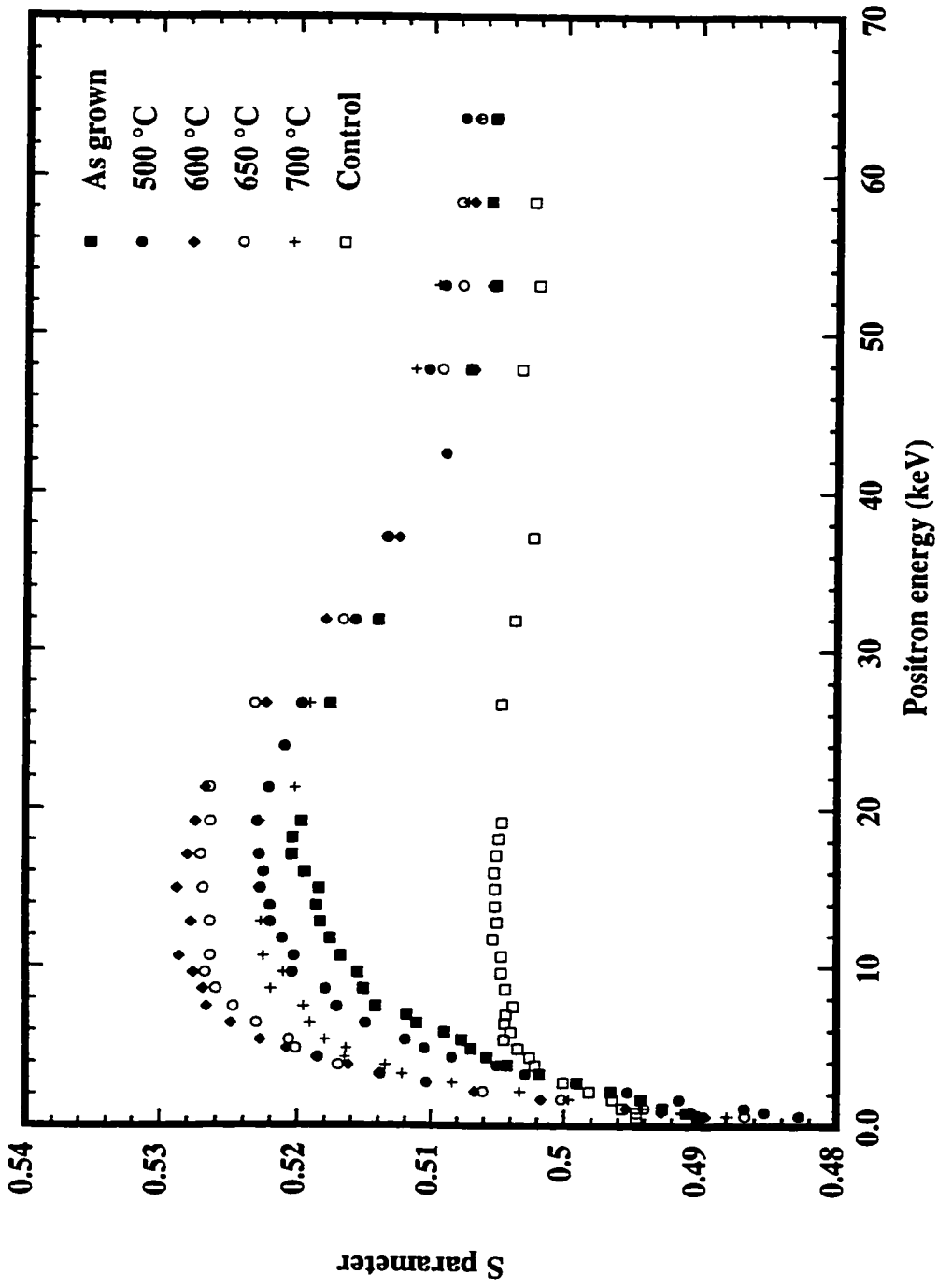

Figure 4.5: Positron annihilation results for He-InGaAsP doped with $3x10^{17}$ cm^{-3} Be, as-grown and after all anneals.

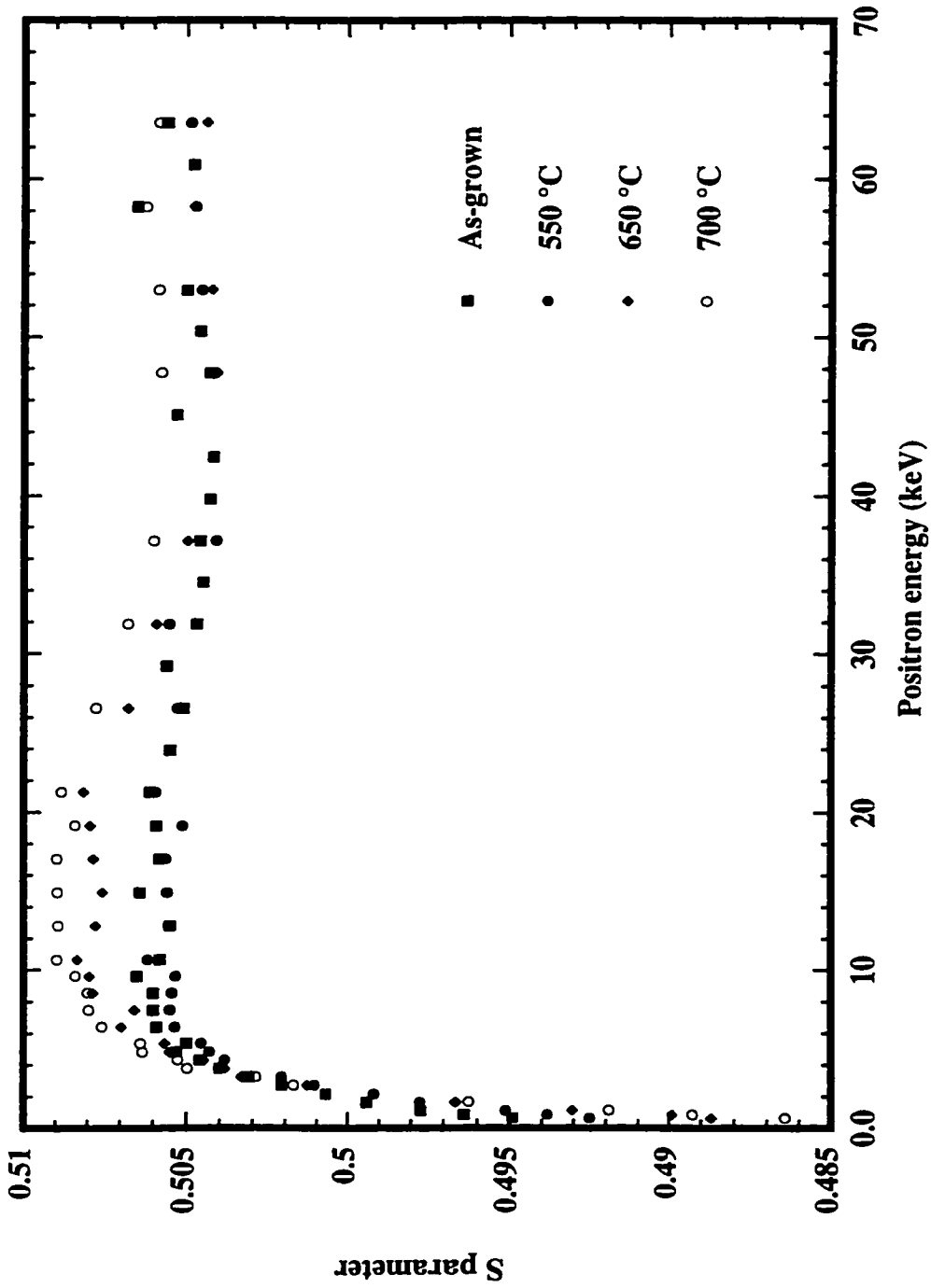

Figure 4.6: Positron annihilation results for He-InGaAsP doped with $3x10^{18}$ cm^{-3} Be, as-grown and after all anneals.

increased to 0.528, ($S_{Epi}/S_{Substrate}$=1.045) at an anneal of 600°C. At anneal temperatures beyond this, the S parameter decreased to 0.526 ($S_{Epi}/S_{Substrate}$=1.037) at 650°C and 0.523 ($S_{Epi}/S_{Substrate}$=1.032) at 700°C. As for the Be-doped He-InP sample, this reduction in the S-parameter could be due to two things: either the Be has caused the defect clusters to break up at the higher anneal temperatures or the defects have become positively charged. Since the Be-doped sample followed the same trends as the undoped and Si-doped samples at the lower anneal temperatures, it seems more likely that the Be has caused the Fermi energy to move lower in the gap, thereby changing the charge state of the defects to positive.

It was possible that the behaviour of the Be-doped sample was related to the anneal temperature, rather than the position of the Fermi energy in the bandgap. To further investigate this, a highly Be-doped sample, known to be p-type as grown, was studied. This sample behaved very differently from all the previous He-InGaAsP samples. As can be seen from Figure 4.6, there is no peak in the S-parameter versus positron energy plot. The S-parameter for the as-grown sample was no different from the standard Be-doped sample (grown without plasma), with a value of approximately 0.506, ($S_{Epi}/S_{Substrate}$=1.002). On anneal, this value changed very little, reaching 0.509, or $S_{Epi}/S_{Substrate}$=1.006, after anneal at 700°C. According to accepted values of the normalized S-parameter, this would indicate that there are few neutral or negatively-charged defects present in the sample. There is no reason to believe that the increased concentration of Be prevented the formation of any defects; the electrical measurements described in the following section prove otherwise. It seems that for a p-type sample in which the Fermi energy sits in the lower half of the bandgap, the open volume defects become positively charged and undetectable by the positron beam.

4.2.3 Low Growth Rate He-InGaAsP

Since the defects are caused by the impact of the plasma particles during growth, a change in the growth rate should cause changes to the defects. To study this effect, an undoped He-InGaAsP sample (MBE no. 2584, $\lambda = 1.55\mu$m) was grown at one third the standard growth rate, 0.3 μm/hour, while the plasma conditions remained unchanged. Unlike the standard growth-rate He-plasma samples,this sample appeared milky white, suggesting serious damage to the surface. Figure 4.7 compares the positron annihilation results for the low growth-rate sample with a He-InGaAsP standard growth rate sample and a control. The effect of the reduced growth rate was to increase the S parameter from 0.52 ($S_{Epi}/S_{Substrate}$=1.025- 1.03) for all the standard growth-rate He-InGaAsP samples to 0.53 ($S_{Epi}/S_{Substrate}$=1.045), presumably due to an increase in the average size of the open volume defects. Figure 4.8 illustrates the effect of annealing this sample. As one would expect, the S parameter increases and saturates at approximately 0.54 ($S_{Epi}/S_{Substrate}$=1.07) after an anneal at 650°C. Annealing at 700°C did not increase the S parameter further.

4.3 Room-Temperature Hall Effect Measurements

A number of doped and undoped samples were grown to study the effects of Be- and Si-doping on the electrical characteristics. All samples were 2 μm thick grown on a semi-insulating InP substrate. The room-temperature bandgap wavelength was 1.55 μm for all samples, except 2155 the standard undoped quaternary, which had a bandgap wavelength of 1.52 μm. Hall effect measurements were performed on the samples as-grown and after a 10 second rapid thermal anneal at a given temperature, summarized in Table 4.2.

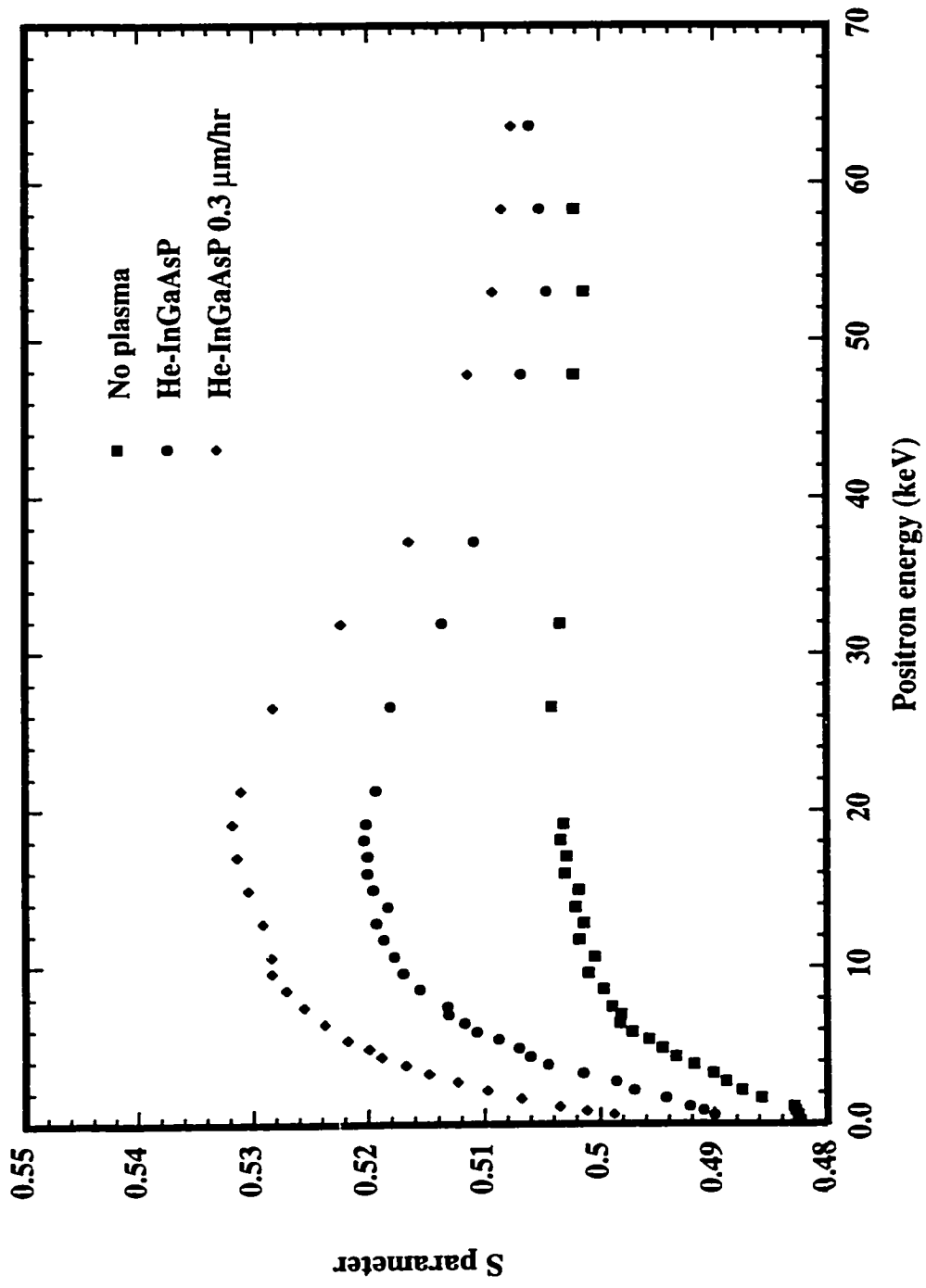

Figure 4.7: Comparison of positron annihilation results for control InGaAsP, standard growth-rate He-InGaAsP and low growth-rate He-InGaAsP.

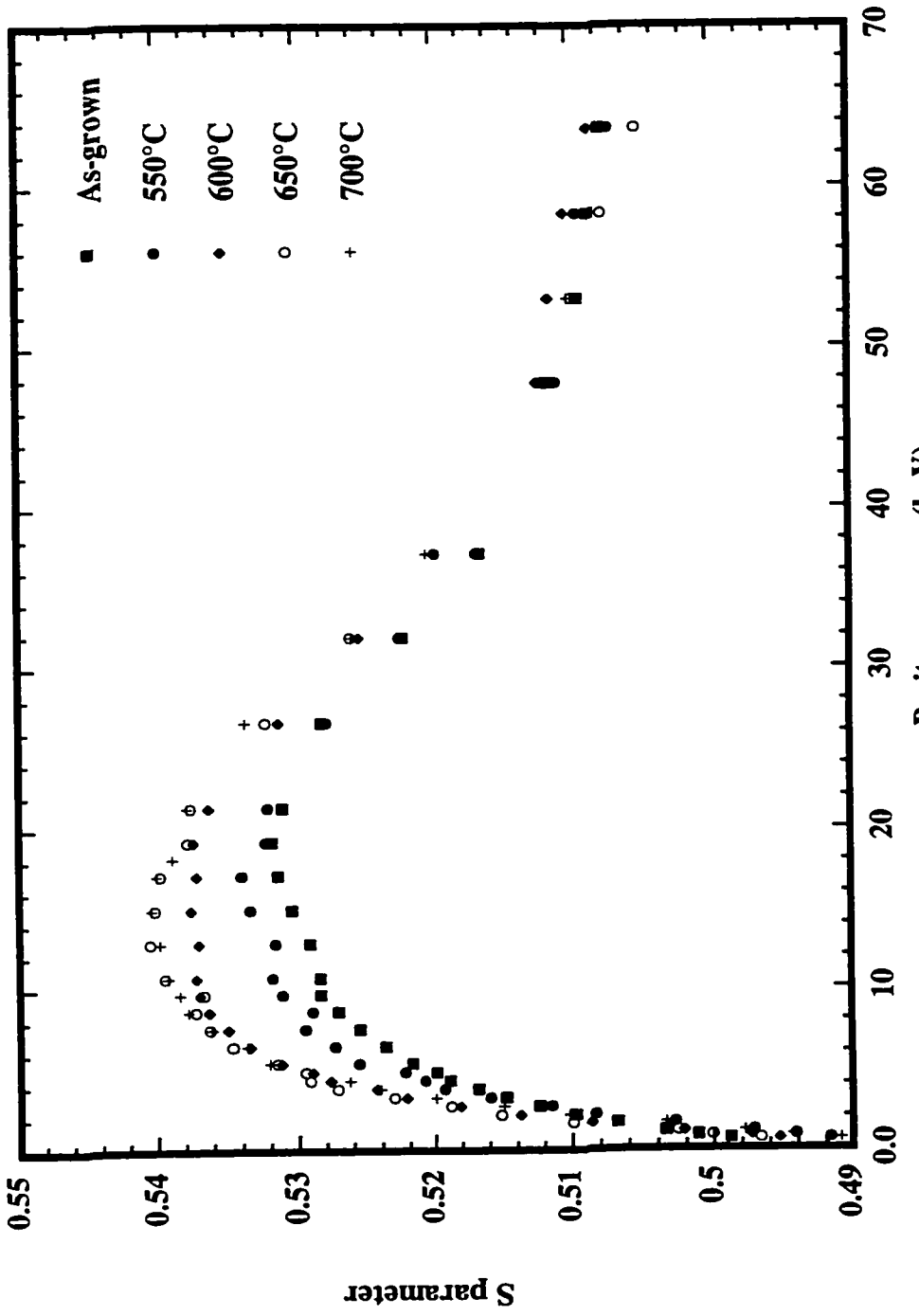

Figure 4.8: Positron annihilation results for low growth rate He-InGaAsP, as-grown and after all anneals.

MBE No.	Dopant Conc. (cm^{-3})	Comments
2155	None	Standard: no plasma
2582	None	He-plasma
2459	Si $3x10^{17}$	He-plasma
2458	Si $7x10^{17}$	He-plasma
2529	Si $1x10^{18}$	He-plasma
2528	Si $3x10^{18}$	He-plasma
2457	Si $4x10^{18}$	He-plasma
2454	Si $3x10^{18}$	Standard: no plasma
2578	Be $1x10^{17}$	He-plasma
2579	Be $3x10^{17}$	He-plasma
2465	Be $1x10^{18}$	He-plasma
2464	Be $2x10^{18}$	He-plasma
2463	Be $3x10^{18}$	He-plasma
2580	Be $4x10^{18}$	He-plasma
2581	Be $5x10^{18}$	He-plasma
2461	Be $6x10^{18}$	He-plasma
2460	Be $6x10^{18}$	Standard: no plasma

Table 4.2: Summary of samples for Hall effect measurements

4.3.1 Undoped He-InGaAsP

Figure 4.9 shows the carrier concentration and mobility as a function of anneal temperature for the nominally undoped He-InGaAsP sample. The as-grown sample, represented at T_{anneal} = 450°C, the growth temperature, was weakly n-type with a carrier concentration of approximately 10^{14} cm^{-3} and an electron mobility of 2350 cm^2/Vs. The carrier concentration and mobility for the standard undoped quaternary sample were $3x10^{15}$ cm^{-3} and approximately 6400 cm^2/Vs, respectively, and these values did not change substantially on anneal. The reduced free carrier concentration implies that electron traps were created by the He-plasma during growth, while the reduced mobility suggests that ionized defects may be present. The free carrier concentration decreased with anneal, reaching a minimum of $4.5x10^{12}$ cm^{-3} after anneal at 600°C. As discussed in Section 3.3, the helium-plasma-assisted growth

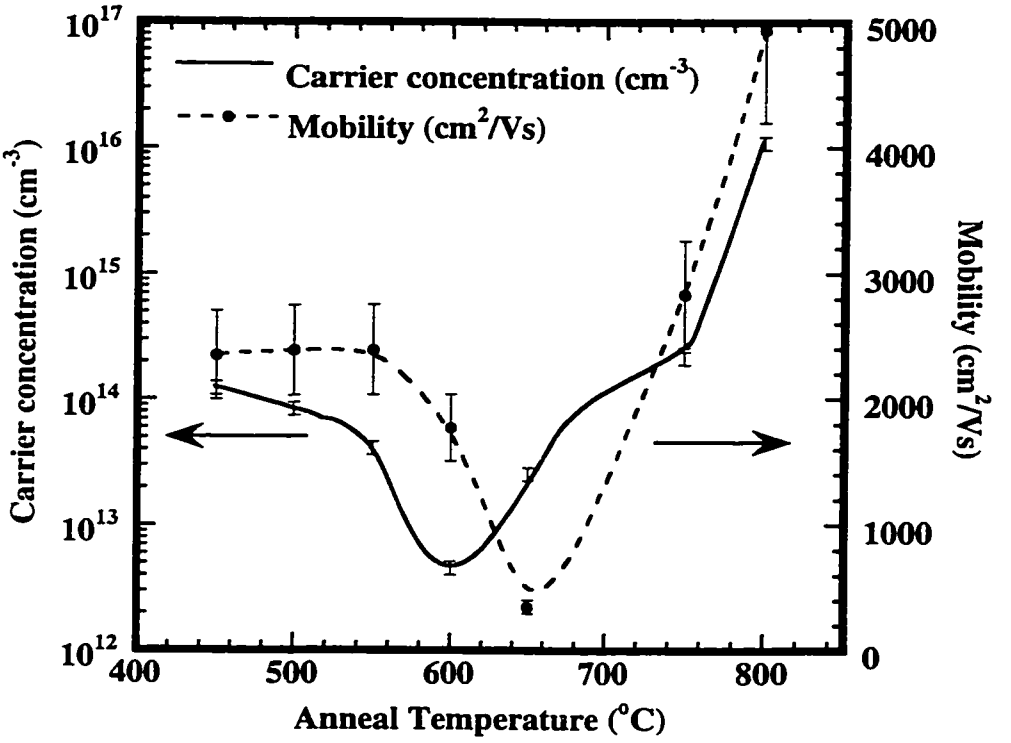

Figure 4.9: The carrier concentration and mobility as a function of anneal temperature for undoped He-InGaAsP.

technique introduces deep donor-like defects into InP. The reduction in the electron concentration in the quaternary may be due to the removal of similar donor-like defects. Beyond 600°C, the carrier concentration increased, suggesting the removal of electron traps from the system. The carrier concentration after anneal at 800°C is higher than that of the standard sample, which suggests that a donor-like impurity is present. Since a small concentration of Si ($\sim 4 \times 10^{16}$ cm^{-3}) was found in the undoped layer of the He-InP n-i-n samples, it is possible that unintentional doping has occurred during growth of the quaternary samples also.

The electron mobility decreased on anneal to a value of 350 cm^2/Vs after

650°C. This corresponds to the increase in S-parameter with anneal found from the positron annihilation spectroscopy and may indicate that the larger open volume defects formed during anneal arc better scattering centres. The increase in mobility for anneal temperatures >650°C coincides with the increase in free carrier concentration, hence may be due to the removal of the electron traps from the system. It seems clear from the electrical behaviour that more than one type of defect is present in He-InGaAsP.

4.3.2 Si-doped He-InGaAsP

Room-temperature Hall effect measurements were performed on He-InGaAsP samples doped with Si concentrations of $3x10^{17}$ to $3.5x10^{18}$ cm^{-3}. A control standard sample, doped with $3x10^{18}$ cm^{-3} Si, exhibited a carrier concentration of $(3.1\pm0.1)x10^{18}$ cm^{-3} as-grown and after all anneals, indicating that any changes in the carrier concentration were not due to the anneal process itself. Figure 4.10 shows the carrier concentration for the as-grown He-plasma-assisted samples compared to the expected (doping) concentration. All samples were n-type, as expected for this dopant, but the carrier concentration was much lower than the doping concentration, indicating the presence of electron traps, as seen in the undoped He-InGaAsP sample. The as-grown carrier concentrations were $2.6x10^{15}$ and $2x10^{18}$ cm^{-3} for the samples doped with $3x10^{17}$ and $3x10^{18}$ cm^{-3} Si respectively.

Figure 4.11 shows the carrier concentration as a function of anneal temperature for all Si-doped samples. The carrier concentration for all samples increased steadily with anneal, which is consistent with the removal of electron traps. The decrease in free carrier concentration with anneal seen for the undoped sample was not observed for any of the Si-doped samples, because the Si-doped samples exhibited much larger free carrier concentrations. At 550°C, there was very little change in

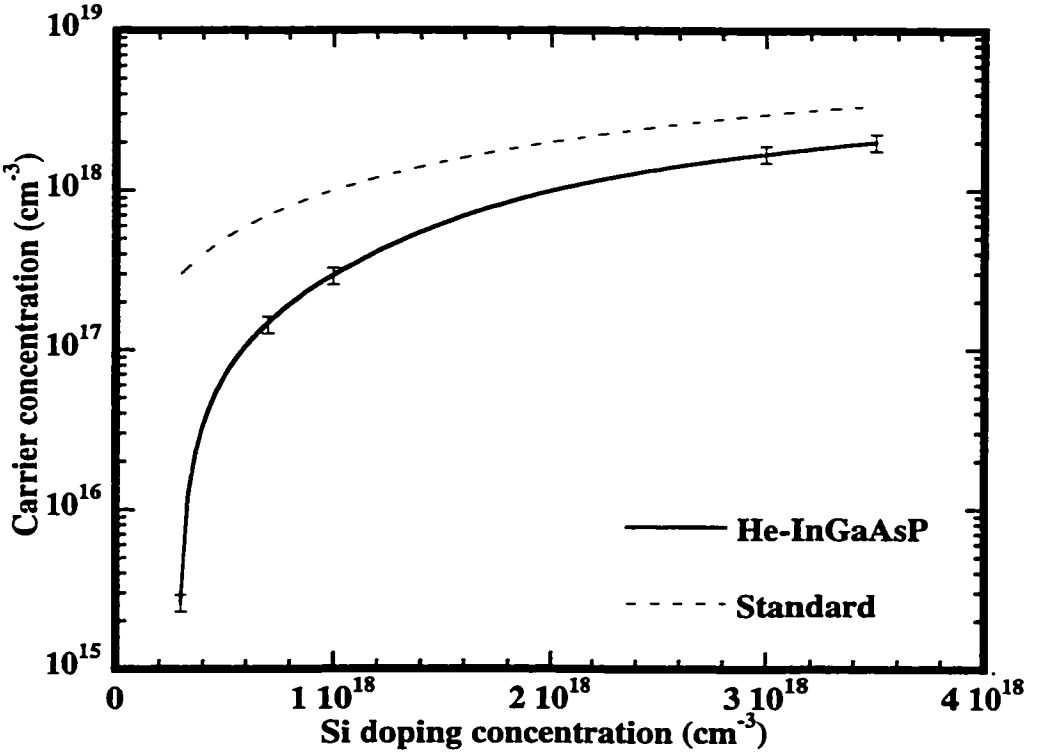

Figure 4.10: Carrier concentration as a function of doping for Si-doped He-InGaAsP compared to expected values for standard InGaAsP.

the electrical behaviour, suggesting that a substantial number of the electron traps responsible for the low carrier concentration were not removed at this anneal temperature. The first substantial change in the carrier concentration occurred after anneal at 650°C. After anneal at 800°C, the carrier concentration for all samples approached the doping concentration ($2.2\text{x}10^{17}$ cm^{-3} and $3.3\text{x}10^{18}$ cm^{-3} for samples doped with $3\text{x}10^{17}$ and $3\text{x}10^{18}$ cm^{-3} Si, respectively), indicating that most of the electron traps had been removed.

A summary of mobility versus Si-doping concentration after annealing is shown in Figure 4.12. All the as-grown He-plasma samples exhibited mobilities in the

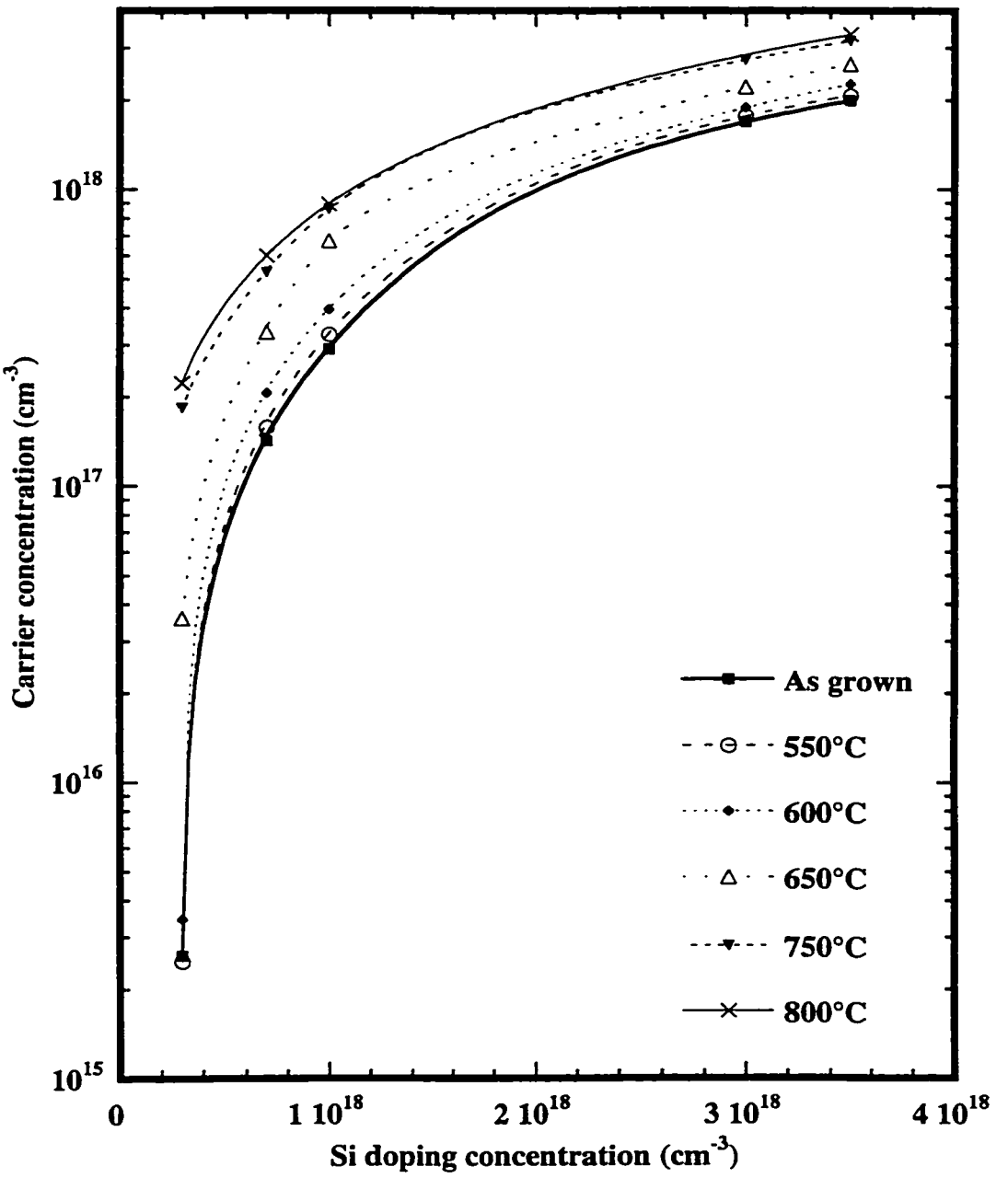

Figure 4.11: Effect of annealing on carrier concentration in Si-doped He-InGaAsP.

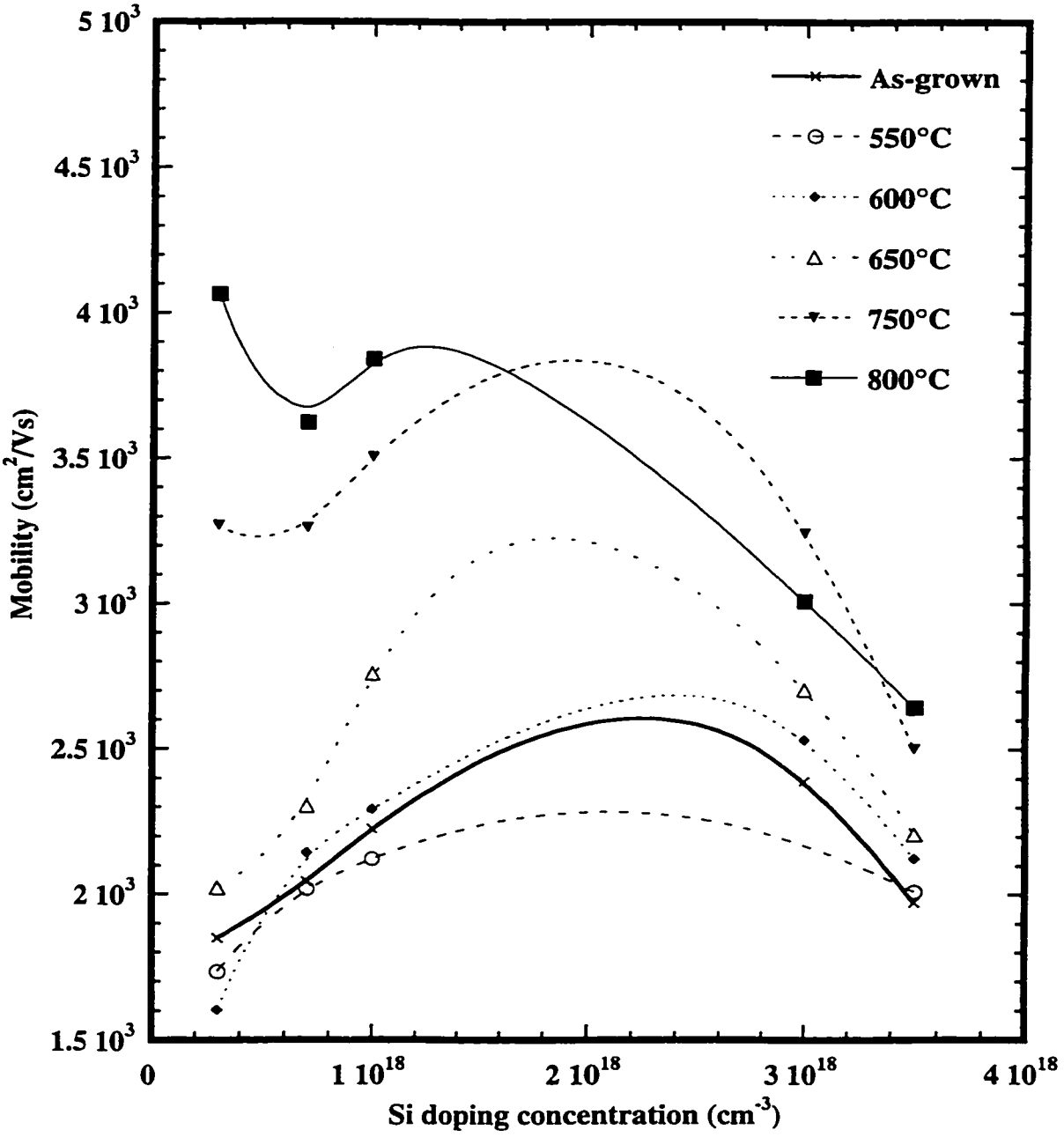

Figure 4.12: Effect of annealing on carrier mobility in Si-doped He-InGaAsP.

range 1850 to 2400 cm^2/Vs. This value is low compared with 2990 cm^2/Vs for the as-grown standard sample ($3x10^{18}$ cm^{-3} Si), suggesting that the defects have reduced the mobility of the samples. Also the curves exhibit a maximum: for Si concentrations of $3x10^{17}$ to $\sim 2x10^{18}$ cm^{-3} the mobility increased; beyond this concentration, the mobility showed a steady decrease. For standard, high quality samples, a steady decrease in mobility would be expected as the concentration of ionized donors increased. Thus, it seems that the mobility of the samples at the lower Si concentrations is controlled by defects. On anneal at 550°C, the mobilities of all samples barely changed. However, for anneal temperatures >600°C, the mobility steadily increased. Finally, after anneal at 800°C, the mobility of the sample doped with $3x10^{18}$ cm^{-3} was 3010 cm^2/Vs, which is comparable to 3070 cm^2/Vs for the annealed control ($3x10^{18}$ cm^{-3} Si), indicating that the majority of scattering centres had been removed.

4.3.3 Be-doped He-InGaAsP

Be-doped samples were grown with doping in the range of $1x10^{17}$ to $6x10^{18}$ cm^{-3}. The carrier concentration as a function of doping is plotted for the as-grown samples in Figure 4.13. At doping levels $<2x10^{18}$ cm^{-3}, all the He-InGaAsP samples were weakly n-type, despite the (p-type) Be doping. This implies that the Be is either passivated (by hydrogen, for example) or is compensated by a donor-like defect. As will be seen in Section 4.6, SIMS analysis indicates that there is insufficient hydrogen present in the as-grown samples for significant passivation to be the cause of this reduced electrical activity. Therefore, it seems likely that the Be is compensated by donor-like defects, as seen for He-InP in Section 3.3. The weakly Be-doped samples (n-type, $<2x10^{18}$ cm^{-3}) exhibited reduced electron concentration with increased Be-doping, implying that a fraction of the Be must be electrically active, to pull the Fermi energy lower in the bandgap. Beyond a Be doping level of $2x10^{18}$ cm^{-3}, the

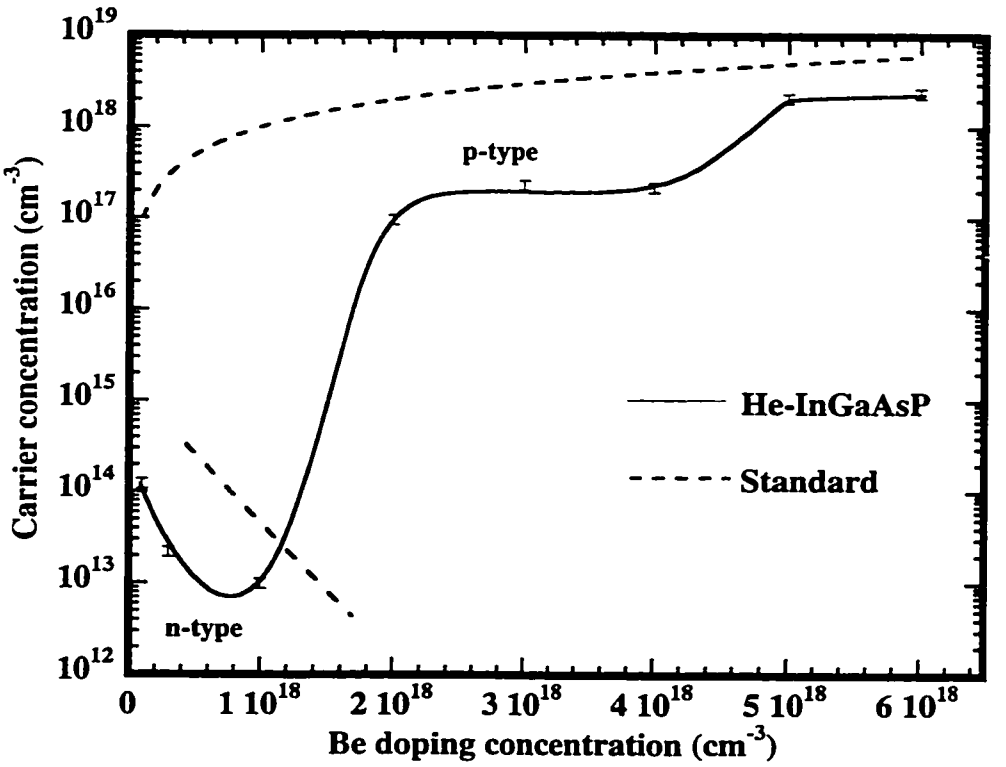

Figure 4.13: Carrier concentration as a function of doping for Be-doped He-InGaAsP samples

samples were p-type, as expected, although the hole concentration was much lower than for standard (no plasma) growths. Once again, this behaviour is probably due to Be compensation by native defects.

The effect of annealing on the carrier concentration is illustrated in Figure 4.14. After anneal at 500°C and 550°C, the samples with Be doping of $1x10^{17}$ and $3x10^{17}$ cm^{-3} remained n-type, with slightly reduced carrier concentrations. However, the sample doped with $1x10^{18}$ cm^{-3} Be converted to p-type after anneal at 500°C. After anneal at 650°C, all samples that were initially n-type (i.e. Be $<2x10^{18}$ cm^{-3}) had converted to p-type. The initial decrease in electron concentration (and consequently in Fermi energy) with anneal for the weakly-doped samples is similar to the

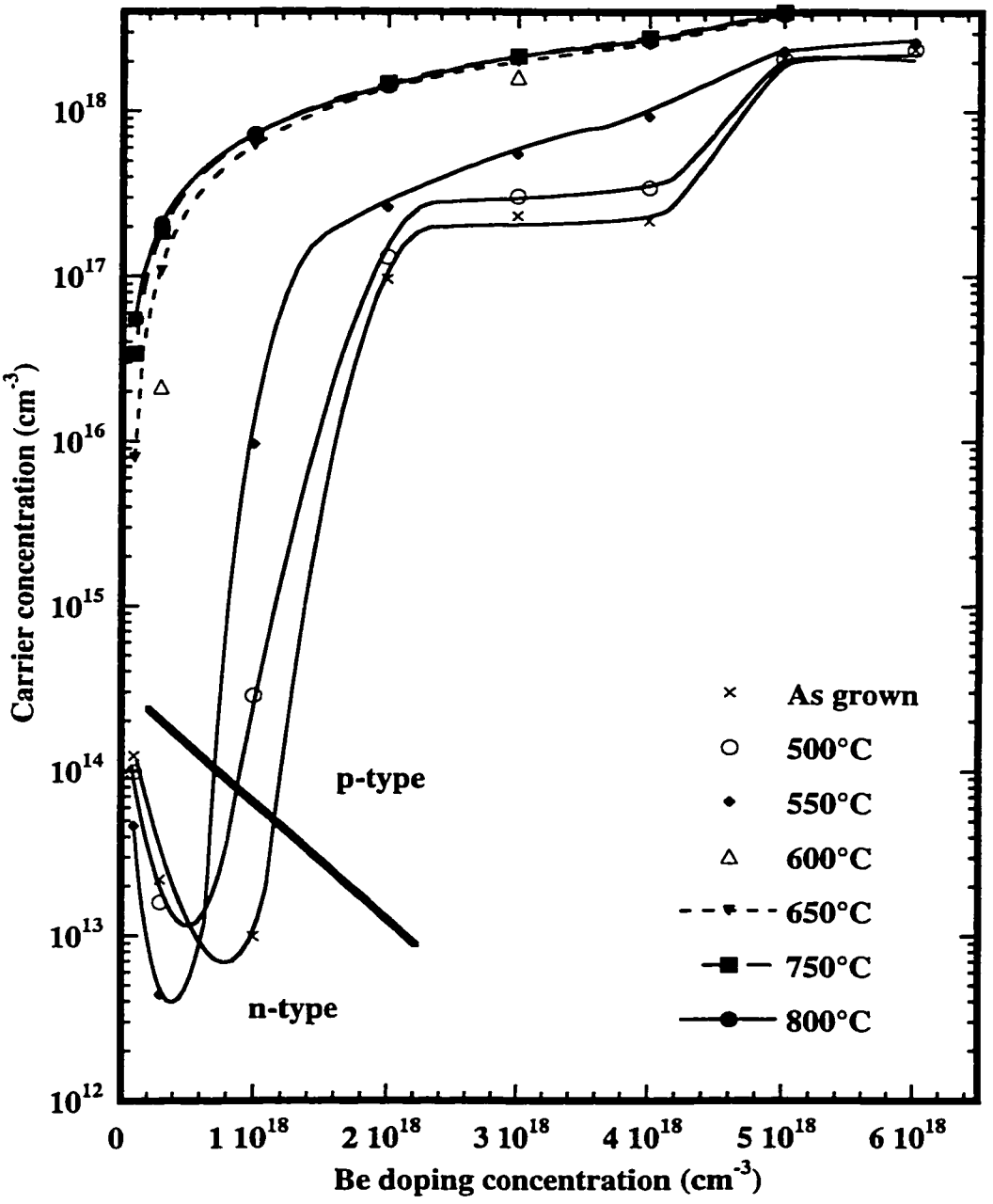

Figure 4.14: Effect of annealing on carrier concentration in Be-doped He-InGaAsP.

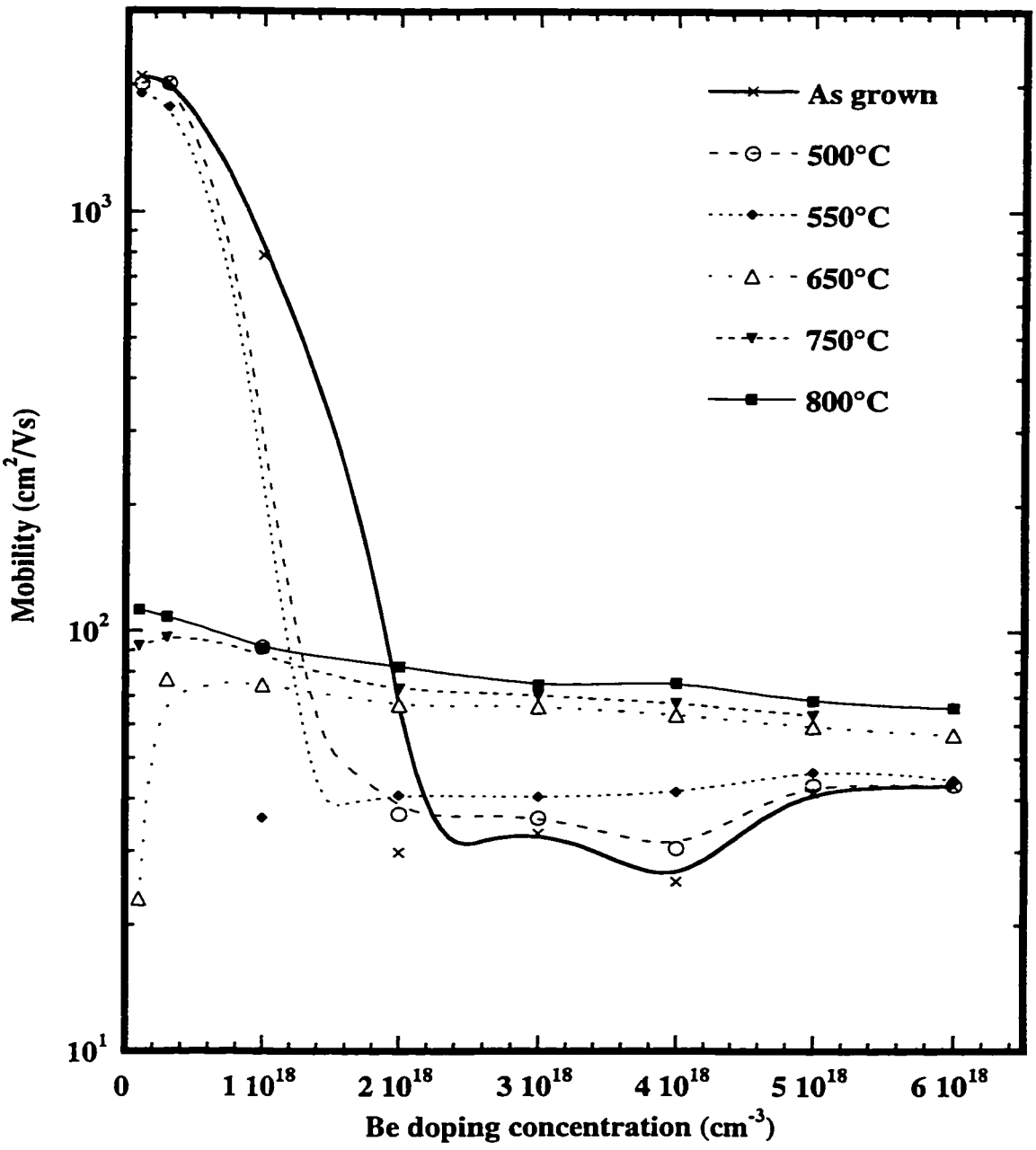

Figure 4.15: Effect of annealing on carrier mobility in Be-doped He-InGaAsP.

behaviour exhibited by the undoped sample and implies that the donor-like defects responsible for the Be-compensation are removed at low anneal temperatures. Eventually, a "critical" anneal temperature is reached, beyond which the sample exhibits p-type behaviour and the Fermi energy sits below mid-gap. For all samples that were p-type as-grown, Be $>2x10^{18}$ cm^{-3}, the carrier concentration increased steadily with anneal. After anneal at 800°C, the samples doped with $3x10^{17}$, $1x10^{18}$, $3x10^{18}$ and $6x10^{18}$ cm^{-3} exhibited hole concentrations of $2x10^{17}$, $7x10^{17}$, $2x10^{18}$ and $4x10^{18}$ cm^{-3}, respectively. The carrier concentrations did not recover to the doping concentration, indicating that some compensating defects remained in the sample after anneal at the highest temperature. In Figure 4.15, the mobility is shown as a function of doping concentration for all samples after anneal at different temperatures. The weakly Be-doped samples (i.e. those with doping $<2x10^{18}$ cm^{-3}) exhibited high mobilities in the range of 800 to 2000 cm^2/Vs, indicating that the samples were n-type as-grown. The more highly doped as-grown samples (Be$>2x10^{18}$ cm^{-3}) had mobilities expected for p-type conduction in the range of a few tens cm^2/Vs. The standard sample, doped with $3x10^{17}$ cm^{-3} Be exhibited a mobility of approximately 70 cm^2/Vs, which did not change with anneal. After anneal at 500°C and 550°C, the samples with Be doping of $1x10^{17}$ and $3x10^{17}$ cm^{-3} still exhibited high mobility values, $\sim$2000 cm^2/Vs. The sample doped with $1x10^{18}$ cm^{-3} Be exhibited reduced mobility of $\sim$100 cm^2/Vs after the 500°C anneal. After anneal at 650°C, all samples that were initially n-type (i.e. Be $<2x10^{18}$ cm^{-3}) exhibited mobilities consistent with p-type conduction. This suggests that the annealing process removed the donors compensating the dopant. The highly doped samples (Be $>2x10^{18}$ cm^{-3}) exhibited mobilities of 25 to 45 cm^2/Vs, as-grown, which increased steadily with anneal to values of 65-110 cm^2/Vs after anneal at 800°C, suggesting the removal of scattering centres.

4.4 Variable-Temperature Hall Effect Measurements

From the room-temperature Hall effect data described above, a computer model was developed that allowed an estimate to be made of the defect energy levels and their concentrations in the quaternary system. To further validate the model, an alternative technique was required to study the defect levels; one such method is variable-temperature Hall effect measurements. As discussed in Chapter 5, four levels (two electron traps, 2 hole traps) were needed to fully describe the material properties, so the simple "one-level model" for VT Hall effect measurements described in Section 2.3 is not valid; a number of defects influence the final carrier concentration.

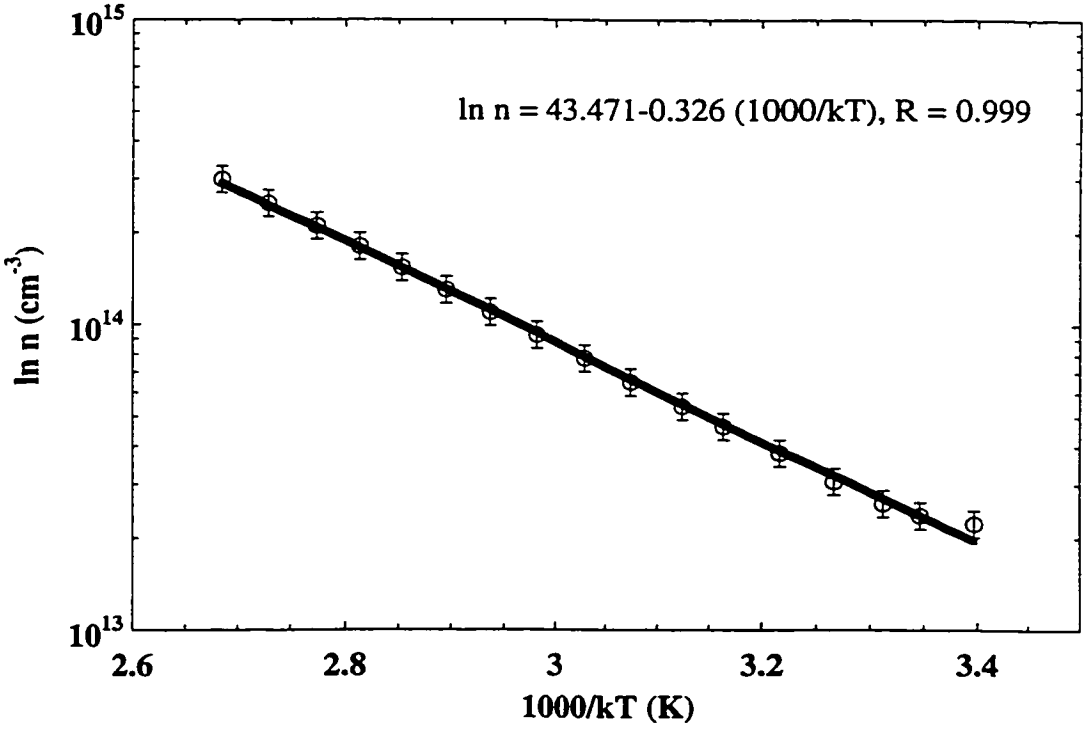

Figure 4.16: Arrhenius plot of the free carrier concentration in Be-doped ($3x10^{17}$ cm^{-3}) He-InGaAsP.

Therefore, it was necessary to compare the results from the experiment with the prediction from the computer simulation. Experimental measurements were performed over a temperature range 253 to 372 K on a sample doped with $3x10^{17}$ cm^{-3} Be. The model in Chapter 5 was used to simulate the expected carrier concentrations over the same temperature range for a similarly doped sample and the results were compared to the experimental data (Section 5.5.4). The sample, 2579, ($3x10^{17}$ cm^{-3} Be), was chosen because it was n-type at room temperature, instead of p-type, suggesting that its electrical behaviour was dominated by a donor-like trap above mid-gap. The measurements were carried out as described in Section 2.3. Figure 4.16 shows the experimental results in Arrhenius form, along with the best linear fit. The line had a slope corresponding to an energy level of 326±23 meV below the conduction band edge. The predicted value for the slope of this line was in reasonable agreement with the experimental results, as discussed further in Section 5.5.4.

4.5 Photoluminescence measurements of He-InGaAsP samples

A number of the samples used for the electrical measurements were also studied using low-temperature (16±2 K) photoluminescence (PL). All spectra were measured under the same conditions. It was known previously that InP samples grown with He-plasma exhibited very little luminescence [Mitchell (1995)], and this was found to be true for the quaternaries also. The electrical measurements suggested that PL studies may be possible with annealed He-InGaAsP samples since the conductivity of the samples recovered as the anneal temperature was increased. This implied that the free carrier concentration was much higher for these samples, probably due to the removal of non-radiative traps.

4.5.1 Undoped InGaAsP

Figure 4.17 shows the behaviour of the undoped He-plasma sample, 2154, compared to the reference sample (no plasma), 2155. Both samples were grown with a nominal room-temperature wavelength of 1.52 μm, which corresponds to a bandgap energy of approximately 0.82 eV. At 17 K, the sample temperature during the measurements, the bandgap energy should be approximately 0.89 eV. However, the reference exhibited a dominant peak at 0.865 eV (that did not change with anneal), which suggests that the actual composition of this sample may have been different from the quoted value. The peak intensity of the as-grown standard was approximately 1000 μV. A much weaker peak was seen at 0.835 eV (expanded in the figure).

The He-InGaAsP sample did not emit detectable PL, either as-grown or after anneal at temperatures below 650°C. Even after anneal at T¿600°C, the emitted intensity was weak. The appearance of PL and the subsequent increase in intensity of the signal from 2 μV at 650°C to 11 μV at 800°C suggests the removal of deep non-radiative traps. This is consistent with the observations of the University of Toronto group, that the lifetime of the optical carriers in the quaternary increases with anneal [Qian et al. (1997c)]. The spectrum was quite different from that of the standard sample: a number of broad peaks were seen at energies lower than the bandgap and the intensity of the peaks varied with anneal temperature. One broad peak, at 0.815 eV, was observed after anneal at 650°C. Two peaks were seen after anneal at higher temperatures; all peaks were broad and probably comprised several peaks. At 700°C, a distinct peak appeared at 0.75 eV, ~115 meV below the band-edge of the standard sample. It is possible that this peak is present in the shoulder of the 650°C peak, but it cannot be clearly discerned. The peak at 0.75 eV subsequently disappeared at higher anneal temperatures. Two superimposed broad peaks appear at 0.825 and

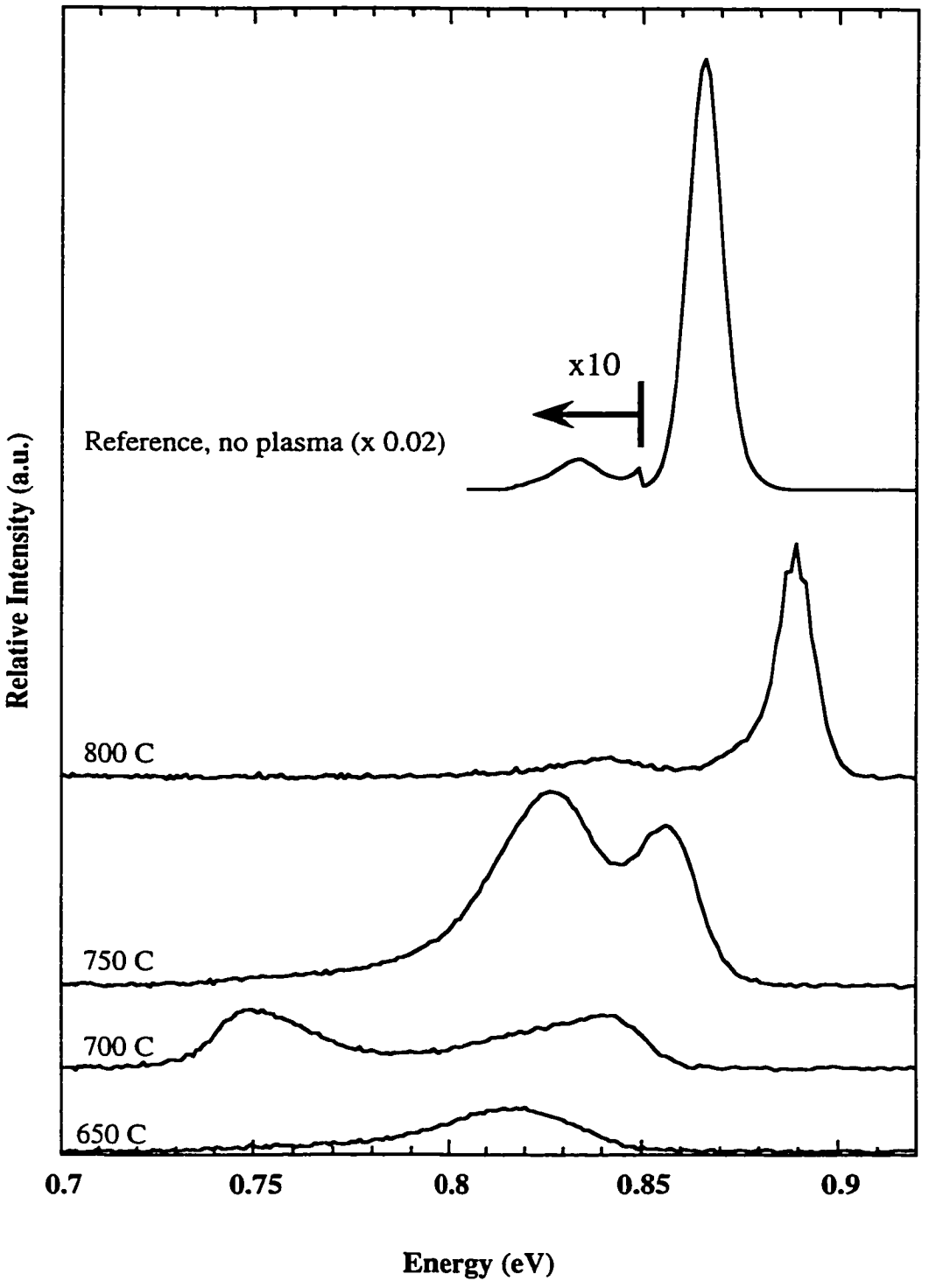

Figure 4.17: Effect of annealing on PL spectrum of undoped He-InGaAsP.

0.86 eV after anneal at 700°C. Finally, a high energy peak appears at 0.89 eV in the sample annealed at 800°C, which most likely corresponds to the bandgap transition, although it is 30 meV higher in energy than the standard sample, suggesting a slightly different composition. From this we can conclude that non-radiative defects dominate for this sample until they are removed by annealing.

4.5.2 Si-doped InGaAsP

As-grown samples of various Si-doping levels ($3x10^{17}$ to $3.5x10^{18}$ cm^{-3}, identical samples to those studied electrically) were subjected to PL measurements. No PL was detected, suggesting that the fastest transitions are non-radiative. Two of these samples ($3x10^{17}$ and $3x10^{18}$ cm^{-3} Si) were studied after anneal at different temperatures. A standard sample (no plasma) with $3x10^{18}$ cm^{-3} doping was also included.

The results for the weakly doped sample are shown in Figure 4.18. On anneal at or above 600 °C, weak PL was observed, suggesting the removal of the non-radiative defects. Like the undoped sample, the Si-doped sample exhibited broad peaks over the energy range of 0.75 to 0.85 eV, suggesting transitions via states in the bandgap. The same peaks were present at different intensities for all the anneal steps. For example, the peak at 0.75 eV (also present in the undoped sample) was most prominent after the 750°C anneal, but can be detected in all the other traces, with no shift on anneal. After anneal at 800°C, a prominent peak appeared at ~0.85 eV, most likely due to the bandedge transition. However, the broad shoulder at lower energies indicates that transitions via bandgap states were still occurring.

Figure 4.19 illustrates the effect of annealing the highly silicon-doped ($3x10^{18}$ cm^{-3}) He-plasma-assisted InGaAsP sample. The as-grown standard sample spectrum is plotted for comparison. The He-InGaAsP sample did not emit any detectable PL

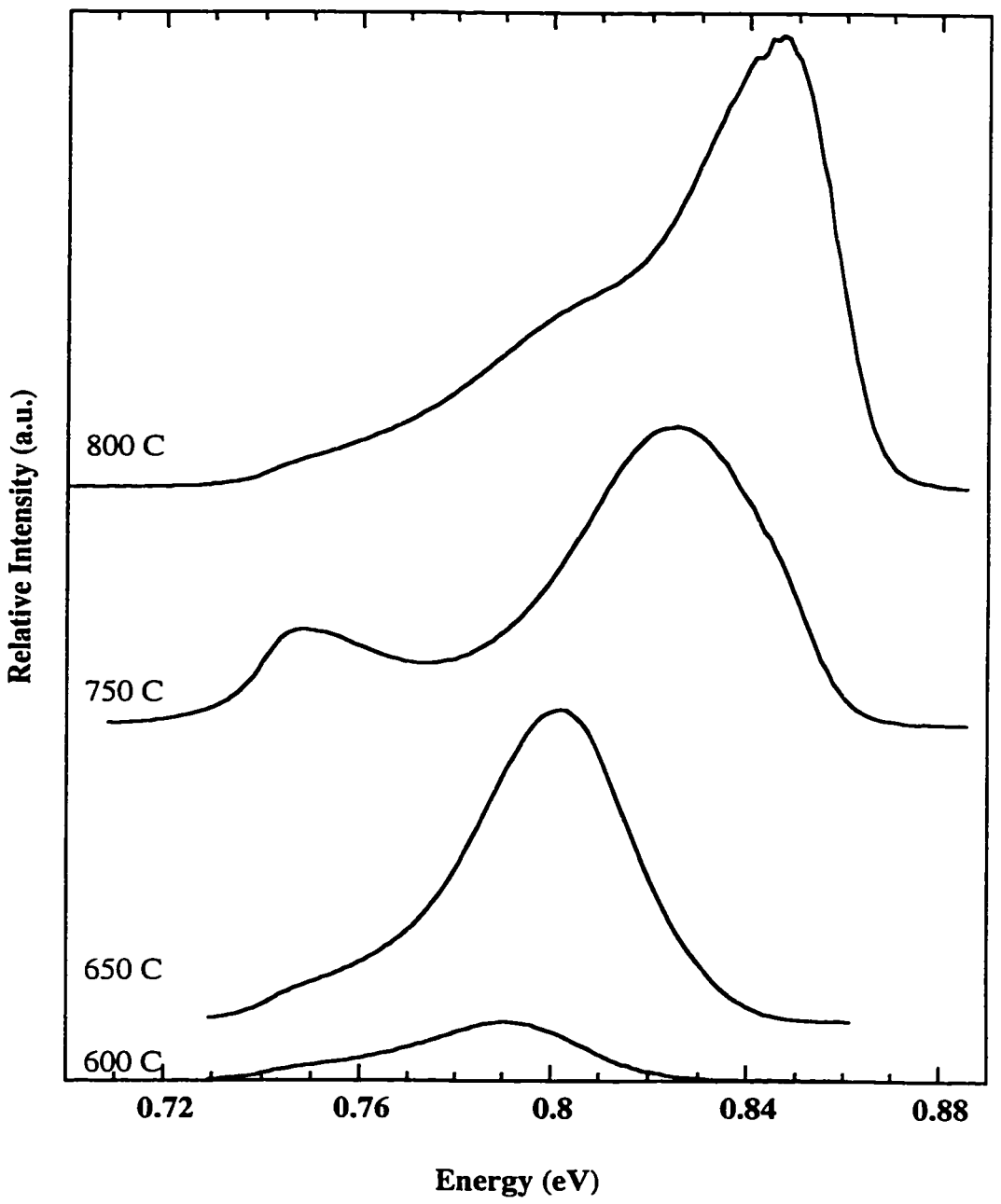

Figure 4.18: Effect of annealing temperature on PL spectrum of weakly Si-doped ($3x10^{17}$ cm^{-3}) He-InGaAsP.

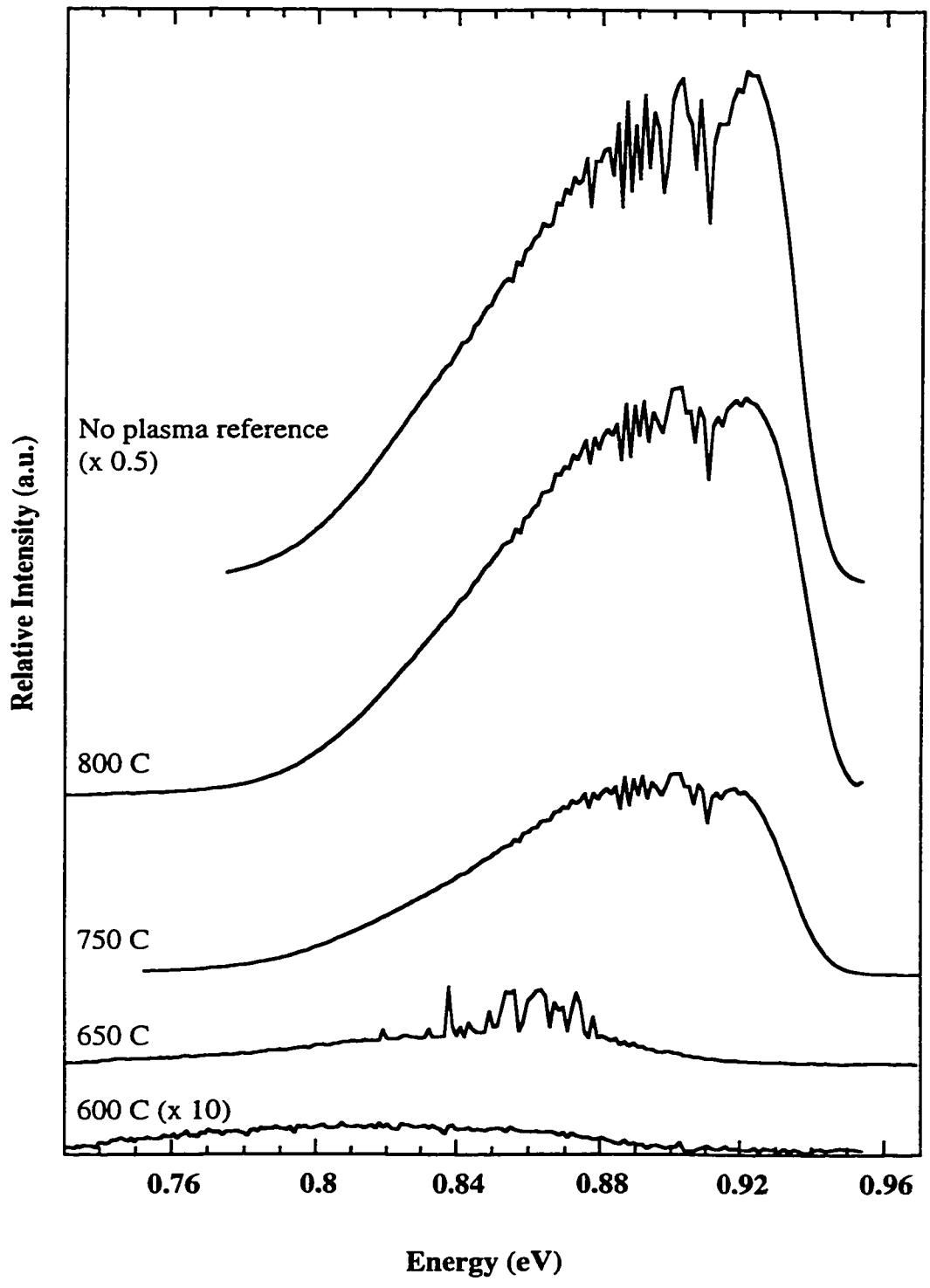

Figure 4.19: Effect of annealing temperature on PL spectrum of heavily Si-doped ($3x10^{18}$ cm^{-3}) He-InGaAsP.

until annealed at 550°C. All peaks were very broad; the high doping swamped all detail of the defects in these spectra and band-filling effects were seen at energies above the bandgap energy, for the standard and those He-plasma samples annealed at 750 and 800°C. The samples annealed at low temperature, 600 and 650°C, emitted weak PL and the intensity increased with anneal temperature. The spectra for the 750 and 800°C anneals were very similar in shape to that of the standard sample, indicating that the fraction of transitions via bandgap states was small.

4.5.3 Be-doped InGaAsP

A number of samples doped with different concentrations of Be ($1x10^{17}$ to $6x10^{18}$ cm^{-3}) were studied as-grown. None of these samples emitted detectable PL. Two of the samples ($3x10^{17}$ and $3x10^{18}$ cm^{-3} Be) were also studied after anneal. Figures 4.20 and 4.21 show the effect of annealing the $3x10^{17}$ and $3x10^{18}$ cm^{-3} Be-doped samples, respectively. Both spectra were similar; the emission was very broad and a steady increase in intensity occurred with increasing anneal temperature. No PL was observed for samples annealed at temperatures of $\leq$600°C. Photoluminescence was only emitted by samples that converted from n-type to p-type on anneal (as described above in the Electrical Results, Section 4.3). The emission occurred over an energy range of approximately 0.75 to 0.84 eV; since the emission energy was sub-bandgap, it seems likely that transitions involved mid-gap states. Unlike the silicon-doped samples, no distinct peaks could be determined; the spectrum comprised a number of overlapping peaks. The shoulder at higher energies (0.83 to 0.84 eV) may be due to bandedge transitions.

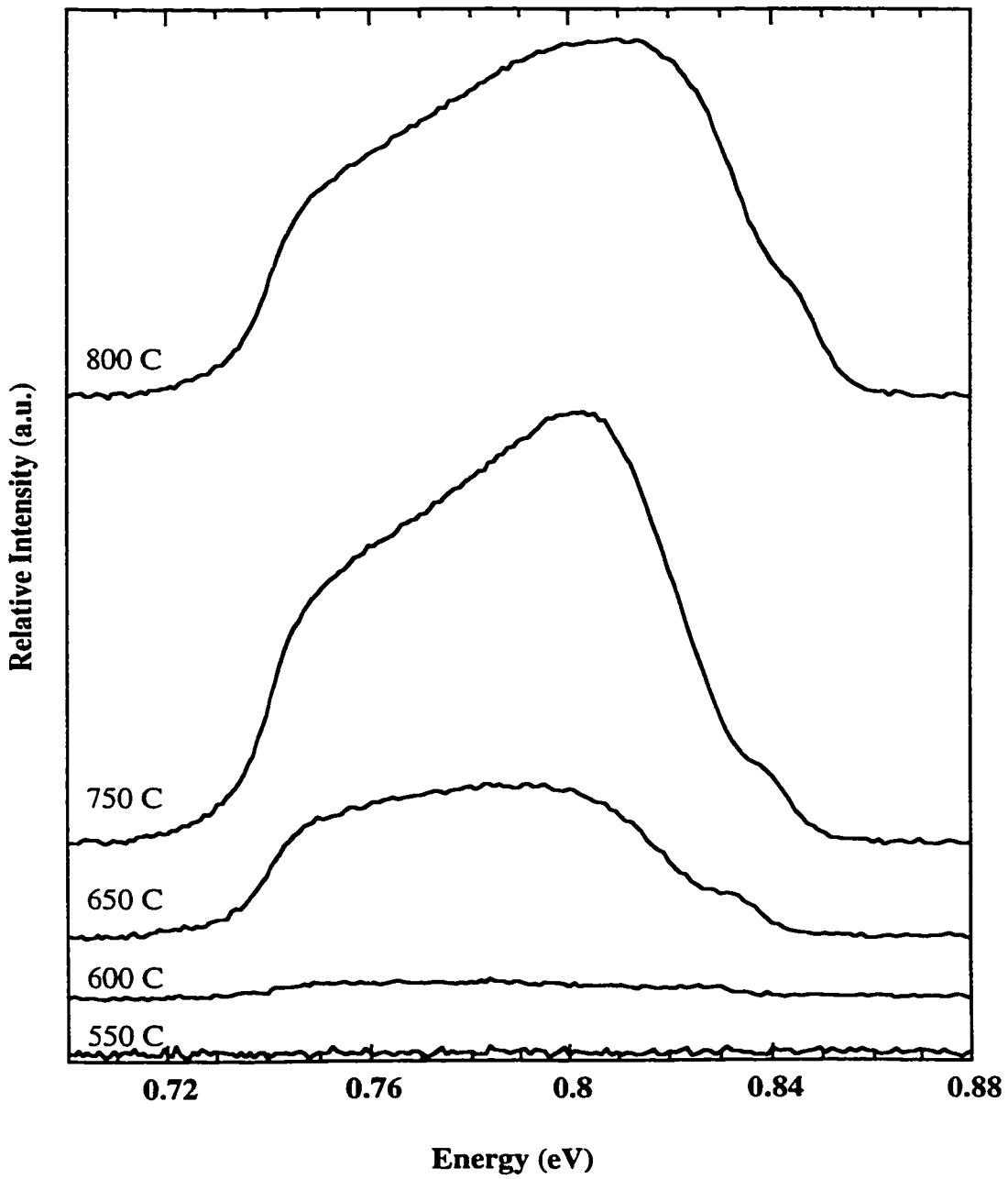

Figure 4.20: Effect of annealing temperature on PL spectrum of Be-doped ($3x10^{17}$ cm^{-3}) He-InGaAsP.

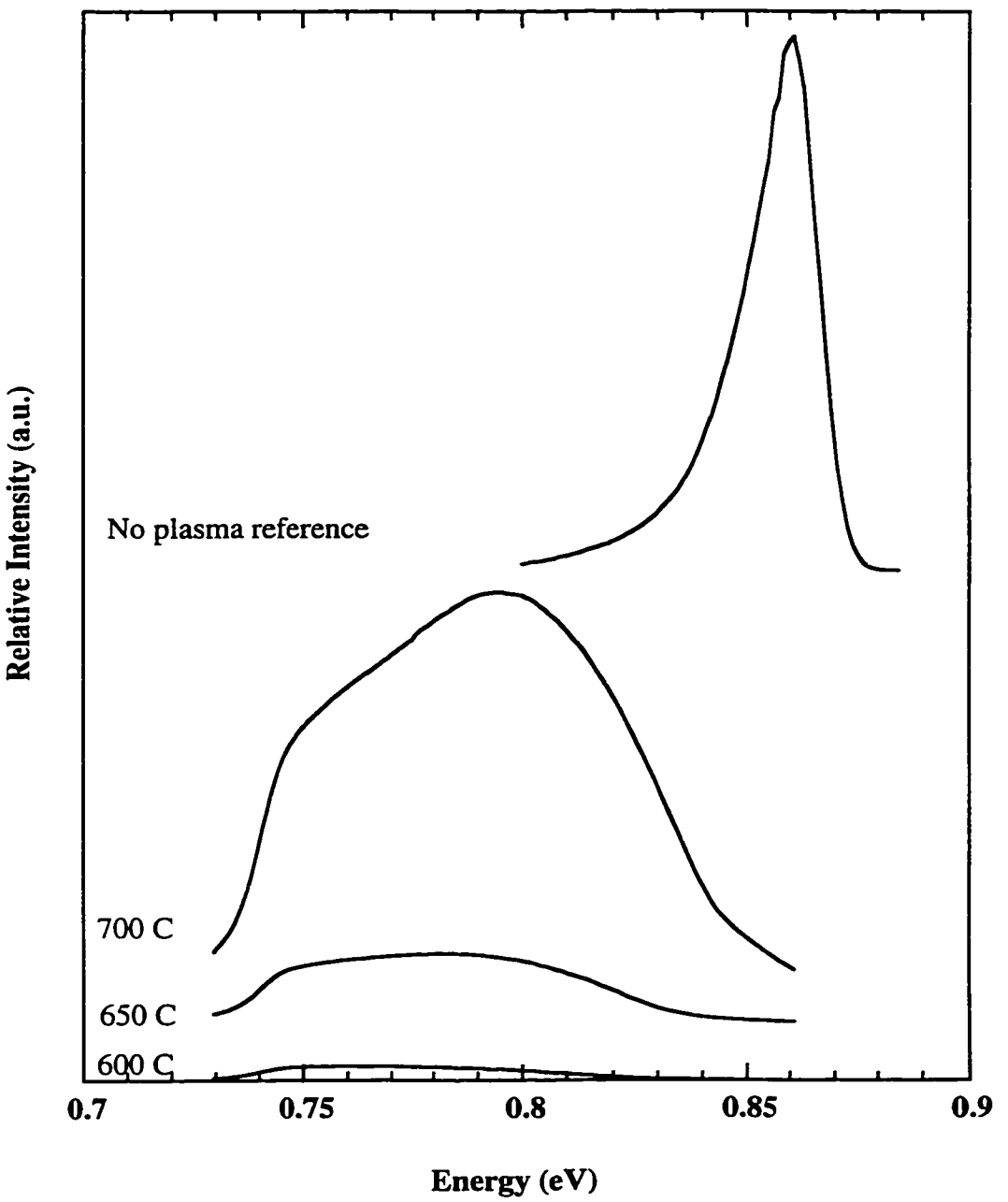

Figure 4.21: Effect of annealing temperature on PL spectrum of Be-doped ($3x10^{18}$ cm^{-3}) He-InGaAsP.

4.6 SIMS Results

In Chapter 3, we demonstrated that hydrogen was present in InP samples when the He-plasma was operated. Since some of the Be-doped quaternary samples were n-type as-grown, SIMS analysis was conducted on a specially-designed sample to determine whether hydrogen may be playing a role in the passivation of the Be dopant. This sample, shown in Figure 4.22, contained a number of different layers, both Be-doped and undoped. The first layer was a standard 1000 Å-thick undoped InP buffer layer. The second layer was a 2000 Å-thick InGaAsP layer doped with $1x10^{18}$ cm^{-3} Be and grown in the presence of atomic deuterium (generated by thermal dissociation). The third layer was identical to the second except that it was undoped. The He-plasma source was not in operation for these three layers. The fourth layer

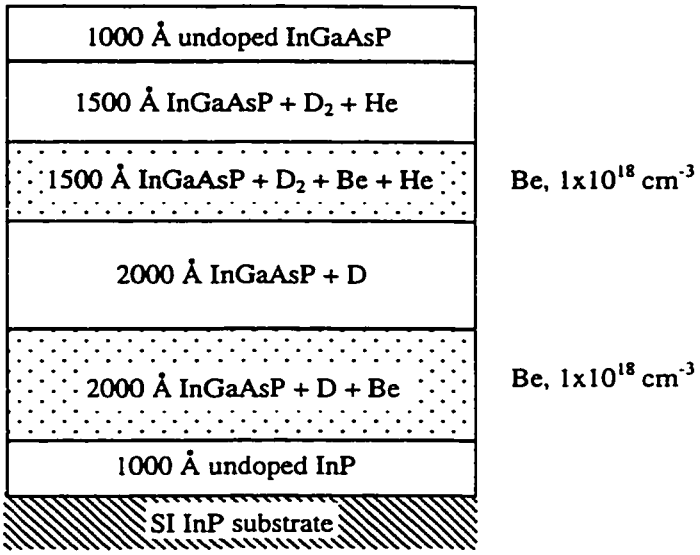

Figure 4.22: Quaternary structure sent for SIMS analysis.

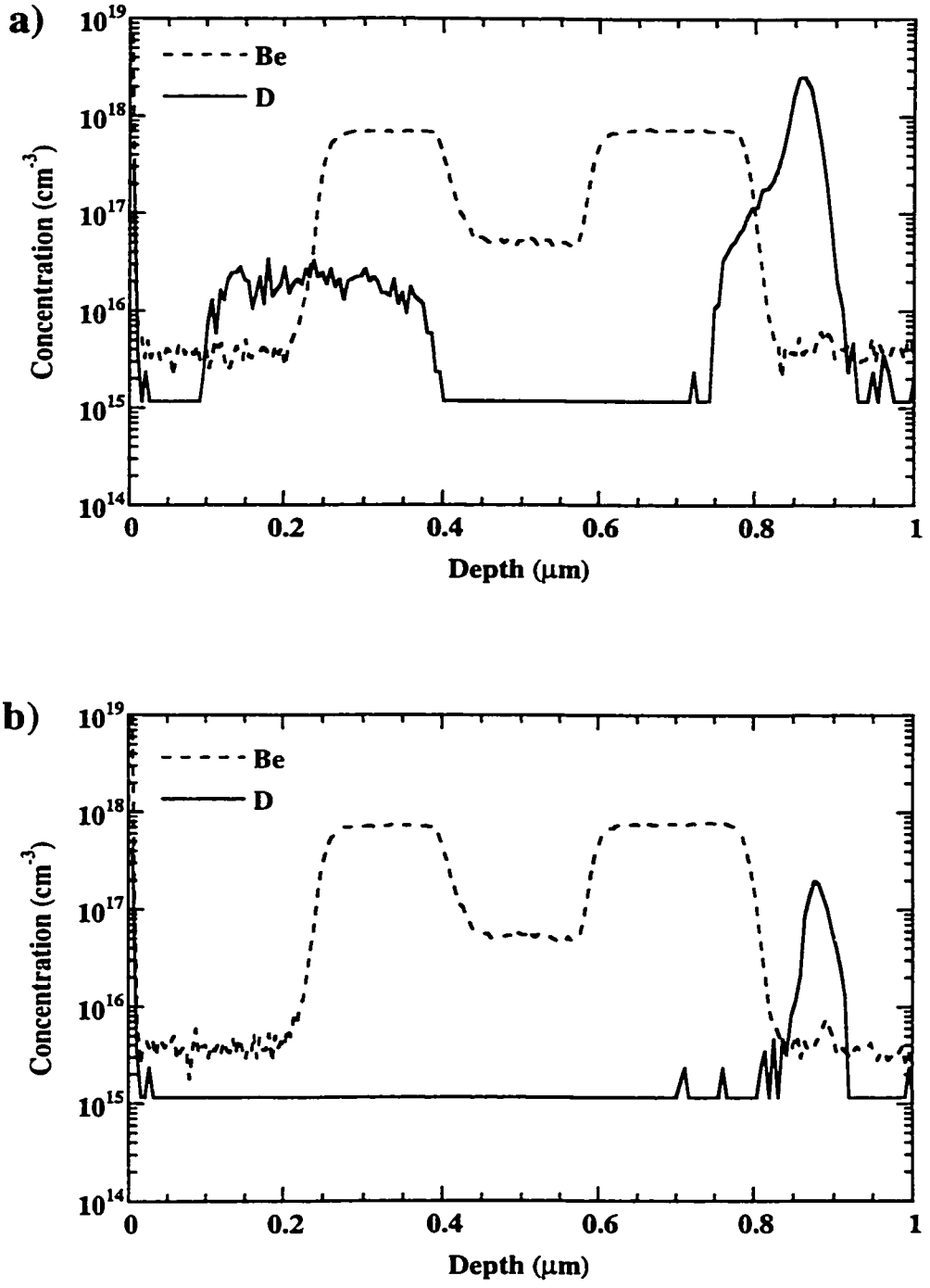

Figure 4.23: SIMS measurements for He-quaternary sample, a) before and b) after 10 second anneal at 700°C.

was a 1500 Å-thick layer of Be-doped InGaAsP ($1x10^{18}$ cm^{-3}) grown in the presence of deuterium gas and the helium plasma. The fifth layer was identical to the fourth except that it was undoped. It should be noted that some energetic deuterium, in the form of ions and excited atoms and molecules, would be generated in the ECR source due to backstreaming from the MBE chamber into the discharge chamber. Finally, a sixth layer was added to cap the structure: 1000 Å InGaAsP with no doping, deuterium or He-plasma. The same structure was studied with SIMS before and after a 10 second anneal in the RTA at 700°C.

The SIMS results for this structure are shown in Figure 4.23. In the as-grown sample, Figure 4.23a, deuterium was observed only in the layers grown in the presence of the He-plasma. The large peak at 0.9 μm is due to interface contamination. The concentration of deuterium was approximately $2x10^{16}$ cm^{-3}. The usual operating pressure of the GSMBE chamber is $4x10^{-5}$ Torr (due mainly to residual hydrogen from the dissociation of the Group V hydrides), while during growth with deuterium it was $2x10^{-4}$ Torr. Therefore, the ratio of deuterium to residual hydrogen in the chamber was 4:1. This means that for every four parts deuterium observed with SIMS, there may be one part hydrogen which was not detected, so the total concentration of deuterium plus hydrogen in this sample can be estimated as approximately $2.5x10^{16}$ cm^{-3}. This concentration of "hydrogen" would not be enough to cause significant passivation of the 10^{18} cm^{-3} Be ions in the sample. Also, as observed for He-InP, the concentration of D was independent of the presence of Be, suggesting that the incorporated deuterium is not necessarily associated with the Be site. Therefore, there does not seem to be an obvious connection between the hydrogen concentration in the quaternary and the Be doping, suggesting that hydrogen passivation plays a relatively small role, at best, in the behaviour of the quaternary. Other contaminants present

in the chamber during growth are oxygen and carbon. These were also measured by SIMS and neither was found to be present in the samples beyond standard background levels (approximately $1x10^{17}$ cm^{-3}) except at the initial growth interface. Finally, for the annealed sample, all the deuterium incorporated into the He-plasma layers has been reduced to a concentration $\lesssim 10^{15}$ cm^{-3} after the anneal step.

4.7 Summary

The He-plasma quaternaries exhibit the same trends as He-InP. The positron annihilation measurements showed that open volume defects were present in this system. All samples that were n-type as-grown, whether undoped or doped with Be or Si, exhibited very similar as-grown normalized S parameters of ~1.03, which subsequently increased with anneal at low temperatures. For the Si-doped and undoped samples, $S_{Epi}/S_{Substrate}$ finally saturated at approximately 1.06, suggesting that the size of the open volume defects reached a maximum, possibly because all the mobile defects had already agglomerated to form larger, immobile defects. The weakly Be-doped sample showed a decrease in the S parameter at anneal temperatures >650°C, which suggests that some of the defects were no longer detectable by the positrons because they are positively charged. This effect was even more pronounced in the highly Be-doped sample, which exhibited a normalized S parameter of 1.002, no different from the standard (no plasma) sample.

The low resistivity of the quaternary, compared to InP, allowed more reliable Hall effect measurements. The undoped and Si-doped samples showed reduced carrier concentrations and mobilities as compared to a standard "non-plasma" sample. This suggests the presence of an electron trap. Also, Be-doping (at concentrations $<2x10^{18}$ cm^{-3}) did not produce p-type samples, which suggests that the Be was either passi-

vated or compensated. SIMS studies indicated that there was insufficient hydrogen in the system for significant Be-H passivation, thereby a donor-like defect may be present to compensate the Be. This is possibly the defect observed with positron annihilation measurements, especially since the defect is not visible when the sample is p-type, i.e. when the Fermi energy is below mid-gap. As mentioned in Section 3.2, Chen et al. (1996) concluded from positron rate distribution measurements on bulk InP samples that in n-doped and SI-type InP, both indium and phosphorus vacancies are seen, but in p-type InP, only the indium vacancies can be seen, because once the Fermi energy was below midgap, the phosphorus vacancy (a donor-like defect) became positively-charged. Finally, the He-InGaAsP became luminescent once it was annealed at T>600°C, which indicates that the defects responsible for the fast optical behaviour observed by Qian et al. (1997a) were removed. This is entirely consistent with the electrical measurements, which indicated that, on anneal, the carrier concentration increased for both Be-and Si-doped samples, suggesting the removal of traps from the system.

Chapter 5

Fermi-Dirac Statistics Modeling

5.1 Introduction

The free carrier concentration in a semiconductor sample can always be related to the corresponding Fermi energy, E_F. Any defects present in the system affect the free carrier concentration and consequently the Fermi energy. Therefore, comparison of the Fermi energy values calculated from the Hall effect analysis with those generated from a suitable computer model allows the estimation of plausible trap energy levels and concentrations. To accomplish this, a program was written in Matlab^{TM} to calculate the expected carrier concentrations and Fermi levels in a doped semiconductor as a function of its doping concentration. The calculations for a number of different conditions, such as trap type, energy and concentration, were then compared to the room-temperature Hall effect data for undoped, Si- and Be-doped quaternary samples. The model parameters were adjusted until the best fit to all the data was obtained, with the minimum number of trap levels. By using E_F, the complications of studying the change in the majority free-carrier type were avoided in the case of the Be samples, where the majority carrier type changed from the electron to the hole with a) increasing dopant concentration and b) annealing temperature. Also, by using the Fermi energy, the results for all samples, both Si- and Be-doped,

could be plotted simultaneously. The details of the Fermi-Dirac statistics model are described below. In the summary, the final model is discussed in relation to the experimental results for the quaternary samples described in Chapter 4.

5.2 Theory

For a standard semiconductor at room temperature, the free carrier concentration should match the doping concentration, since the dopants are chosen with very low ionization energies (a few meV typically) and therefore are expected to be fully ionized at room temperature. However, in a material that contains traps, this carrier concentration is reduced. The effects of doping and deep traps can be described using Fermi-Dirac statistics. All the modeling is based on the charge-neutrality equation for a system in equilibrium [Pierret, (1989), page 123]:

$$p - n + N_D^+ - N_A^- + N_T^+ - N_T^- = 0 \tag{5.1}$$

where p (n) is the concentration of holes (electrons), N_D (N_A) is the donor (acceptor) concentration and N_T^+ (N_T^-) is the concentration of donor-like (acceptor-like) traps. This equation is true for any system in equilibrium, regardless of the doping concentration etc. Blakemore [(1962), p. 250] defines a defect as donor-like if it is electrically neutral when full and $+e$ ionized when empty. In contrast, a defect is acceptor-like if it is neutral when empty and $-e$ charged when full. The electron and hole concentrations are related to the Fermi energy as follows [Pierret, (1989), p. 118] for any system:

$$n = N_C \Im_{1/2}(\eta_C) \qquad \text{or} \tag{5.2}$$

$$p = N_V \Im_{1/2}(\eta_V) \tag{5.3}$$

where N_C (N_V) is the effective density of states for the conduction (valence) band, E_F is the Fermi energy, E_C (E_V) defines the energy of the conduction (valence) band edge and $\Im_{1/2}$ is the Fermi-Dirac integral of order 1/2, defined as:

$$\Im_{1/2}(\eta) = \int_0^\infty \frac{\xi^{1/2} d\xi}{1 + e^{\xi - \eta}} \tag{5.4}$$

where η is:

$$\eta_C = (E_F - E_C)/kT \qquad \text{for the conduction band or} \tag{5.5}$$

$$\eta_V = (E_V - E_F)/kT \qquad \text{for the valence band} \tag{5.6}$$

At room temperature, we shall assume that the dopants are fully ionized, so $N_D^+ = N_D$ and $N_A^- = N_A$. This may lead to inaccuracies in the calculations for the very highly-doped samples, since partial ionization effects have been ignored, but modelling the high-doping effects becomes very difficult for the quaternary system, as discussed in Section 5.4. The number of ionized traps can be determined from the defect energy level in the band gap (analogous to the energy levels of the dopant elements) and trap concentration:

$$N_T^+ = \frac{N_T}{1 + g_T e^{(E_F - E_T)/kT}} \tag{5.7}$$

where N_T^+ is the ionized trap concentration for donor-like traps, N_T the total trap concentration, g_T the degeneracy of the traps (the number of different ways in which the trap may be filled) and E_T the energy level of the donor-like trap in the band gap. By analogy to the equation for intentionally ionized acceptors, the equation for acceptor-like traps takes the form:

$$N_T^- = \frac{N_T}{1 + g_T e^{(E_T - E_F)/kT}} \tag{5.8}$$

where N_T^- is the ionized trap concentration for acceptor-like traps, N_T the total trap concentration and E_T the energy level of the acceptor-like trap in the band gap. Due

to the difficulty of establishing g_T experimentally, it is usually assumed that g_T=1 for both donor- and acceptor-like traps. The energy level, E_T, is then quoted with this assumption:

$$N_T^+ = \frac{N_T}{1 + g_T e^{(E_F - E_T)/kT}} = \frac{N_T}{1 + e^{(E_F - E_T)/kT}} \tag{5.9}$$

The final form of the charge balance equation is:

$$N_C \Im_{1/2}([E_F - E_C]/kT) - N_V \Im_{1/2}([E_V - E_F]/kT) - N_D + N_A - \frac{N_T}{1 + e^{(E_F - E_T)/kT}} + \frac{N_T}{1 + e^{(E_T - E_F)/kT}} = 0 \tag{5.10}$$

It then remains to solve this equation for E_F. The free electron and hole concentrations can be found by substituting the Fermi energy, E_F, back into the following equations:

$$n = N_C \Im_{1/2}([E_F - E_C]/kT) \tag{5.11}$$

$$p = N_V \Im_{1/2}([E_V - E_F]/kT) \tag{5.12}$$

Therefore, for a given doping concentration, trap density and trap energy, the Fermi energy and associated carrier concentration can be calculated and compared with the experimental data.

5.3 Details of the Calculations

Simplifications can be made to the Fermi function, $\Im_{1/2}([E_F - E_C]/kT)$, if the semiconductor system is non-degenerate, that is, if the Fermi energy lies at least $3kT$ from either bandedge. If this is the case, then the carrier concentrations can be calculated from the simplified expressions:

$$n = N_C e^{(E_F - E_C)/kT} \qquad \text{if } E_C - E_F \geq 3kT \tag{5.13}$$

$$p = N_V e^{(E_V - E_F)/kT} \qquad \text{if } E_F - E_V \geq 3kT \tag{5.14}$$

This condition imposes the following maximum carrier concentration (hence ionized dopant concentration) for which a system is non-degenerate:

$$n = N_C e^{-3} \quad \text{for the free electron concentration or} \tag{5.15}$$

$$p = N_V e^{-3} \quad \text{for the free hole concentration.} \tag{5.16}$$

The effective density of states is calculated as follows:

$$N_C = 2(2\pi m_c kT/h^2)^{3/2} \tag{5.17}$$

$$N_V = 2(2\pi m_h kT/h^2)^{3/2} \tag{5.18}$$

where m_c (m_h) is the effective mass of the electron (hole), k is the Boltzmann constant and T is the temperature in Kelvin. For the effective hole mass, m_h, the contribution from the heavy and light holes must be taken into account:

$$m_h = (m_{hh}^{1.5} + m_{lh}^{1.5})^{2/3} \tag{5.19}$$

The quaternary material used in this work had a bandgap energy of $E_g = 0.8$ eV, so the effective masses for the electron, heavy hole and light hole were calculated (see Appendix) to be $m_c = 0.0474m_e$ (where m_e is the free electron mass), $m_{hh} = 0.4015m_e$ and $m_{lh} = 0.0638m_e$. This resulted in values of $N_C = 2.58 \times 10^{17}$ cm^{-3} and $N_V = 6.76 \times 10^{18}$ cm^{-3} and maximum limits for non-degeneracy of $n = 1.28 \times 10^{16}$ cm^{-3} and $p = 3.37 \times 10^{17}$ cm^{-3}. For doping levels greater than these n and p values (almost all the samples in this study), the semiconductors may be degenerate, depending on the traps present, in which case the simplifying assumptions would no longer be valid. Therefore, the full Fermi-Dirac expressions were used for the calculations. However, to minimize computing time, an approximation was used in place of the full integral $\Im_{1/2}$ [Blakemore, (1982)], which introduced a maximum 0.5% error into the results:

$$\Im_{1/2}(\eta) \simeq [e^{-\eta} + \zeta(\eta)]^{-1} \tag{5.20}$$

where

$$\zeta(\eta) = 3(\pi/2)^{1/2}[(\eta + 2.13) + (|\ (\eta - 2.13)\ |^{2.4} + 9.6)^{5/12}]^{-3/2} \tag{5.21}$$

and

$$\eta_C = (E_F - E_C)/kT \qquad \text{or} \tag{5.22}$$

$$\eta_V = (E_V - E_F)/kT \tag{5.23}$$

In order to compare the models with the experimental data, the measured carrier concentrations were converted to Fermi energy values using [Blakemore, (1982)]:

$$\eta \simeq \frac{lnu}{1 - u^2} + \frac{(3\sqrt{\pi}u/4)^{2/3}}{1 + [0.24 + 1.08(3\sqrt{\pi}u/4)^{2/3}]^{-2}} \tag{5.24}$$

where

$$u = \Im_{1/2}(\eta) = n/N_C \text{ or } p/N_V \tag{5.25}$$

and

$$E_F = \eta kT + E_C \tag{5.26}$$

or

$$E_F = E_V - \eta kT \tag{5.27}$$

5.4 High Doping Considerations

For highly-doped semiconductors, simply using Fermi-Dirac statistics does not account for all the physical effects occurring in the system [Pierret, (1989), p. 132]. The presence of the dopant causes physical changes to the system that become significant when the doping concentration is high. Lee and Fossum (1983) described the considerations for highly n-doped silicon:

a) "many-body effects" caused by the interactions between the free carriers or between the free carriers and the dopants:

i) electron-electron interactions cause the conduction bandedge to be shifted down in energy, so bandgap narrows

ii) electron-hole interactions cause the valence bandedge to be shifted up, so bandgap narrows

iii) electron-donor interactions cause Coulomb screening of the ionized donors, thereby reducing the impurity ionization energy ($E_C - E_D$). This does not affect the bandgap energy, since it is believed that the impurity band moves up and into the band.

b) the random distribution of impurities causes fluctuations in the local electrostatic potential which leads to two effects:

i) macroscopically, both the conduction and valence band edges appear to tail into the bandgap; the bands are no longer parabolic

ii) an impurity band forms, due to overlap of the electron wave functions at the bound impurity states and because the random distribution of the dopants causes a statistically averaged variation in the impurity energy level. Lee and Fossum (1983) concluded that the influence of this band on the bandgap is difficult to calculate, but justified its being neglected in their model on the grounds that the band was narrow before entering the conduction band and once in the band, the bound states would be completely screened by electrons and therefore indistinguishable from the host atoms.

De et al. (1993) used the following equations, based on the calculations of Marshak and Van Vliet (1984), for the InGaAsP quaternary system under the heavy doping

condition:

$$n = \left(\frac{a_n n_i \Im_{1/2}(\eta_n)}{e^{\eta_n}}\right) exp\left(A\frac{\Delta Eg}{kT}\right) exp\left(\frac{(E_{fn} - E_i)}{kT}\right) \tag{5.28}$$

and

$$p = \left(\frac{a_p n_i \Im_{1/2}(\eta_p)}{exp(\eta_p)}\right) exp\left((1-A)\frac{\Delta Eg}{kT}\right) exp\left(\frac{(E_i - E_{fp})}{kT}\right) \tag{5.29}$$

where $\Im_{1/2}(\eta)$ is the Fermi integral of order 1/2, η_n (η_p) is the reduced Fermi energy of the electron (hole), ΔE_g is the bandgap narrowing term, A is the "asymmetry factor", k is the Boltzmann constant, T is temperature in K, E_i and E_{fn} (E_{fp}) are the intrinsic Fermi level and the quasi-Fermi level for the electron (hole) and a_n (a_p) is the parameter for non-parabolic band structure [Marshak and van Vliet, (1984)]. However, it is not straightforward to use these equations; insufficient data are available on bandgap narrowing as functions of doping for the quaternary system, so authors usually assume that the band gap narrowing for InGaAsP is the same as for GaAs [Dutta (1980), Sermage et al. (1983)]:

$$\Delta E_g = -1.6 \times 10^{-8}(p^{1/3} + n^{1/3}) \quad \text{(eV)} \tag{5.30}$$

where n and p are in units of cm^{-3} [Casey and Stern (1976)].

From the above, one can see that incorporating high-doping effects into the computational analysis becomes highly involved and probably would not provide much more insight into the behaviour of the He-plasma-assisted MBE materials, especially given the uncertainties both in the measurements and the calculations. However, before omitting these effects, we can gain an estimate of how much high doping affects the calculations by using some relatively straightforward estimates developed by Bugajski and Lewandowski (1985) for n-InP. The analysis was broken down into a number of different effects: i) band-gap shrinkage due to the exchange interaction among the free carriers and ii) band tailing effects due to the Coulomb interaction of free carriers with ionized impurities.

i) experimentally, the electron-electron interaction was found to reduce the band-gap by an amount:

$$E^e = 2.25 \times 10^{-8} n^{1/3} \quad \text{(eV)} \tag{5.31}$$

where, once again, n is in cm^{-3}. This gives a correction to the bandgap of -35.7 meV for n-InP doped with 4x10^{18} cm^{-3} Si, for example.

ii) the band-tailing effect due to electron-impurity interaction is taken into account by a correction (including the non-parabolic bands) of

$$E^c = \left(\frac{\pi^{4/3}\hbar^2}{3^{1/3}}\right)\left(\frac{1}{em_e}\right) n^{2/3}\left[1 - 1.660(3\pi^2)^{2/3}\left(\frac{\hbar^2}{2m_e}\right)\frac{n^{2/3}}{E_g}\right] \quad \text{(eV)} \tag{5.32}$$

where $\hbar$ is Planck's constant/2π, $m_e = 0.079m_0$ is the effective mass of the electron in InP, and n is in cm^{-3}. This gives a value of -68 meV for a doping level of 4x10^{18} cm^{-3}.

The total reduction in the bandgap due to high-doping effects is then approximately 100 meV, which gives an error of approximately 10% in InP at the highest doping concentrations. Since the experimental error is of the same order ($\sim$10%), it is unnecessary to include the effects of high doping on calculating the exact positions and concentrations of the traps in this material. Also, in the above estimates, a value of N_D was used for n, that is, no traps were present to reduce the carrier concentration. In the case of He-plasma materials, the situation is less straightforward, since $n < N_D$ due to the presence of traps. Therefore, the calculation would require a certain number of iterative steps in order to estimate the Fermi energy correctly; the bandgap-narrowing depends on n, which can only be found numerically by knowing the values of E_F and the bandgap. In conclusion, then, this analysis is a first approxi-

mation (using Fermi-Dirac statistics only) and hence will provide a semi-quantitative explanation of the material properties.

5.5 Analysis of Experimental Results

5.5.1 Si-doped He-InGaAsP

The Hall effect data for the silicon samples were the more straightforward results to analyze, since the carrier concentration of the samples steadily increased with increase in doping and anneal temperature. In contrast, the weakly Be-doped samples were n-type, exhibited reduced carrier concentration with weak Be-doping and low anneal temperatures and finally became p-type when sufficiently high anneal temperatures were used. For the silicon-doped samples, the doping ranged from $1x10^{17}$ cm^{-3} to $3.5x10^{18}$ cm^{-3}. The acceptor concentration was taken to be $N_A = 0$.

To gain an idea of how different trap types affected the results, calculations were performed initially with only one type of trap present (either a donor- or an acceptor-like trap) for: a) a given trap concentration at a number of different trap energy levels in the bandgap; and b) for a given trap energy at different concentrations. Additional traps at different levels were then added, as necessary, until an appropriate solution was found that best fitted the experimental data.

It was quickly found that placing donor-like traps in the bandgap did not cause the reduced electron concentration observed experimentally. This type of trap only enhanced the electron carrier concentration. Acceptor-like (electron) traps, on the other hand, did reduce the electron concentration, as illustrated in Figures 5.1 to 5.4. These figures show the carrier concentration as a function of Si-doping, to illustrate the effect of introducing a single trap level into the system. To generate each of these plots, a specific trap energy was selected and then the trap concentration was varied

to see whether a suitable fit could be obtained. Plots are shown for traps of energy 0.2, 0.4, 0.6, and 0.7 eV above the valence band edge at a number of different trap concentrations: 0, $1x10^{17}$, $3\ x10^{17}$, $1x10^{18}$ and $3x10^{18}$ cm^{-3}. The experimental values obtained from room temperature Hall effect measurements are also plotted; since the error bars are smaller than the data markers, they have been omitted for clarity. It can be seen that, as the trap is positioned lower in the band gap, the intercept on the y-axis (carrier concentration for the undoped sample) is lowered. Also, the trap concentration affects the doping level at which the carrier concentration rapidly rises; the concentration at which the carrier concentration recovers is approximately the trap concentration. This behaviour indicates that when the trap density exceeds the dopant concentration, the carrier concentration is due to thermal activation of electrons from the trap level to the conduction band. It can also be seen that it is not possible to describe the effect of a particular trap level with a trap of different energy or concentration; the two parameters are independent enough that the shape of the curve uniquely defines the trap level and concentration within a certain (subjective) range. This forms the basis of the modeling approach, since, essentially, we are stating that a particular trap dominates the Fermi level only for a certain range of energies in the bandgap; the defect causes the Fermi energy to be "pinned". Of course, this does not rule out the possibility that a number of different trap energies and concentrations could combine to give an "average" carrier concentration profile, which only appears as a single defect level experimentally. However, by only using the minimum number of levels, we are identifying the *dominant* trap in a particular bandgap energy range; introducing a number of traps to accomplish the same effect would not improve the qualitative understanding of the material behaviour.

From Figures 5.3 and 5.4 it can be seen that the data, particularly for the

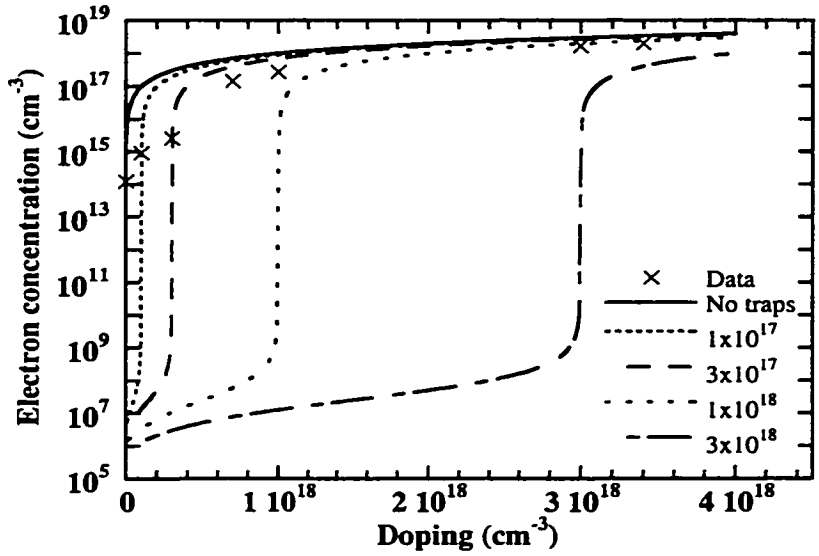

Figure 5.1: Calculated carrier concentrations for acceptor-like traps of various densities placed 0.2 eV above the valence band edge.

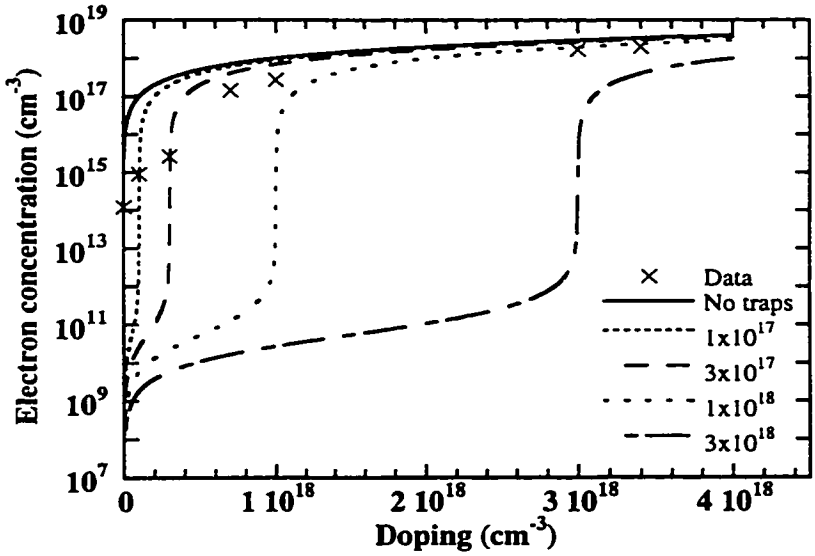

Figure 5.2: Calculated carrier concentrations for acceptor-like traps of various densities placed 0.4 eV above the valence band edge.

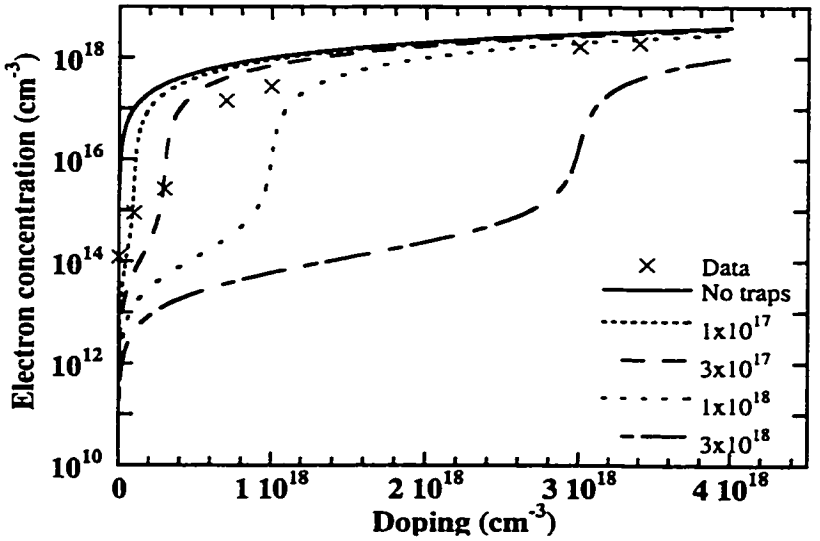

Figure 5.3: Calculated carrier concentrations for acceptor-like traps of various densities placed 0.6 eV above the valence band edge.

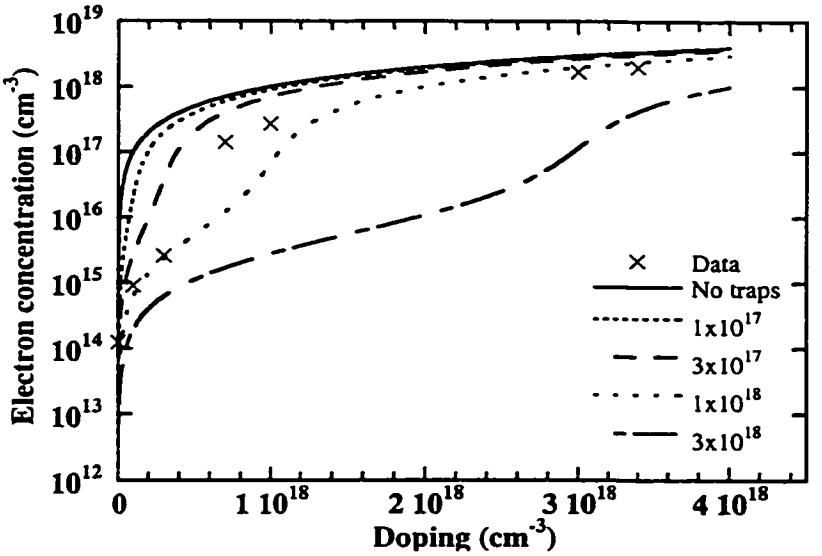

Figure 5.4: Calculated carrier concentrations for acceptor-like traps of various densities placed 0.7 eV above the valence band edge.

low doping concentrations, are best fitted by traps of energy 0.6-0.7 eV above the valence band with a concentration between 3 x10^{17} and 1x10^{18} cm^{-3}. By comparison of the models with the data, a trap energy level of E_{T1}=0.68 eV above the valence band was used with a trap concentration of 5x10^{17} cm^{-3}, as illustrated in Figure 5.5. As we would expect, once the traps are filled (i.e. the doping exceeds the trap concentration or, alternatively, the Fermi energy has risen above the trap energy), they do not substantially affect the carrier concentrations of samples with a much greater doping concentration. From Figure 5.5, the 5x10^{17} cm^{-3} traps at (E_V + 0.68) eV cannot account for the low carrier concentrations seen experimentally for doping levels >1x10^{18} cm^{-3}. This suggests that a second acceptor-like trap is present that affects the higher doping concentrations. This was addressed by including in the model a second trap, lying above the conduction band edge, at an energy of E_{T2}=0.85 eV and a concentration of 1x10^{18} cm^{-3}. This trap dominates the Fermi level position once the traps at E_{T1} are filled. We must remember, however, that the energy levels found from this model, particularly for the defect at E_{T2}=0.85 eV, are only an estimate since a number of approximations were made regarding the highly-doped samples; E_{T2} lies approximately 50 meV above the conduction bandedge, yet the error in this calculation is $\sim$ 100 meV (Section 5.4). The effects of both traps are illustrated in Figure 5.6.

5.5.2 Be-doped He-InGaAsP

As mentioned previously, the Be-doped samples were more complicated to analyze because the samples doped with <2x10^{18} cm^{-3} were n-type as-grown, not p-type as expected for Be. Hence, it was more appropriate to plot the Fermi energy, rather than the carrier concentration, versus doping, so that both the Si- and Be-doped samples could be modeled in a universal way. The experimental data for all

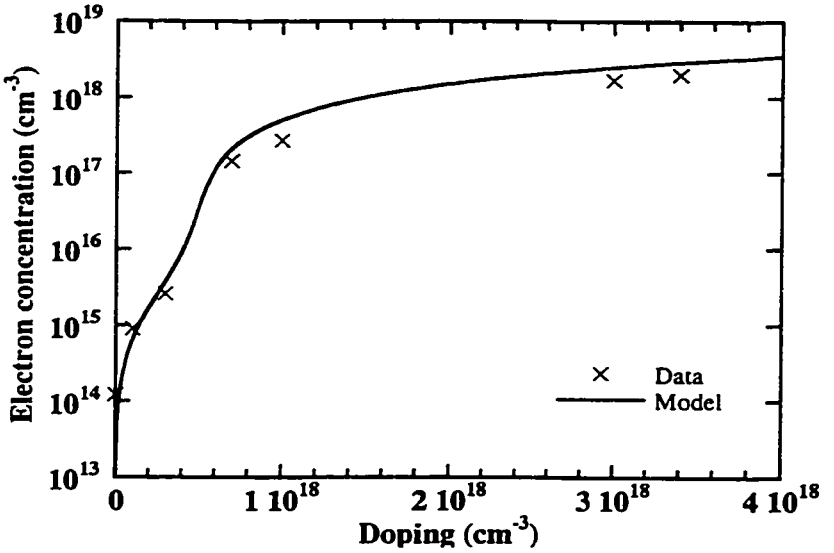

Figure 5.5: Calculated carrier concentrations for acceptor-like traps with an energy level 0.68 eV above the valence band edge and a concentration of $5x10^{17}$ cm^{-3}.

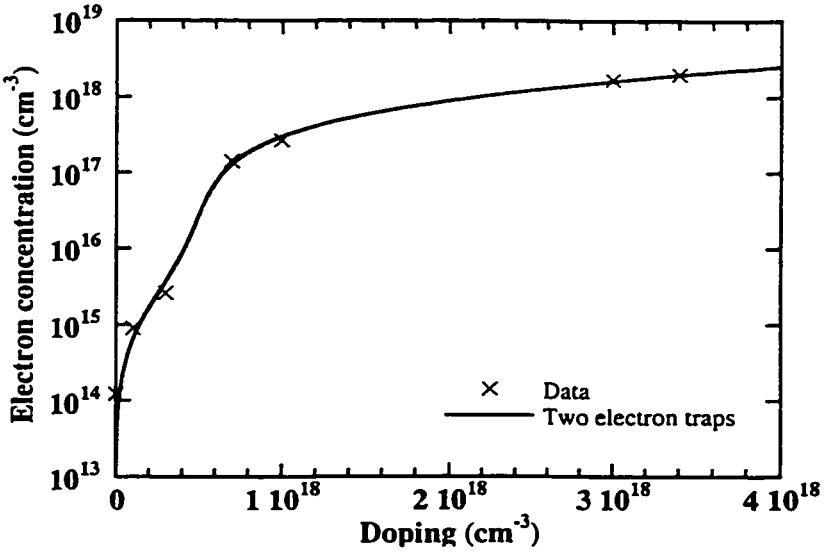

Figure 5.6: Calculated carrier concentrations for acceptor-like traps placed 0.68 eV ($5x10^{17}$ cm^{-3}) and 0.85 eV ($1x10^{18}$ cm^{-3}) above the valence band edge.

samples, plotted in this way, are illustrated in Figure 5.7. The Si-doped samples are represented on the positive x-axis and Be-doped samples on the negative x-axis. Thus, data lying on the negative x-axis above mid-gap ($E_V + 0.4$ eV) represent the n-type behaviour of the weakly Be-doped He-InGaAsP samples.

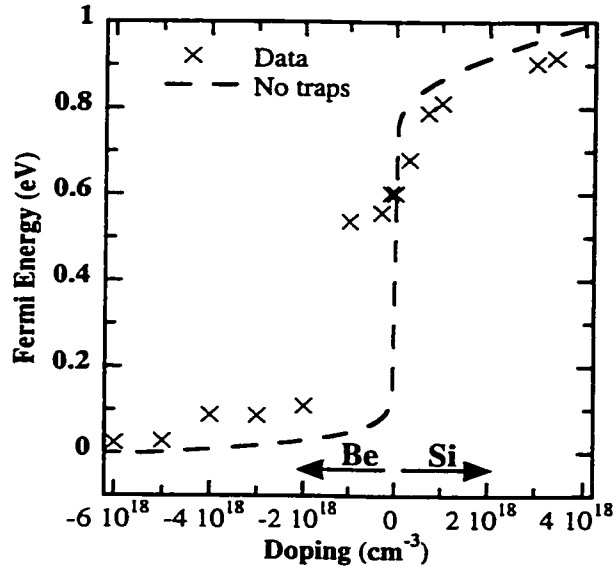

Figure 5.7: The He-InGaAsP Hall effect data, plotted as Fermi energy versus doping concentration, for all Be- and Si-doped samples. The Si-doped samples are represented on the positive x-axis, the Be-doped samples on the negative axis.

Retaining the two levels proposed above for the Si-doped samples, two more defect levels were added, as explained below, to model the behaviour observed for the Be-doped samples. By adding p-type dopants to a standard quaternary sample, the Fermi energy is pulled below the mid-gap energy. However, the He-InGaAsP samples remained n-type up to a Be doping level of $1x10^{18}$ cm^{-3}, suggesting that the Fermi level is controlled by a hole-trap above mid-gap. In Chapter 4, it was shown that a compensating donor-like defect must be present in these samples. From Figure 5.7, the experimental data show a rapid decrease in the Fermi energy once a Be-doping

concentration of $1x10^{18}$ cm^{-3} is exceeded, corresponding electrically to a change from n-type to p-type behaviour observed when sufficient Be is added to the system. This suggests an approximate donor-like defect concentration of $\sim 1x10^{18}$ cm^{-3}, sitting in the energy range 0.5 to 0.6 eV above the valence band. A good fit to the data yields a level at $E_{T3}=(E_V+0.55)$ eV, with a trap concentration of $1.2x10^{18}$ cm^{-3}. However, the presence of this trap does not explain the reduced carrier concentrations observed at the higher doping levels. To address this, another donor-like defect was included near the valence band edge, at an energy $E_{T4}=(E_V+0.08)$ eV and a concentration of $3x10^{18}$ cm^{-3}. Figure 5.8 illustrates the effect as each defect, with its associated concentration and energy level, is added to the model.

It can be seen that the acceptor-like defects, E_{T1} and E_{T2}, fit the data more closely than the donor-like levels, E_{T3} and E_{T4}. This may indicate that more donor-like defect levels are required in these energy ranges than are presently included in the model. It is quite possible that there are several closely-spaced defects and experimentally we see an average effect. The model gives only a semi-quantitative estimate of the trap energies and concentrations since several considerations were neglected. Firstly, the Hall effect data were not corrected for depletion effects at the surface and substrate-epilayer interfaces. Since no depletion effects were found for a sample doped with $3x10^{17}$ cm^{-3} Si, it was not possible to estimate the depletion widths for any doping concentration. This would cause greater error for the samples of low carrier concentration, since the depletion effects would be more pronounced. Secondly, at low carrier concentrations we are limited by the sensitivity of the Hall effect apparatus, which again would cause the greatest error in the weakly-doped samples. Thirdly, the model did not take into account the high doping effects discussed above and finally, the trap levels and concentrations chosen are somewhat subjective be-

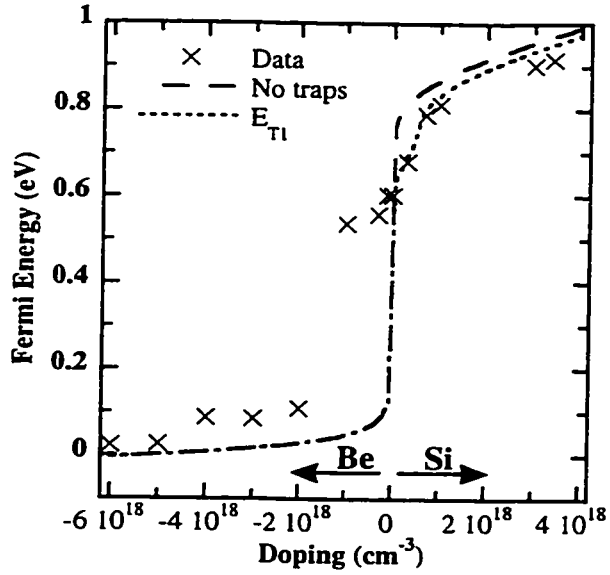

5a) Effect of including acceptor-like trap at Et1=0.68 eV, Nt1=5x10^{17} cm^{-3}.

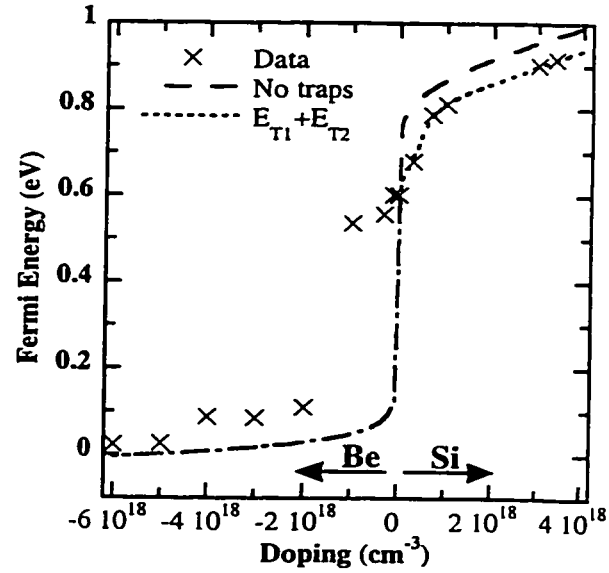

5b) As for (a) except additional acceptor-like trap at Et2=0.85 eV, Nt2=1x10^{18} cm^{-3}.

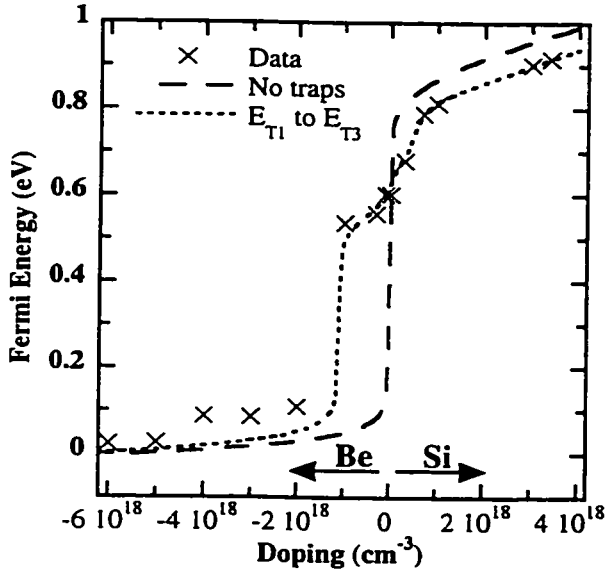

5c) As for (b) except additional donor-like trap at Et3=0.55 eV, Nt3=1.1x10^{18} cm^{-3}.

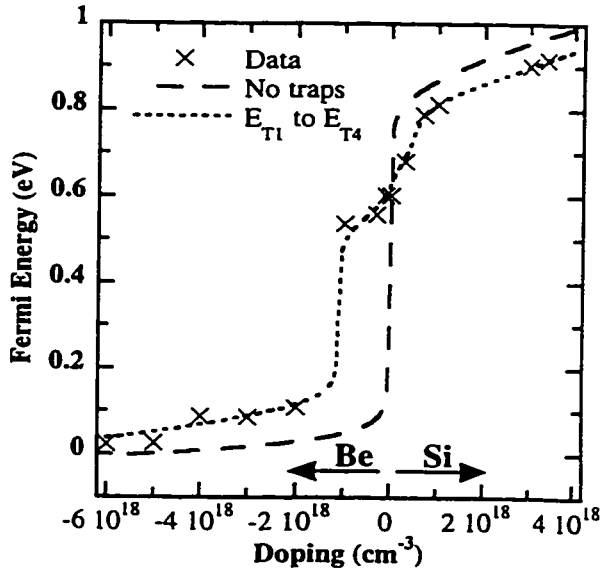

5d) As for (c) except additional donor-like trap at Et4=0.08 eV, Nt4=4x10^{18} cm^{-3}.

Figure 5.8: Effect of adding each trap on calculated Fermi energy.

cause the fit was optimized visually. However, despite these quantitative limitations, the model does indicate the need for two acceptor-like defects in the upper half of the bandgap, one of which lies at or above the conduction band edge to account for the low electron concentration at high silicon doping levels. Also, at least one deep donor-like trap, situated above mid-gap, is required to explain the n-type behaviour of the weakly Be-doped samples. Finally, the hole concentration does not recover as fully as expected at the highest Be doping concentrations and this implies that at least one donor-like defect, possibly a band of defects, is present near the valence band edge.

5.5.3 Annealing Studies

As described in Chapter 4, all samples were annealed at various temperatures in order to study the effect on the carrier concentrations. To model the effects of annealing on the defects present in the samples, we assumed that: i) the electrically-active defect concentration decreased with anneal, once a sufficient temperature was attained; and ii) the annealing process did not create new electrically-active defects. The experimental and model results are summarized in Figure 5.9. The experimentally determined Fermi energy and model best fits are plotted for anneal temperatures 550, 650 and 750°C. Figure 5.10 illustrates the changes to each of these levels with annealing.

We can see for the 550°C anneal that the concentration of donor-like defects at (E_V+0.55) eV has been reduced significantly, while the other defect concentrations are unchanged. The sample doped with 1x10^{18} cm^{-3} Be has become p-type, since the Fermi energy now lies below mid-gap in Figure 5.9. The effect of this anneal on the electron concentration of the Si-doped samples has been negligible; therefore, the 550°C plot lies on top of the as-grown plot over the entire Si-doping range. After

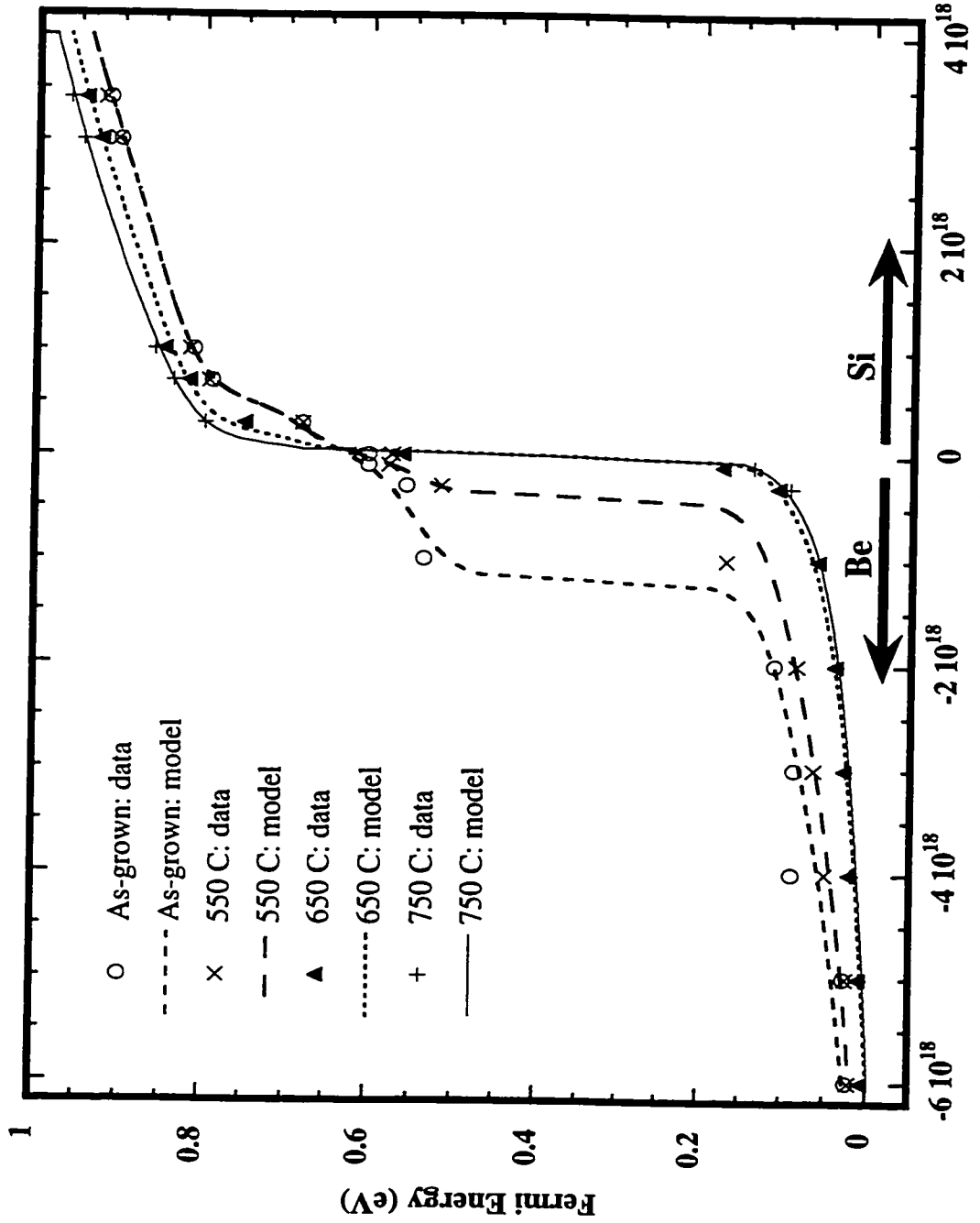

Figure 5.9: Effect of annealing on calculated Fermi energy.

Energy (eV)	As-grown (cm^{-3})	550°C (cm^{-3})	650°C (cm^{-3})	750°C (cm^{-3})	800°C (cm^{-3})	Defect Type
$E_{T1} = 0.68$	$5x10^{17}$	$5x10^{17}$	$2x10^{17}$	$1x10^{17}$	$5x10^{16}$	Acceptor-like
$E_{T2} = 0.85$	$1x10^{18}$	$1x10^{18}$	$6x10^{17}$	$2x10^{17}$	negligible	Acceptor-like
$E_{T3} = 0.55$	$1.2x10^{18}$	$4x10^{17}$	negligible	negligible	negligible	Donor-like
$E_{T4} = 0.08$	$3x10^{18}$	$3x10^{18}$	$8x10^{17}$	$5x10^{17}$	$5x10^{17}$	Donor-like

Table 5.1: Calculated trap energy levels and concentrations as a function of anneal temperature.

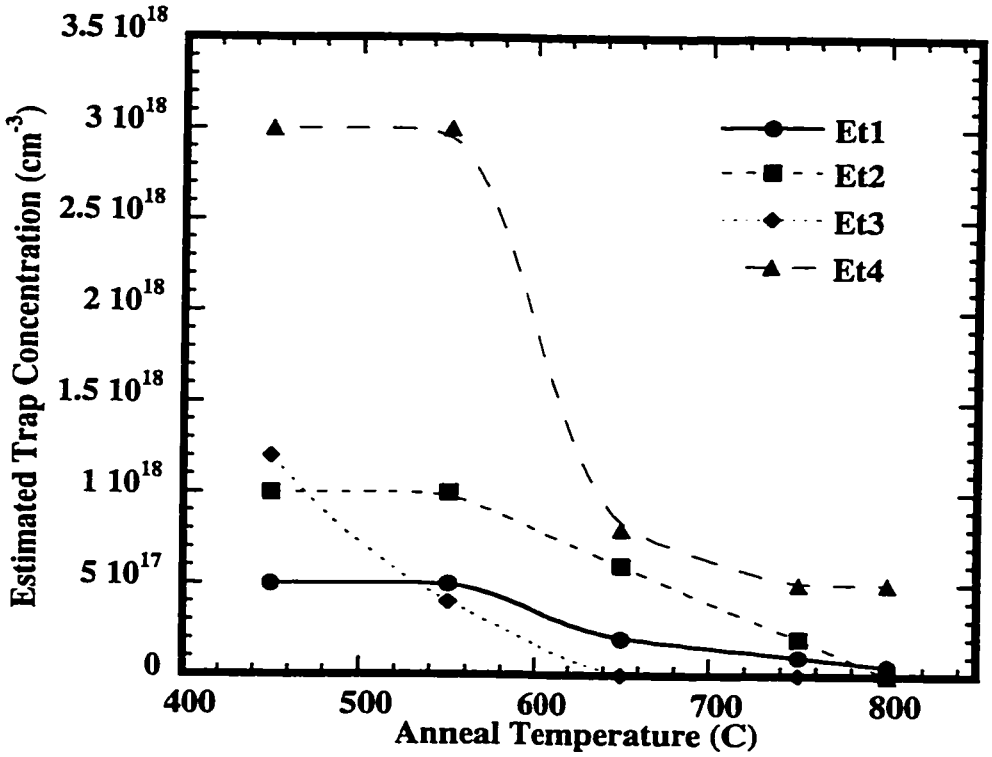

Figure 5.10: Effect of annealing on estimated trap concentrations.

the 650°C anneal, the donor level at 0.55 eV is essentially completely removed; and the samples doped with $1x10^{17}$ and $3x10^{17}$ cm^{-3} Be have become p-type. Also, the concentration of acceptor-like levels and the (E_V+0.08) eV donor level have decreased at this anneal temperature. Finally after anneal at 750°C, almost all defect levels have been removed and, except for some small differences at the lower doping levels, the samples appear similar to a standard quaternary material with few defects. Table 5.1 summarizes the proposed energy levels and the changes to defect concentration with annealing.

5.5.4 Variable-Temperature Hall Effect Measurements

Having obtained a model that described the room-temperature Hall effect measurements, it was possible to model the electrical effects of changing the temperature of a specific sample. As discussed in Section 2.3, the standard theory for analysis of temperature-dependent Hall effect measurements assumes that only one donor-like and one acceptor-type defect are present in the material. However, as we have seen previously, the model indicates that four defect levels may be present, along with the shallow dopant. Therefore, the most appropriate way to analyze the temperature-dependent electrical results was to compare them to simulations from the model. Figure 5.11 illustrates the simulation results for samples with various doping concentrations, along with the experimental results for a sample doped with $3x10^{17}$ cm^{-3} Be. A number of observations can be made. Firstly, the slope of the line depends strongly on the doping concentration and type, because we are measuring the Fermi energy, and this will be affected by more than one defect level at any given temperature. Strongly n-type samples gave shallow slopes of 0.030 to 0.15 eV, whereas weakly n-type samples (such as the test sample) gave slopes that "clustered" around the proposed defect level, E_{T1}, at 0.25 eV below the conduction bandedge.

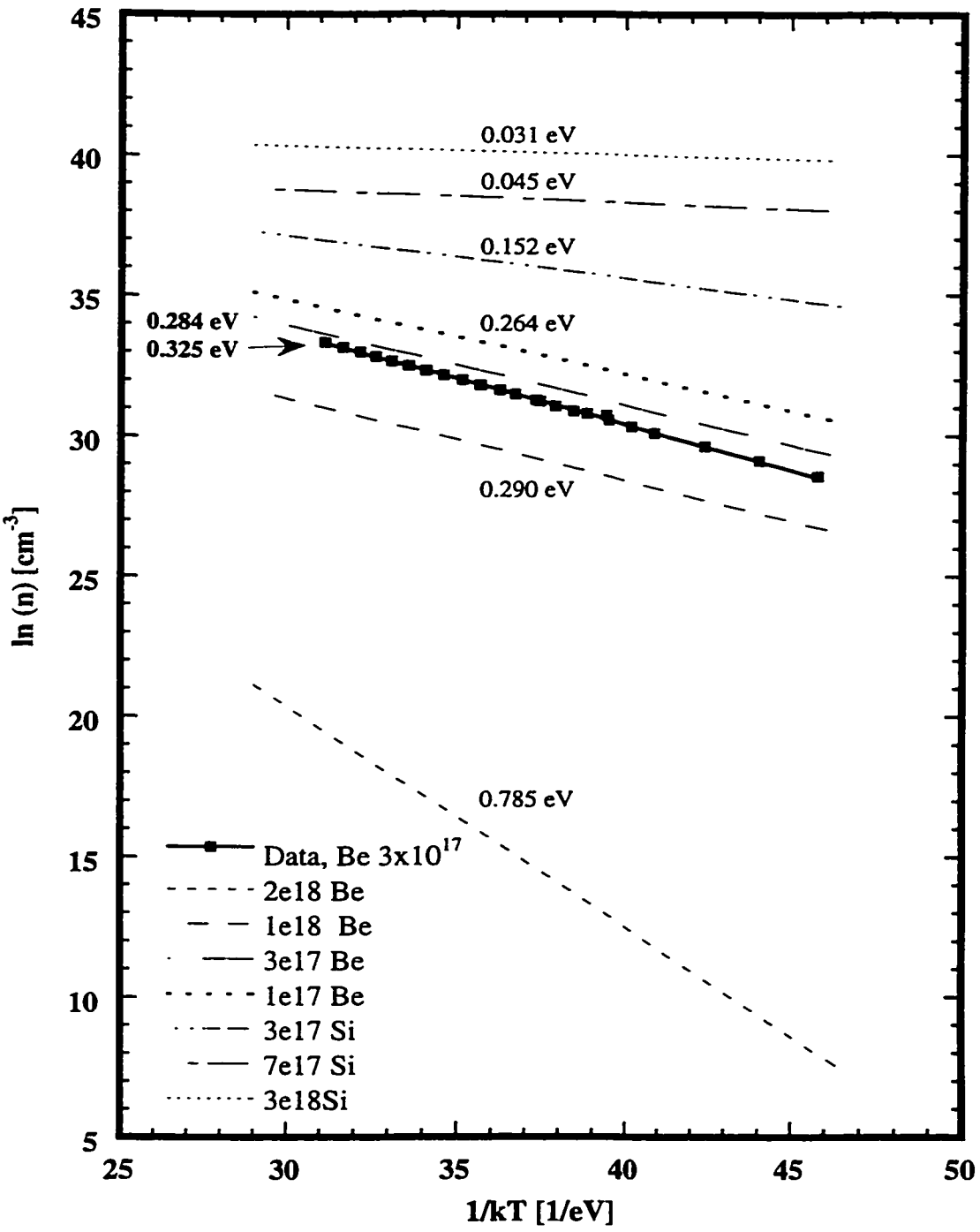

Figure 5.11: Model simulations of ln(n) versus 1/kT for a number of doping concentrations. Experimental data for Be-doped sample (3x10^{17} cm^{-3}) also shown for comparison.

The p-type Be-doped sample (2x10^{18} cm^{-3}) gave a slope of 0.785 eV, a value much lower in the bandgap than any of the other samples. Secondly, the experimental data for a Be-doped sample (3x10^{17} cm^{-3}) gave a slope of 0.325 eV below the conduction band, in reasonable agreement with the theoretical slope of 0.284 eV below the conduction for the same doping conditions. Thus, the model was able to adequately describe the effects of sample temperature on the electrical properties.

5.6 Summary Discussion for InGaAsP

Using this model, we can now explain more fully the behaviour of the He-plasma-assisted quaternary samples.

Electrical behaviour

The increase in resistivity of the undoped and weakly Be-doped samples on anneal at low temperature can be attributed to the fact that the deep donors (E_{T3}=E_V+0.55 eV) are removed at lower anneal temperatures than the shallow electron traps, E_{T1} and E_{T2}. The (E_V+0.55) eV donors decreased in concentration at 550°C versus 650°Cfor the acceptor-like levels, and this manifested itself as a decrease in the electron concentration. Once the electron traps, E_{T1} and E_{T2}, were removed, the n-type carrier concentration of the undoped and silicon-doped samples increased. The removal of the donor-like defects (hole traps) on anneal also caused the p-type character of the Be-doped samples to become apparent. Of course, when the Be concentration exceeded the (E_V+0.55) eV hole trap density, i.e. the Be concentration was 2x10^{18} cm^{-3} or higher, all the E_{T3} traps were empty, and the material was p-type even as-grown. The inclusion of both donor-like and acceptor-like flaws can explain both the resistivity as a function of doping as well as the resistivity as a function of annealing.

Positron data

For all samples that were n-type as-grown, whether undoped, Si-doped or weakly Be-doped, the positron results were similar in that we saw open volume defects, probably in the form of single and divacancies. On annealing at low temperatures, up to 650°C, the open volume defects appeared to increase in size for all these samples, regardless of doping. This coincided with a decrease in the electron concentration with increasing anneal temperature for the undoped and weakly Be-doped He-InGaAsP samples; the Si-doped samples, which exhibited much higher electron concentrations, showed an increase in carrier concentration. At the higher anneal temperatures, the S-parameter of the undoped and Si-doped samples saturated, indicating that the clusters had reached their maximum size. Interestingly, the presence of these clusters did not greatly inhibit the electrical behaviour of the samples, since, despite the increase in size of the clusters with anneal, the carrier concentration and mobility eventually approached those expected for standard samples. The weakly Be-doped sample, exhibited different behaviour on anneal; after the initial increase at low anneal temperatures, the S-parameter suddenly decreased in value at the higher anneal temperatures, suggesting that some of the defects were now positively-charged. The Be caused even more pronounced effects when present at a concentration of $3x10^{18}$ cm^{-3}; the S-parameter was no different from that of the standard sample, either as-grown or after anneal, indicating that in this sample, none of the defects were detectable. Given the model described above, we can now understand the behaviour of the Be-doped samples in terms of the donor-like defects. All samples contain both acceptor-like and donor-like defects, created during growth by the plasma particles. Acceptor-like defects are neutral when "empty" of an electron, and negatively-charged when "full". This means that any open volume defects that

are acceptor-like would always be apparent to the positron beam, regardless of the position of the Fermi energy. In contrast, donor-like defects are neutral when full and positively-charged when empty. As the samples were annealed, the Fermi level of the Be-doped samples decreased below the level of the donor-like defects detected by the positrons causing those donor-like defects to become positively charged. In so doing, they became undetectable to the positron beam. For the undoped and Si-doped samples, the Fermi energy always remained above mid-gap; hence the donors were always neutral and therefore detectable.

Photoluminescence behaviour

The fact that the as-grown samples emitted very little PL indicates that the fastest recombination processes are non-radiative. The PL intensity did not recover until anneal temperatures of 600°C or greater were used. This coincides electrically with the removal of the donor-like defects at E_{T3}=E_V+0.55 eV, suggesting that these defects are responsible for the non-radiative transitions. Beyond anneal temperatures of 600°C, PL transitions were observed in the range of 0.75 to 0.9 eV, all of which are at or below the bandgap energy for a sample at 16K. The above-described trap level model indicated that, after anneal at higher temperatures, the dominant traps are those donors that lie close to the valence band edge (within approximately 80 meV) and the acceptor-like level which lies 120 meV from the conduction band-edge. Thus it is possible that we are seeing transitions from the conduction band edge to these deep donor levels close to the valence band (0.8 to 0.9 eV PL) and from the electron trap, E_{T2}, to the valence band (approximately 0.75 eV or 120 meV below the conduction band edge). Also, as noted in Section 5.5, the models for the donor-like levels in the Be-doped samples were poorer fits to the data than for the acceptor-like levels in the Si-doped samples. It is quite possible that a number of levels are present

near the valence band edge which give rise to the broad bands in the 0.8 to 0.9 eV range of the PL spectra.

Pump-Probe Measurements

Studies undertaken at the University of Toronto [Qian et al. (1997)] indicated that the carrier lifetime in Be-doped samples became shorter with increased Be doping, as described in Section 1.3. This is consistent with the Fermi energy being pulled further towards the valence band-edge, thereby emptying more donor-like (fast) traps. Also, recently the same group performed dual-wavelength pump-probe measurements on both Be- and undoped samples [Qian et al. (1999)]. They reported that the undoped sample exhibited a considerably longer carrier lifetime when pumped below the conduction band-edge versus above-bandgap pumping. This also is consistent with the model developed above: there are fast traps which lie closer to the middle of the bandgap (E_{T3}) and slower, shallower traps closer to the band-edges. The same group also observed [Qian et al. (1997c)] that the carrier lifetime increased with annealing. Once again, this can be attributed to the removal of the fast "mid-gap" defects.

Chapter 6

Discussion and Future Work

6.1 Defects in III-V Semiconductors

In Chapter 5, a model was developed that proposed the presence of four traps in the He-InGaAsP material system: two electron traps at $E_V + 0.68$ and $E_V + 0.85$ eV and two hole traps at $E_V + 0.08$ and $E_V + 0.55$ eV. In this section, some of the III-V defects previously observed by other researchers in the field will be discussed, in an effort to identify some of the defects found in He-InGaAsP. Over the years, many defects have been studied, both experimentally and theoretically, in the III-V system. A selection of native defects for InGaAs(P), InP and GaAs from the vast literature on this subject [see, for example, the comprehensive reviews by Nauka (1993) and Anderson and Jiao (1991)] are described in the sections below, along with summary tables. However, the identification of a specific defect, particularly in the quaternary system, is difficult for a number of reasons. Firstly, even the relatively simple native point defects can take several forms: an atom of element x may be completely missing from the lattice, in which case there is a vacancy, denoted V_x; when an atom is situated on the wrong sublattice, e.g. an In atom on a P site, it is an antisite defect, denoted In_P; also, atoms may become situated between the substitutional lattice sites, in which case an interstitial is formed, e.g. P_i. Also, these defects may not be isolated,

but may form complexes with other defects or impurities in the lattice. Secondly, a defect at a known energy in a binary material, such as InP, will not necessarily occur at exactly the same energy in the quaternary system, although the defect may exhibit an energy level in the same range. For example, the energy levels associated with P vacancies and related complexes occur at $\sim (E_C - 0.44)$ eV in InP [Yamamoto et al. (1989)] and at $(E_C - 0.39)$ eV in $In_xGa_{1-x}As_yP_{1-y}$ ($0 \leq y \leq 0.41$) [Zhu et al. (1989)]. Thirdly, since defects can exhibit different charge states that may differ in energy by only small amounts, the assignment of detected defects is extremely difficult [Jaros (1980)]. In the Fermi-Dirac model used in Chapter 5, it was assumed that each defect behaved either as a neutral or singly-charged defect, whereas in fact, these levels may be due to multiply-charged states of a particular defect.

A number of parameters can be quoted for a given defect in a material system, such as its concentration, energy level in the bandgap and capture cross-section. For this work, the defect energy level is the most accessible value from the experimental measurements and therefore, will be quoted in the discussion below.

6.1.1 InGaAsP Defects

The most relevant defects for this work are those observed in InGaAsP, summarized in Table 6.1. However, although a number of defects have been described in terms of energy levels and capture cross-sections, very few have been attributed a specific origin. Sasai et al. (1979) identified three electron traps in $In_{0.85}Ga_{0.15}As_{0.39}P_{0.61}$ (E_g= 1.063 eV at room temperature) by DLTS at (E_C−0.27) eV, (E_C−0.30) eV and (E_C−0.51) eV, but no origin was suggested for the traps. Zhu et al. (1989) studied $In_xGa_{1-x}As_yP_{1-y}$ of various compositions ($0 \leq y \leq 0.41$) with DLTS. Two electron traps were observed at (E_C−0.39) eV and (E_C−0.61) eV; the first was attributed to the P vacancy, the second (observed when there was lattice mis-match) was attributed to

an anion vacancy and/or a complex involving an impurity. Bhattacharya et al. (1979, 1981) found a number of electron and hole traps in various compositions of quaternary materials with band-gap energies from 0.95 to 1.19 eV, although many were unassigned or attributed to impurities. The most significant according to the authors was the electron trap at (E_C−0.81) eV which exhibited very similar behaviour to a trap at (E_C−0.83) eV in GaAs (possibly related to the Ga vacancy). A possible native defect electron trap was found at (E_C−0.35) eV in p-InGaAs. Also, the authors claim to have identified the first hole trap in the quaternary system at (E_V+0.26) eV. This trap appeared for both LPE and VPE material, suggesting that it is a native defect, but no origin was suggested. Pelloie et al. (1986) studied p-$In_{0.53}Ga_{0.47}As$ and p-$In_{0.72}Ga_{0.28}As_{0.6}P_{0.4}$. The quaternary material yielded three hole traps at (E_V+0.25), (E_V+0.40) and (E_V+0.69) eV. Interestingly, the 0.25 eV trap exhibited very similar characteristics to the (E_V+0.22) eV hole trap found in InP in the same work and which was tentatively attributed to an impurity-V_P complex. The other two traps were not identified. The ternary exhibited a hole trap at (E_V+0.08) eV of very high

Defect	**Stated Defect Type**	**Energy (eV)**	**Researcher(s)**
Unknown	Electron	E_C−0.27 E_C−0.30 E_C−0.55	Sasai et al. (1979)
V_P	Electron	E_C−0.39	Zhu et al. (1989)
V_{anion} or imp. complex		E_C−0.61	Zhu et al. (1989)
V_{Ga} related?	Electron	E_C−0.82	Bhattacharya et al. (1981)
Native defect?	Hole	E_V+0.26	Bhattacharya et al. (1981)
p-InGaAs native defect	Electron	E_C−0.35	Bhattacharya et al. (1981)
Impurity-V_P complex	Hole	E_V+0.25	Pelloie et al. (1986)
Unknown	Hole	E_V+0.40 E_V+0.69	Pelloie et al. (1986)

Table 6.1: Experimentally determined defects in InGaAsP

concentration and it was suggested that it was related to the p-type Zn dopant.

It can be seen that the above offers no obvious identification for any of the native defects postulated in this work. Electron traps were identified by Sasai et al. (1979) in the energy range of $E_C - 0.27$ eV, but the specific cause was not suggested. Further insight into the He-InGaAsP system can be gained from the defects found in InP and GaAs, discussed below.

6.1.2 InP Defects

A large number of native point defects have been found in InP; electron traps have ranged in energy from $(E_C - 0.11)$ eV to $(E_C - 0.78)$ eV [Anderson and Jiao, (1991)]. The defects that are most relevant to this work are summarized in Table 6.2.

The indium vacancy, an acceptor-like defect, was observed at E_V+(0.18 ± 0.02) eV [Yu et al. (1992)]. A number of researchers have identified the phosphorus vacancy as an electron trap, with energy levels of (E_C−0.43) eV (complexed with

Defect Name	Stated Defect Type	Energy level (eV)	Researcher(s)
V_{In}	Acceptor	E_V+(0.18 ± 0.02)	Yu et al. (1992)
V_P	Donor		Liang et al. (1992)
	Electron trap	E_C−0.44	Yamamoto et al. (1989)
V_P:Fe complex		E_C−0.43	Iliadis et al. (1989)
In_i	Donor		Liang et al. (1992)
P_i	Acceptor		Liang et al. (1992)
In_P	Acceptor		Liang et al. (1992)
P_{In}	Donor	E_C−(0.33 ± 0.03)	Yu et al. (1992)
		E_C−0.22	Dreszer et al. (1993a)
		E_C+0.11	
		E_C−0.23	Dreszer et al. (1993b)
		E_C+0.12	
		E_C−0.25 (DLTS)	

Table 6.2: Experimentally determined defects in InP

Fe) [Iliadis et al. (1989)] and (E_C−0.44) eV [Yamamoto et al. (1989)]. The indium antisite defect, In_P, has been postulated to be an acceptor-like defect [Liang et al. (1992)]. However, as of 1993, this defect had not been observed experimentally [Seitsonen (1994)]. The phosphorus antisite, P_{In}, however, has been observed by a number of researchers. Yu et al. (1992) found P_{In} to be a deep donor sitting at an energy of (0.33 ± 0.03) eV below the conduction band. Dreszer et al. (1993a, b) used a number of techniques to estimate the energies of the P_{In} to be (E_C+0.11) eV and (E_C−0.22) eV (from Hall effect measurements), (E_C+0.12) eV and (E_C−0.23) eV (from high-pressure Hall effect measurements) and (E_C−0.25) eV (from DLTS). Two groups identified defects at (E_C−0.49) eV [McAfee et al. (1981)] and (E_C−0.53) eV [Ogura et al. (1983)] as V_{In}, P_i or P_{In}. Liang et al. (1992) proposed that the phosphorus interstitial would expected to be acceptor-like, while the indium interstitial would be donor-like. However, no energy levels were quoted for these defects.

Theoretical calculations have also been performed for the In and P vacancies in InP [Alatalo et al. (1993), Seitsonen et al. (1994)]. Their results are summarized in Table 6.3. All the ionization levels for the In vacancy were found to lie within 0.23 eV of the valence bandedge. The calculations showed that the P vacancy is negative when the Fermi energy is in the upper part of the bandgap; only two states were predicted at E_V + 0.99 and E_V + 1.18 eV. To summarize, the most relevant defects for this work, in terms of their energy level in the bandgap, may be the indium vacancy and the phosphorus antisite. The indium vacancy is believed to sit close to the valence bandedge and, according to theory, can assume a number of charge states; for example, the transition from neutral to positively charged (donor-like behaviour) occurs at (E_V + 0.1) eV and this may correspond to the level E_{T4} from the Fermi-Dirac model that sits at (E_V+0.08) eV. However, the indium atom is

much more massive than the phosphorus atom, thus is less likely to be removed from the lattice by a collision event. The phosphorus antisite exhibited a donor-like level of approximately ($E_C - 0.25$) eV [Dreszer et al. (1993b)], which may correspond to E_{T3}. This defect exhibited a second level above the conduction band edge at ($E_C + 0.11$) eV. It is possible that trap levels E_{T2} and E_{T3} could both be explained in terms of the phosphorus antisite defect.

6.1.3 GaAs Defects

The other binary of potential interest for this work is GaAs; the defects relevant to this work are summarized in Table 6.4. The gallium vacancy, an acceptor-like

Vacancy	Ionization level	Energy level w.r.t. VB (eV)
V_{In}	(+/2+)	−0.04
	(0/+)	0.10
	(−/0)	0.13
	(2−/−)	0.18
	(3−/2−)	0.23
V_P	(0/+)	unstable
	(−/+)	0.99
	(3−/−)	1.18

Table 6.3: Theoretically calculated defects in InP (after Alatalo et al. (1993)).

Defect Name	Stated Defect Type	Energy level (eV)	Researcher(s)
V_{Ga}	-ve when $E_F \sim E_i$	Not given	Corbel et al. (1997)
	Acceptor-like	$E_V + 0.3$	Kaminska et al. (1989)
	Electron trap	$E_C - 0.82$	Bhattacharya et al. (1981)
V_{As}	Amphoteric	E_C−(0.03 to 0.05)	Corbel et al. (1997)
		E_C−0.14	
V_{As}−As pair?		E_C−0.04	Auret et al. (1998)
		E_C−0.14	
		E_C−0.045	Ziebro et al. (1992)
		E_C−0.15	

Table 6.4: Experimentally determined defects in GaAs

defect [Lee et al. (1990)] was found at an energy level of $E_V + 0.3$ [Kaminska et al. (1989)]. Bhattacharya et al. (1981) tentatively attributed an electron trap at $(E_C - 0.82)$ eV to the Ga vacancy. Using positron annihilation lifetime studies, Corbel et al. (1997) identified both the Ga and As vacancies; they found V_{Ga} to be negatively charged when the Fermi energy was at mid-gap and V_{As} was found to be amphoteric, depending on the position of the Fermi energy. Two energy levels were identified for the arsenic vacancies: the vacancy is positive when the Fermi energy lies below $(E_C - 140)$ meV and negative when the Fermi lies above $(E_C - [30 \text{ to } 50])$ meV. Auret et al. (1998) investigated the effect of processing GaAs using rf He-plasma dry etching. They found a number of electron traps, two of which were situated 0.04 and 0.14 eV below the conduction band. These levels were believed to be two charge states of the V_{As}-As pair [Ziebro et al. (1992)]. The gallium vacancy appears to lie too deep in the gap to be relevant to this work. The arsenic vacancy is a possible candidate for trap E_{T1}, which sits at an energy of 120 meV below the conduction bandedge, although the situation is complicated by the different charge states manifested by this defect. Given the experimental and calculation errors associated with the highly-doped samples, it is possible that the second V_{As}-As defect corresponds to level E_{T2}, which is believed to lie at an energy ~ 0.8 eV.

In summary, a large number of defects have been observed in this material system. It seems possible that the electron-trap defects are related to the arsenic vacancy, which tends to form levels in the upper half of the bandgap in gallium arsenide. The closest level for the donor level in the upper half of the bandgap was found to be the phosphorus antisite, but the phosphorus vacancy is also a likely candidate. The lower donor level that sits just above the valence may be a defect complex involving the Be dopant or possibly, one of the charge states of the indium

vacancy.

6.2 Future Work

From the above discussion, it is clear that further work is required to identify these defects and confirm the energy levels associated with them. A number of possible material characterization techniques are discussed below. Also, the unusual properties of the He-plasma material and the simplicity of the growth technique make this material an excellent candidate for high-speed telecommunications applications. This section concludes with a brief discussion of potential devices fabricated with He-InGaAsP.

6.2.1 Material Characterization

Deep Level Transient Spectroscopy

DLTS allows the determination of the concentrations, activation energies and trap cross-sections of defects, although it does not provide structural information. Also, this technique can distinguish between electron and hole traps. DLTS utilizes the changes in the space charge of a depleted region of a device (such as a metal-insulator-semiconductor (MIS) structure or p-n junction) after a transient bias is applied [Bourgoin and Lannoo, (1983)]. The width of the depletion layer is a function of the number of defects that are filled with electrons. The change in width of this region manifests itself as a change in the capacitance of the junction. The trap parameters are found by studying the emission rates from the traps after the fill pulse. However, in order for this technique to give reliable results, the trap concentration must be small compared to the doping level.

MIS structures have been fabricated previously from the He-plasma grown

materials, but the devices failed because the contact was not Schottky-like. Hence, for future work, a p-n junction approach is suggested. For example, McKeever et al. (1990) used n^+p mesa diodes to study defect levels in irradiated p-InP. The p-type layer of interest was grown on a heavily p-doped substrate with a p^+ buffer layer. A thin n^+ layer was then grown on top of all the p-doped layers and alloyed contacts were applied to the substrate and the n^+ layer. Electron and hole traps were clearly distinguishable using this technique and it might prove valuable for both the He-InP and He-InGaAsP materials.

Electron Paramagnetic Resonance

By placing a sample in a magnetic field, the degeneracy of the electron ground states is lifted and a number of energy levels arise. Transitions by unpaired electrons can be induced between these levels if the sample is in resonance with an applied electromagnetic field. Semiconductors are diamagnetic, so would not exhibit these transitions, but defects are often filled with one unpaired electron or hole and, in this case, paramagnetism could possibly be observed [Bourgoin and Lannoo, (1983)].

This technique has been applied successfully to LTG GaAs, in which arsenic antisites (As^0_{Ga} and As^+_{Ga}) were studied. However, when this technique was applied to LTG InP, no paramagnetic defects were found; the Fermi level was pinned by shallow donors in the upper half of the bandgap, so the phosphorus antisite was neutral and diamagnetic [von Bardeleben et al. (1992)]. Despite its usefulness in the study of defects, this technique is difficult to apply to compound semiconductors because it requires weak hyperfine interaction with nuclear spins in order to produce sufficiently narrow resonance lines. In addition, for epitaxial layers, care must be taken to distinguish between the signals from the substrate and the epilayer, which is not always straightforward [von Bardeleben et al. (1992)]. This technique may

prove useful for studying antisite defects in He-InP, but would be extremely difficult to apply to the He-quaternary samples.

Other Techniques

A number of more exotic, and less common, techniques have been used to characterize defects in epitaxial semiconductor layers. Liu et al. (1994) used near-infrared absorption (NIRA) and magnetic circular dichroism of absorption (MCDA) to determine the density of neutral (As^0_{Ga}) and ionized (As^+_{Ga}) arsenic antisites in LTG GaAs. Feenstra et al. (1993) were able to observe arsenic antisites in LTG GaAs using scanning tunneling microscopy (STM). They identified a band of donor-like defect states near E_V+0.5 eV and, by studying the images of the defect, were able to determine that the structure was "consistent with an isolated arsenic antisite (As on Ga) in a tetrahedral environment". This technique may be valuable in the study of any phosphorus antisite defects in the He-plasma-assisted materials.

6.2.2 Device Applications

Recently, the quaternary material was fabricated into a simple photoconductive optical detector [Kang et al. (1999)]. A fast-response device of this type requires a material with a fast optical response time and a high carrier mobility [Smith et al. (1989)], both of which are exhibited by He-InGaAsP. Kang et al. fabricated metal-semiconductor-metal (MSM) devices with 2 μm thick layers of He-InGaAsP (with a room-temperature bandgap wavelength of 1.583 μm) grown on SI InP. The Ti-Au electrodes were 22 μm wide and spaced 20 μm apart. The low responsivity of the detectors (10.8 mA/W at 33 GHz, 20 V bias, 0.5 mW total optical power) was attributed to the non-ideal structure.

In collaboration with the University of Toronto, efforts are currently under-

way at McMaster University to fabricate the first all-optical switch with the He-InGaAsP material, based on the asymmetric Fabry-Perot device (AFP) [Loka and Smith (1998)]. The AFP is comprised of an epitaxial layer of fast-response semiconductor material (in this case, He-InGaAsP) grown on a substrate with a high reflectivity mirror on the back surface and a low reflectivity mirror on the top surface. The thickness of the epitaxial layer is chosen such that light entering the device at the top surface and reflected from the back mirror is completely cancelled by light from the front surface, thus providing the "off" state. To switch the device "on", a high intensity control pulse is used to change the refractive index of the epitaxial layer, thereby inhibiting the destructive interference. For this device to operate successfully in a fast-response environment, the material must exhibit fast response times and large optically-induced refractive index changes, both of which have been observed for He-InGaAsP. This type of device has been demonstrated by Loka and Smith (1998) with LTG GaAs. However, using He-InGaAsP would allow the device wavelength to be tailored to a specific application.

6.3 Conclusion

Both InP and InGaAsP grown by He-plasma-assisted gas source molecular beam epitaxy exhibit unusual properties, which we believe are caused by the impact of the plasma particles during growth. This work was undertaken to better understand the underlying mechanisms of the quaternary material, since it may be technologically important for the telecommunications industry.

The initial studies focused on the binary, He-InP. Electrical measurements were performed using the standard room-temperature Hall effect technique in addition to n-i-n resistor studies. The as-grown material was weakly n-type, with a

carrier concentration of $6x10^{11}$ cm^{-3}, corresponding to a resistivity, $\rho > 10^5$ Ω-cm. This reduction from the standard carrier concentration ($\sim 10^{15}$ cm^{-3}) indicated the presence of electron traps in the system. On anneal, the electron concentration decreased, leading to a further increase in the resistivity. When Be was added to the material at concentrations of $3x10^{17}-1x10^{18}$ cm^{-3}, the sample remained n-type but the carrier concentration decreased, suggesting that either the Be was passivated or there were donor-like defects compensating the dopant. One common impurity in gas source MBE chambers is hydrogen, which arises from the dissociation of the group V hydride sources. Hydrogen is known to passivate acceptor-like dopants in InP. SIMS analysis of samples grown in the presence of deuterium gas indicated that there was sufficient deuterium present to passivate the Be in the as-grown samples, but the relationship between deuterium concentration and Be doping concentration was weak. After anneal at 600°C, the hydrogen had been completely removed, but the sample still exhibited n-type behaviour. Therefore, it is likely that the Be was compensated by a donor-like defect. Positron annihilation spectroscopy confirmed that defects were present in all the as-grown He-InP samples, both Be-doped and undoped, probably in the form of single and divacancies. To detect vacancies with this technique, the defects must be negatively-charged or neutral, since positively-charged defects are inefficient positron trapping centres. On anneal, these defects seemed to enlarge, most likely due to the diffusion and clustering of the smaller, mobile vacancies. However, the behaviour of the undoped and Be-doped samples differed when high anneal temperatures were used. The Be-doped sample showed a sudden decrease in the positron S-parameter, which we believe is due to a change in charge state of the defect from neutral or negative to positive. This may confirm that a donor-like defect was present, which underwent a change in charge state when the Fermi energy was pulled below

the level of the defect.

Subsequent studies concentrated on the quaternary material. He-InGaAsP was easier to study electrically, since it did not exhibit such high resistivity values. This allowed a comprehensive study of the material under various doping and rapid thermal anneal conditions. The quaternary exhibited similar trends in behaviour to the binary: the resistivity increased with anneal and Be-doping (up to a certain point) and open volume defects were observed with positron annihilation spectroscopy. The positron studies indicated that the Be-doped samples behaved differently to the undoped samples: the weakly Be-doped sample (initially n-type as-grown) showed an increase in the S-parameter for low temperature anneals and a subsequent decrease at higher anneal temperatures; the more strongly Be-doped sample (p-type as-grown) never exhibited an S-parameter value higher than that for the standard Be-doped sample, i.e. the defects were completely "masked" when the sample was p-type. All samples that exhibited a high S parameter as-grown, showed an increase in the S parameter on anneal, implying that larger defect clusters were being formed. The Hall effect measurements indicated that the undoped samples were weakly n-type and the addition of $<2\text{x}10^{18}$ cm^{-3} Be caused the resistivity to increase, i.e. the samples remained n-type but the electron concentration decreased with increased Be doping. Beyond a Be-doping concentration of $2\text{x}10^{18}$ cm^{-3}, the samples were p-type, although the hole concentration was much lower than that expected for standard Be-doped InGaAsP samples. This electrical behaviour indicated the presence of compensating donors with a concentration of $1\text{x}10^{18}$ to $2\text{x}10^{18}$ cm^{-3}. The silicon-doped samples were all weakly n-type, but the electron concentration was low compared to standard samples, once again suggesting the presence of electron traps. After anneal at 800°C, the Si-doped samples exhibited the electron concentrations expected for standard

samples, i.e. all electron traps had been removed. The n-type, weakly Be-doped samples initially became more resistive on anneal at low temperatures, but then reverted to p-type behaviour. Photoluminescence studies revealed that undoped, Si-doped and Be-doped samples emitted no detectable luminescence in the as-grown state. After anneal at temperatures >600°C however, PL became observable, although in all cases the spectra contained broad peaks at energies lower than the bandgap energy. This suggests that there are deep, non-radiative traps in the as-grown samples, which are removed upon anneal, probably leaving shallower, radiative states.

As a result of the room-temperature He-InGaAsP Hall effect studies, a model was developed based on Fermi-Dirac statistics that allowed the determination of four trap levels and their concentrations. Two electron traps and two hole traps were found at energy levels of $E_V + 0.85$ eV ($1\text{x}10^{18}$ cm^{-3}), $E_V + 0.68$ eV ($5\text{x}10^{17}$ cm^{-3}), $E_V + 0.55$ eV ($1.2\text{x}10^{18}$ cm^{-3}) and $E_V + 0.08$ eV ($3\text{x}10^{18}$ cm^{-3}). These values give only an estimate of the defect energy levels and concentrations; a number of assumptions were made, especially for the highly-doped samples, so the model can be considered semi-quantitative only. The hole traps (donor-like defects) nearest the middle of the bandgap are removed at the lower anneal temperatures, thereby explaining why the electron concentration decreases with gentle anneal. The electron traps are removed at higher anneal temperatures, so beyond a certain anneal temperature, the electron concentration of the undoped and Si-doped samples increased. A number of possible defects could be responsible for the material characteristics; the positron annihilation studies indicated that a donor-like vacancy defect is present, possibly in the form of As or P vacancies. Also, the P_{In} antisite may be present, if an indium atom were dislodged from the growth surface and the vacancy subsequently filled a P atom. The hole-trap lying close to the valence band edge may involve the Be dopant. Of course,

a number of other defects, such as As_{In} or P_{Ga} may also be present, but information regarding these defects and their complexes is more difficult to find.

In conclusion, He-InP and He-InGaAsP are complex materials with a great deal of potential for future applications. The objective of this study, to gain a better understanding of the material characteristics and underlying mechanisms, has been realized by extensive experimental work and the development of a plausible model. Based on this model, future devices can be designed that fully utilize the unusual properties of InGaAsP grown by He-plasma-assisted gas source MBE.

Appendix A

Material Parameters

The wavelength (in μm) and bandgap energy (in eV) of a semiconductor are related as follows:

$$E_0 = \frac{1.24}{\lambda} \quad \text{(eV)} \tag{A.1}$$

For a quaternary sample, the bandgap wavelength corresponding to a material of a given composition, $In_{1-x}Ga_xAs_yP_{1-y}$ can be found from the mole fraction of arsenic, as determined experimentally by Nahory et al. (1978):

$$E_0(y) = 1.35 - 0.72y + 0.12y^2 \tag{A.2}$$

For a quaternary layer that is lattice matched to the InP substrate (all the samples in this study), the relation between x and y is:

$$x \simeq \frac{0.1894y}{0.4184 - 0.013y} (0 \leq y \leq 1) \tag{A.3}$$

A quaternary material parameter, P, such as the density or electron effective mass, can be found from the parameters for the binary compounds by using Vegard's law [Adachi, (1982)]:

$$\begin{aligned} P_{In_{1-x}Ga_xAs_yP_{1-y}} &= (1-x)yP_{InAs} + (1-x)(1-y)P_{InP} \\ &+ xyP_{GaAs} + x(1-y)P_{GaP} \end{aligned} \tag{A.4}$$

The binary parameters used to calculate the quaternary values using Vegard's law are summarized in Table A.1. Table A.2 summarizes the room-temperature bandgap energy, wavelength and density for each of the materials used in this work.

Parameter	InP	InAs	GaAs	GaP
m_e/m_0	0.079	0.023	0.067	0.130
m_{hh}/m_0	0.606	0.400	0.341	0.670
m_{lh}/m_0	0.121	0.027	0.094	0.170
ρ	4.787	5.667	5.307	4.13

Table A.1: Binary parameters used to calculate quaternary values used in this work [Adachi, (1982)].

Composition	Wavelength (μm)	Energy (eV)	Density (g/cm^3)
InP	0.919	1.35	4.787
$In_{0.61}Ga_{0.39}As_{0.85}P_{0.15}$	1.50	0.827	
$In_{0.60}Ga_{0.40}As_{0.87}P_{0.13}$	1.52	0.816	5.39
$In_{0.58}Ga_{0.42}As_{0.90}P_{0.10}$	1.55	0.800	5.41

Table A.2: Parameters for materials studied in this work.

References

S. Adachi, Journal of Applied Physics **53** (12), 8775 (1982)

M. Alatalo, R.M. Nieminen, M.J. Puska, A.P. Seitsonen and R. Virkkunen, Physical Review **B47**, 6381 (1993)

W.A. Anderson and K.L. Jiao, *Indium Phosphide and Related Materials: Processing, Technology, and Devices*, (Editor: A. Katz), (Artech House, 1991), Chapter 3

N. Atique, E.S. Harmon, J.C.P. Chang, J.M. Woodall and M.R. Melloch, Journal of Applied Physics **77**, 1471 (1995)

F.D. Auret, W.E. Meyer, P.N.K. Deenapanray, S.A. Goodman, G. Myburg, M. Murtagh, S.-R. Ye and G.M. Crean, Journal of Applied Physics **84** (4), 1973 (1998)

H.J. von Bardeleben, Y.Q. Jia, J.P. Hirtz, J.C. Garcia, M.O. Manasreh, C.E. Stultz and K.R. Evans, Materials Research Society Symposium Proceedings **241**, 69 (1992)

S.D. Benjamin, A. Othonos and P.W.E. Smith, Electronics Letters **30**, 1704 (1994)

P.B. Bhattacharya, J.W. Ku, S.J.T. Owen, S.-H. Chiao and R. Yeats, Electronics Letters **15** (23), 753, (1979)

P.B. Bhattacharya, J.W. Ku, S.J.T. Owen, G.H. Olsen and S.-H. Chiao, IEEE Journal of Quantum Electronics **QE-17** (2), 150, (1981)

J.S. Blakemore, *Semiconductor Statistics*, International Series of Monographs on Semiconductors (Editor: H.K. Henisch), Vol. 3, (Pergamon Press, 1962)

J.S. Blakemore, Solid State Electronics **25**, 1067, (1982)

D.E. Bliss, W. Waluciewicz, K.T. Chan, J.W. Ager III, S. Tanigawa and E.E. Haller, Materials Research Society Symposium Proceedings **241**, 93 (1992)

D.E. Bliss, W. Walukiewicz, J.W. Ager, E.E. Haller, K.T. Chan and S. Tanigawa, Journal of Applied Physics **71** (4), 1699 (1992)

J. Bourgoin and M. Lannoo, *Point Defects in Semiconductors II: Experimental Aspects*, Springer Series in Solid-State Sciences (Editor: M. Cardona), Vol. 35, (Springer-Verlag, 1983)

M. Bugajski and W. Lewandowski, Journal of Applied Physics **57** (2), 521 (1985)

H.C. Casey and F. Stern, Journal of Applied Physics **47** (2), 631 (1976)

Z.Q. Chen, X.W. Hu, S.J. Wang and S.Q. Li, Solid State Communications **97** (11), 951 (1996)

A.Y. Cho and J.R. Arthur, Progress in Solid-State Chemistry **10** (3), 157 (1975)

C. Corbel, C. LeBerre, K. Saarinen and P. Hautojarvi, Materials Science and Engineering **B44**, 173 (1997)

W.C. Dautremont-Smith, J. Lopata, S.J. Pearton, L.A. Koszi, M. Stavola and V. Swaminathan, Journal of Applied Physics **66** (5), 1993 (1989)

S.S. De, A.K. Ghosh, M. Bera, A.K. Hazra and J.C. Haldar, Canadian Journal of Physics **71**, 582 (1993)

P. Dreszer, W.M. Chen, K. Seendripu, J.A. Wolk, W. Walukiewicz, B.W. Liang, C.W. Tu and E.R. Weber, Physical Review **B47**, 4111 (1993)

P. Dreszer, W.M. Chen, D. Wasik, R. Leon, W. Walukiewicz, B.W. Liang, C.W. Tu and E.R. Weber, Journal of Electronic Materials **22** (12), 1487 (1993)

N.K. Dutta, Journal of Applied Physics **51** (2), 6095 (1980)

R.M. Feenstra, J.M. Woodall and G.D. Pettit, Physical Review Letters **71**, 1176 (1993)

M.Y. Frankel and T.F. Carruthers, Applied Physics Letters **64** (15), 1950 (1994)

S. Gupta, J.F. Whitaker and G.A. Mourou, IEEE Journal of Quantum Electronics **QE-28** (10), 2464 (1992)

E.S. Harmon, M.R. Melloch, J.M. Woodall, D.D. Nolte, N. Otsuka and C.L.Chang, Applied Physics Letters **63**, 2248 (1993)

E.S. Harmon, D.T. McInturff, M.R. Melloch and J.M. Woodall, Journal of Vacuum Science and Technology **B13**, 768 (1995)

J.R. Hayes, A.R. Adams and P.D. Greene, Electronics Letters **16** (8), 282 (1980)

Hewlett-Packard Operating Manual, Specifications for Model 4145B Parameter Analyzer

A.A. Iliadis, S.C. Laih and E.A. Martin, Applied Physics Letters **54** (15), 1436 (1989)

M. Jaros, Advances in Physics **29** (3), 409 (1980)

M. Kaminska, E.R. Weber, Z. Liliental-Weber, R. Leon and Z.U. Rek, Journal of Vacuum Science and Technology **B7** (4), 710 (1989)

J.U. Kang, M.Y. Frankel, R.D. Esman, D.A. Thompson and B.J. Robinson, Journal of Applied Physics **83**(6), 3423 (1998)

J.U. Kang, K. William, M.Y. Frankel, D.A. Thompson and B.J. Robinson, International Conference on Integrated Optics and Optical Fiber Communications, San Diego, 21-26 February 1999

Keithley Operating Manual, Specifications for Electrometer/Multimeter Model 619

M.A. Lampert and P. Mark, *Current Injection in Solids* (Academic Press, 1970)

D.W. Lawther and P.J. Simpson, Defect and Diffusion Forum **138/139**, 1 (1996)

D.S. Lee and J.G. Fossum, IEEE Transactions on Electron Devices **ED-30** (6), 626 (1983)

J.-L. Lee, A. Uedono, S. Tanigawa and J.Y. Lee, Journal of Applied Physics **67** (10), 6153 (1990)

R.F. Leheny, A.A. Ballman, J.C. DeWinter, R.E. Nahory and M.A. Pollack, Journal of Electronic Materials **9** (3), 561 (1980)

B.W. Liang, Y. He and C.W. Tu, Materials Research Society Symposium Proceedings **241**, 283 (1992)

X. Liu, A. Prasad, W.M. Chen, A. Kurpiewski, A. Stoschek, Z. Liliental-Weber and E.R. Weber, Applied Physics Letters **65**, 3002 (1994)

H.S. Loka and P.W.E. Smith, IEEE Photonics Technology Letters **10** (12), 1733 (1998)

D.C. Look, Journal of Applied Physics **70** (6), 3148 (1991)

D.C. Look, G.D. Robinson, J.R. Sizelove and C.E. Stutz, Journal of Electronic Materials **22** (12), 1425 (1993)

A.H. Marshak and C.M.V. Vliet, Proceedings of the IEEE **72**, 148 (1984)

S.R. McAfee, F. Capasso, D.V. Lang, A. Hutchison and W.A. Bonner, Journal of Applied Physics **52** (10), 6158 (1981)

S.W.S. McKeever, R.J. Walters, S.R. Messenger and G.P Summers, Journal of Applied Physics **69** (3), 1435 (1990)

D. McMorrow, T.R. Weatherford, W.R. Curtice, A.R. Knudson, S. Buchner, J.S. Melinger, L.H. Tran and A.B. Campbell, IEEE Transactions on Nuclear Science **42** (6), 1837 (1995)

H.P. Meier, M. Kamp and S. Strit, Microelectronics Journal **25**, 609 (1994)

M.R. Melloch, D.D. Nolte, J.M. Woodall, J.C.P. Chang, D.B. Janes and E.S. Harmon, Critical Reviews in Solid State and Materials Science **21**(3), 189 (1996)

D.B. Mitchell, Ph.D. thesis, (McMaster University, 1995)

D.B. Mitchell, B.J. Robinson, D.A. Thompson, L. Qian, S.D. Benjamin and P.W.E. Smith, Applied Physics Letters **69** (4), 509 (1996)

R.E. Nahory, M.A. Pollack, W.D. Johnston, Jr. and R.L. Barns, Applied Physics Letters **33**, 659 (1978)

K.W. Nauka, *Imperfections in III-V Materials*, Semiconductors and Semimetals (Treatise Editors: R.K. Willardson, A.C. Beer and E.R. Weber), Vol 38 (Volume editor: E.R. Weber), (Academic Press, 1993), Chapter 8

M. Ogura, M. Mizuta, N. Hase and H. Kukimoto, Japanese Journal of Applied Physics **23**, 79 (1983)

S. O'Hagan and M. Missous, Journal of Applied Physics **75**, 7835 (1994)

M.B. Panish, Prog. Crystal Growth and Charact. **12**, 1 (1986)

M.B. Panish and H. Temkin, Annual Review of Materials Science **19**, 209 (1989)

L.J. van der Pauw, Philips Research Reports **13**, 1 (1958)

J.L. Pelloie, G. Guillot, A. Nouailhat and A.G. Antolini, Journal of Applied Physics **59** (5), 1536 (1986)

R.F. Pierret, *Advanced Semiconductor Fundamentals*, Modular Series on Solid State Devices (Editors: R.F. Pierret and G.W. Neudeck), Vol. VI (Addison-Wesley, 1989)

H. Pinkney, P. Simpson, J.U. Kang, D.A. Thompson, B.J. Robinson and P. Mascher, Journal of Vacuum Science and Technology **A16** (2), 772 (1998)

L. Qian, S.D. Benjamin, P.W.E. Smith, B.J. Robinson and D.A. Thompson, Applied Physics Letters **71**, 1513 (1997)

L. Qian, S.D. Benjamin, P.W.E. Smith, B.J. Robinson and D.A. Thompson, Optics Letters **22**, 108 (1997)

L. Qian, presentation at OESC 97, Third Graduate Student Opto-electronic Semiconductor Conference on Materials, Devices and Applications, University of British Columbia, B.C., 4-6 June, 1997

L. Qian, S.D. Benjamin, P.W.E. Smith, H. Pinkney, D.A. Thompson and B.J. Robinson, presentation at CLEO 99, Baltimore, U.S.A., May 1999

E.V.K. Rao, F. Alaoui, Y. Gao, J.L. Benchimol and H. Thibierge, Semiconductor Science and Technology **6**, 125 (1991)

B.J. Robinson, D.A. Thompson, O.J. Lumley, S.A. McMaster, J. Zhao, H. Pinkney, L. Qian, S.D. Benjamin and P.W.E. Smith, Proceedings of the Ninth International Conference on Indium Phosphide and Related Materials, Cape Cod, MA (1997), p. 70.

K. Saarinen, P. Hautojarvi and C. Corbel, *Identification of Defects in Semiconductors*, Semiconductors and Semimetals (Treatise Editors: R.K. Willardson, A.C. Beer and E.R. Weber), Vol 51A (Volume editor: M. Stavola), (Academic Press, 1998)

B.E.A. Saleh and M.C. Teich, *Fundamentals of Photonics*, (John Wiley and Sons, 1991)

Y. Sasai, Y. Yamazoe, M. Okuyama, T. Nishino and Y. Hamakawa, Japanese Journal of Applied Physics **18** (7), 1415 (1979)

A.P. Seitsonen, R. Virkkunen, M.J. Puska and R.M. Nieminen, Physical Review **B49** (8), 5253 (1994)

B. Sermage, H.J. Eichler, J.P Heritage, R.J. Nelson and N.K. Dutta, Applied Physics Letters **42**, 259 (1983)

M. Sheik-Bahae, A.A. Said, T.H. Wei, D.J. Hagan and E.W. van Stryland, IEEE Journal of Quantum Electronics **QE-26**, 760 (1990)

S.M. Shibli and M.M. Garcia de Carvalho, Journal of Applied Physics **64** (1), 235 (1988)

F.W. Smith, H.Q. Le, V. Diadiuk, M.A. Hollis, A.R.Calawa, S. Gupta, M. Frankel, D.R. Dykaar,G.A. Mourou and T.Y. Hsiang, Applied Physics Letters **54** (10), 890 (1989)

P.W.E. Smith and S.D. Benjamin, Optical Engineering **34**, 189 (1995)

R.-S. Tang, L. Sargent and J.S. Blakemore, Journal of Applied Physics **66** (1), 256 (1989)

H. Temkin, V.G. Keramidas, M.A. Pollack and W.R. Wagner, Journal of Applied Physics **52** (3), 1574 (1981)

H. Temkin and B.V. Dutt, Materials Research Society Symposium Proceedings **14**, 253 (1983)

D.A. Thompson, D.B. Mitchell, B.J. Robinson, R.R. LaPierre and P. Mascher, Proceedings of the Ninth International Conference on Ion Beam Modification of Materials, Canberra, Australia, 5-10 February, 1995, p. 769

Y.P Varshni, Physica **34**, 149 (1967)

W. Walukiewicz, J. Lagowski, L. Jastrzebski, P. Rava, M. Lichtensteiger, C.H. Gatos and H.C. Gatos, Journal of Applied Physics **51** (5), 2659 (1980)

A.C. Warren, J.M. Woodall, J.H. Burroughs, P.D. Kirchner, H.K. Heinrich, G. Arjavalingam, N. Katzenellenbogen, D. Grischkowsky, M.R. Melloch, N. Otsuka, K. Mahalingam, F.H. Pollak and X. Yin, Materials Research Society Symposium Proceedings **241**, 15 (1992)

G.W. Wicks, Critical Reviews in Solid State and Materials Science **18** (3), 239 (1993)

D. Wood, *Optoelectronic Semiconductor Devices*, Prentice Hall International Series in Optoelectronics (Consultant editors: J. Midwinter and B. Weiss), page 435, Prentice Hall, 1994

N. Yamamoto, K. Uwai and K. Takahei, Journal of Applied Physics **65** (8), 3072 (1989)

P.W. Yu, B.W. Liang and C.W. Tu, Applied Physics Letters **61** (20), 2443 (1992)

Q.-S. Zhu, K. Hiramatsu, N. Sawaki and I. Akasaki, Japanese Journal of Applied Physics **28** (8), L1326 (1989)

B. Ziebro, J.W. Hemsky and D.C. Look, Journal of Applied Physics **72**, 78 (1992)